Advanced nanomaterials for solid state hydrogen energy storage

Prof. zw. dr. inż. Robert A. Varin, Department of Mechanical and Mechatronics Engineering, University of Waterloo, Waterloo, Canada (robert.varin@uwaterloo.ca)

Lectures prepared for the Military University of Technology, "Ad Hoc Professorship" (Katedra "Ad Hoc"), Warsaw, Poland, October 8-26, 2018

Motto:

"The seeker after truth does not put his faith in any consensus, however venerable or widespread. Instead, he questions what he has learned of it, applying to it his hard-won scientific knowledge, and he inspects and inquires and investigates and checks and checks and checks again. The road to the truth is long and hard, but that is the road we must follow."

Ibn Al-Haytham, mathematician and astronomer (born c. 965, Basra, Iraq—died c. 1040, Cairo, Egypt); from Gregory Wrightstone, "INCONVENIENT FACTS: The science that Al Gore doesn't want you to know" (Kindle Location 41). Mill City Press, 2017. Kindle Edition.

CONTENTS:

1. INTRODUCTION

1.1. Motivation: The Hydrogen Economy

The energy supply to the humankind in the last two centuries was solely based on fossil fuels such as coal in the 19th and crude oil and natural gas in the 20th century. Unfortunately, this fossil fuel-based economy has led to a number of new challenges facing all of us in the 21st century the **first one** of which is a reduction in the world crude oil supply which could reach so-called "Hubbert's Peak" in the not-so-distant future [**1**]. Dr. M. K. Hubbert was a notable American geologist and geophysicist [**2**]. In the 1950's he proposed a theory *that fossil fuel production (in particular crude oil) in a given world region over time would follow a roughly **bell-shaped** curve without giving a precise formula*; *he later used the Hubbert curve, the derivative of the logistic curve for estimating future production using past observed discoveries*. Fig. 1.1 shows his first estimate from 1956 for the U.S. crude oil production. In general, the upper bound predicted reasonably well an actual production peak in the 1970's from *conventional* sources although the actual peak was slightly higher. He made some corrections to his theory in the 1960's which did not change the original picture. The major discrepancy after the year 2000 arises from recent advances in oil extraction technology from *unconventional* sources such as, for instance, shale oil

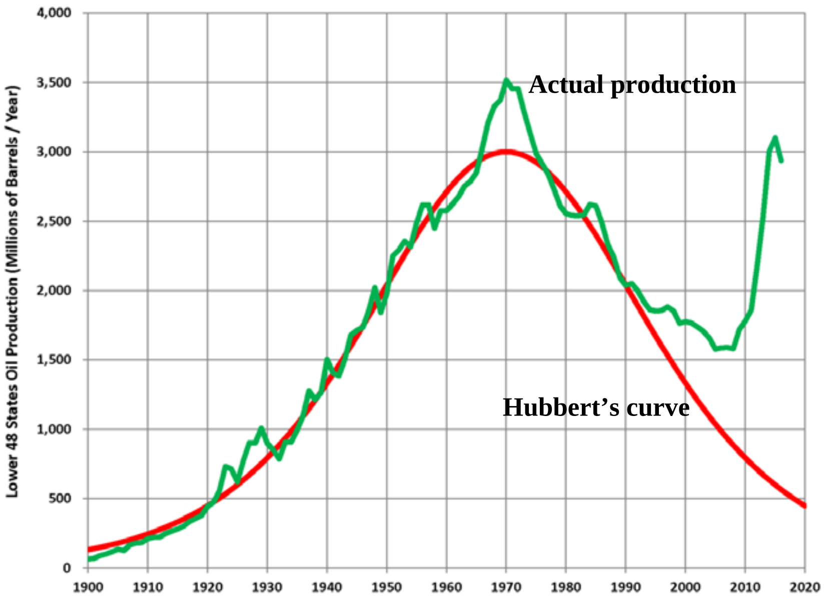

Fig. 1.1. Hubbert's upper-bound prediction for US crude oil production (1956), and actual lower-48 states production through 2014 [**1**].

(U.S.A.) or oil/tar sands (Canada). These presence of these sources was not taken into account by Hubbert neither he considered the dramatic improvements in the oil extraction techniques in the past 20 years. However, looking at the data on U.S. oil production and imports 1910-2012 in Fig. 2.1, it is seen that perhaps a general idea about a certain very diffuse peak for oil depletion seems to be still valid and may occur within the next 20-30 years.

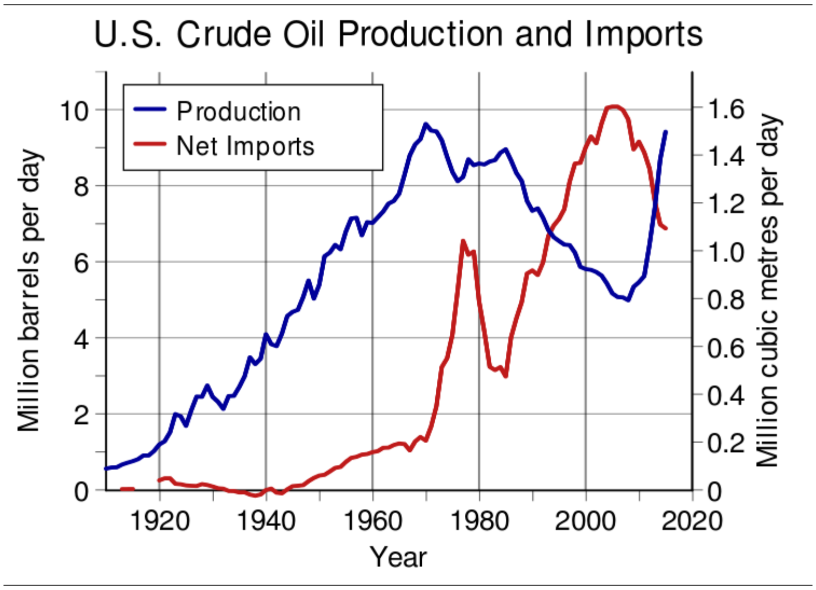

Fig. 1.2. U.S. Oil Production and Imports 1910 to 2012 [1].

It is also noted that no major conventional oil field has been discovered since 1970 [3].

The second challenge pushing towards getting rid of fossil fuels is poor urban air quality which leads to increased lung disease problems (e.g. asthma). Tens of millions of automobiles using gasoline/diesel combustion engines, running the urban streets, exhaust various obnoxious gases like nitrogen oxides (NO_x).

The third challenge is so-called “global warming” and following “climate change” due to the release of growing amounts of greenhouse gas CO_2. In theory, the “greenhouse effect” is a culprit for global warming/climate change. According to a theoretical mechanism [4] while about 30% of the Sun’s radiation is reflected by clouds, most of it passes through the Earth’s atmosphere and strikes the surface. There it is absorbed and its energy *emitted in the near-infrared spectrum*. Some of that re-emitted energy is absorbed by greenhouse-gas molecules. As they absorb the radiation, they *in turn emit energy in the form of heat creating the greenhouse effect*, as schematically shown in Fig. 1.3. As further discussed by Wrightstone [4], “greenhouse gases

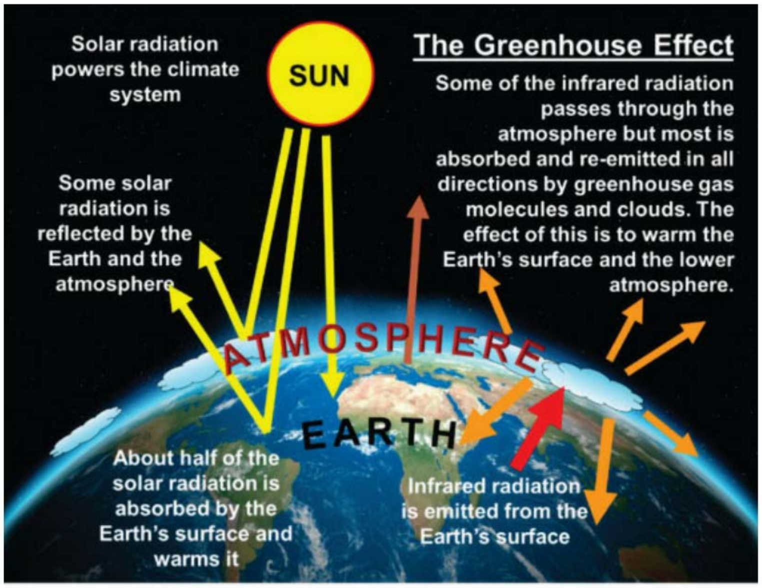

(Modified from IPCC 2007)

Fig.1.3. The greenhouse effect [4].

and the warming they cause keep the Earth at a comfortable average temperature of about 15° Celsius. Without them, the Earth would be an unlivable -18°C. Good examples of the extremes of greenhouse warming are two nearby planets, as they bookend the spectrum of greenhouse gas concentration. Venus has a pea-soup atmosphere, with CO_2 comprising 96% (compared with 0.04% for Earth), and an average temperature of almost 462°C. Meanwhile, Mars has virtually no atmosphere, and a temperature of -55°C (-67°F). This is the “Goldilocks effect”: Venus is too hot; Mars is too cold; Earth is just right”. Furthermore, as clearly pointed out by Wrightstone [4]: “*In the discussion about greenhouse gases, alarmist organizations and their allies in the media focus solely on man-made gases as the main agents of greenhouse warming. They do not mention the most significant greenhouse gas of all—water vapor. For example, the National Geographic climate-change website reports that greenhouse gases “include carbon dioxide (CO_2), methane, nitrous oxide (NO_x), fluorinated gases, and ozone. EPA’s greenhouse-gas pie chart is something like the lefthand chart in Fig. 1.4. It shows no contribution from water vapor. Based solely on* *charts like this and descriptions like that given by National Geographic, one might well conclude that CO_2 is the main driver of greenhouse warming. Before global warming*

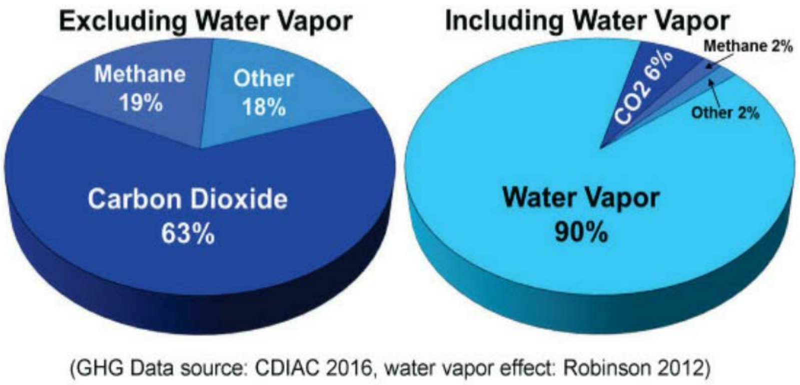

Fig. 1.4. The contribution of greenhouse gases to global warming [4].

became a political issue, it was generally accepted among physicists that water vapor contributes 60 to 95% of the greenhouse effect. It is no more sensible or workable for governments to attempt to regulate the weather by declaring CO_2 to be a pollutant than it would be for them to try to regulate water vapor or declare it to be a pollutant. The role of water vapor within climate models and predictions based on it is an inexact science, as the amount of water vapor in the air varies markedly from place to place and from day to day. Absolute humidity can range from near zero in deserts and Antarctica—the Earth's driest continent—to about 4% in the steamy tropics (Driessen 2014). Even a very small change in water vapor, however, can so affect the greenhouse effect as would a doubling of the present CO2 concentration in the atmosphere (Robinson 2012). Downplaying or disregarding water vapor, or assigning too large a magnitude to feedbacks such as the water-vapor feedback that is thought to amplify the direct warming from CO2, serves to overemphasize Man's contribution to greenhouse warming".

Inconvenient fact 1: ***Carbon dioxide (CO_2) is NOT the primary greenhouse gas.***

The second **Inconvenient fact** is that "***The warming effect of CO_2 declines as its concentration increases***" as shown in Fig. 1.5 [4].

Inconvenient fact 2: *The warming effect of CO_2 declines as its concentration increases*.

In the words of Wrightstone: "*Climate scientists have determined, and both sides agree, that the warming effect of each molecule of CO_2 decreases significantly (logarithmically) as its concentration increases. This is one reason why there was no runaway greenhouse warming* *when the concentration of CO_2 was approaching 20 times that of today. This inconvenient fact, important though it is, is kept very well hidden and is rarely mentioned, for it undermines the theory of future catastrophic climate change (Hoskins 2014)".*

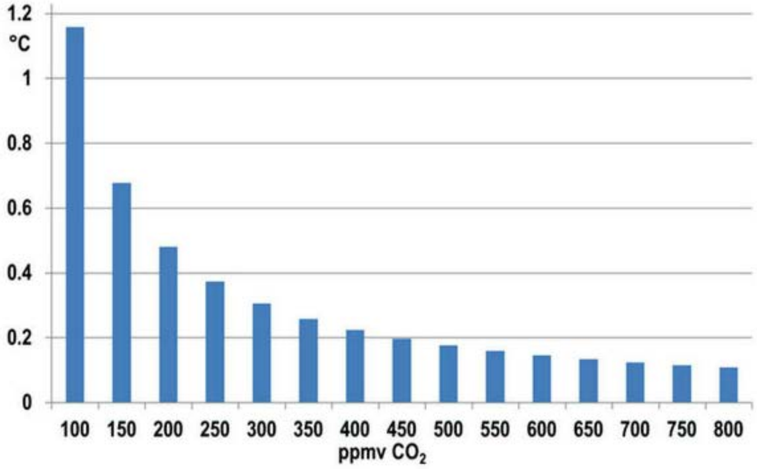

(Graph calculated using IPCC's formula $\Delta T_0 = \frac{5.35}{3.2} \ln \frac{C}{C_0}$;AR3, Ch. 6.1. Courtesy Monckton 2017)

Fig. 1.5. The warming effect of CO_2 declines as its concentration increases [4].

Summary — Greenhouse Gases

"***There is no dispute among scientists that CO_2 is a greenhouse gas, and that increasing CO_2 concentrations will increase global temperature to some degree. The $100 trillion question is: To what degree? The proponents of man-made warming will tell you emphatically that CO_2 is the prime cause of current temperature changes, while, as we shall see in subsequent chapters, true science demonstrates that the slight warming caused by CO_2 is likely largely overwhelmed by the same natural climate drivers that have been active for hundreds of millions of years***"[4]. There are number of other "inconvenient facts" about the effect of CO_2 can be found in ref. [4] which is highly recommended for reading.

Since the mid-1970's a concept of the ecologically clean Hydrogen Economy has been gaining a momentum as essentially the only viable remedy for the growing world energy consumption. The Hydrogen Economy offers a potential solution to satisfying the global energy requirements and improving energy security without involving more fossil fuels. Hydrogen is a very attractive alternative energy *vector*. It is ubiquitous, clean, efficient, and can be produced directly from sunlight and water by biological organisms and using semiconductor-based systems similar to photovoltaics. Hydrogen can also be produced indirectly via thermal processing of biomass or fossil fuels where the development of advanced technological processes combined with a CO_2 sequestration if required [5] have the potential to produce essentially unlimited quantities of hydrogen. For example, electricity produced by wind turbines or nuclear power plants during off-peak periods [6] can be used for the electrolysis of water into hydrogen [7] and the latter stored for future distribution to places of use.

1.2. Principal obstacles for implementing the Hydrogen Economy

The realization of the enormous benefits of the Hydrogen Economy has triggered over the last 15 years, intense activities into the development of hydrogen related technologies. There are **three major technological obstacles** to the full implementation of the Hydrogen Economy in the next few decades.

The first is the cost of safe and efficient production of hydrogen gas. As shown in Fig. 1.6 at present, 48% of hydrogen is produced from methane steam reforming, 30% from oil/naphtha reforming, 18% from coal gasification and only 3.9% from the electrolysis of water [8]. Apparently, the bulk of hydrogen production still relies upon fossil fuels a by-product of which is CO_2. However, the fossil fuel-based processes are much cheaper than the electrolysis of water which does not produce any by-products. Since, as argued earlier CO_2 is only minor greenhouse gas its presence as a by-product of methane steam reforming should not be of a great concern.

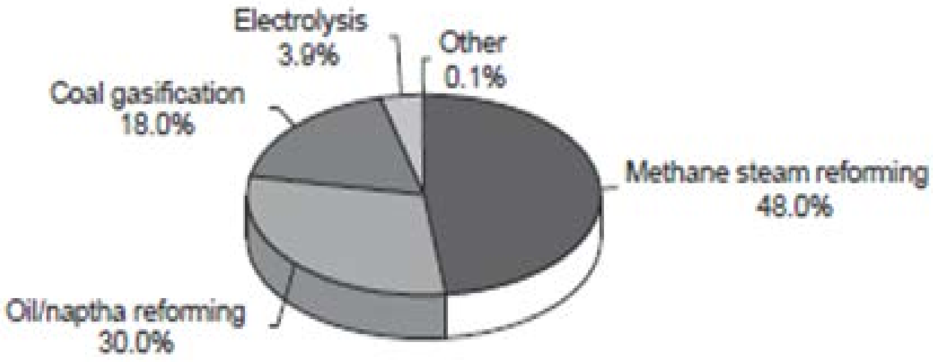

Fig.1.6. Present distribution of primary energy sources for hydrogen production [8].

However, if someone wants to avoid any CO_2 by-product there is always another alternative: water electrolysis. It is much more expensive than methane steam reforming although the efforts are underway to reduce the price of electrolysis-derived hydrogen to $2-3/kg.

The second obstacle is the further **development of PEM fuel cell (PEMFC)** which is the primary cell most suitable for transportation. Most importantly, the research is focused on the extension of the usable service life, water flooding, dynamics and reliability. The present cost of energy derived from a PEMFC for an 80 kW automotive fuel cell system is around $46/kW assuming a mass production of 500,000 FCVs per year [9]. The Department of Energy (U.S.A.) Ultimate target requires the cost of $30/kW. It is quite clear that the fuel cell stack obstacle has been substantially relaxed nowadays from the projected cost of $200/kW some 10 years ago [10].

How does a fuel cell work? When hydrogen burns, it releases energy as heat and produces water:

$$2H_2 + O_2 \rightarrow 2H_2O + \textbf{HEAT} \qquad (1.1)$$

However, if **air** is used for flame combustion of hydrogen, small amounts of NO_x may be produced.

A schematic of a Proton Exchange Membrane (PEM) Fuel Cell is shown in Fig. 1.6.

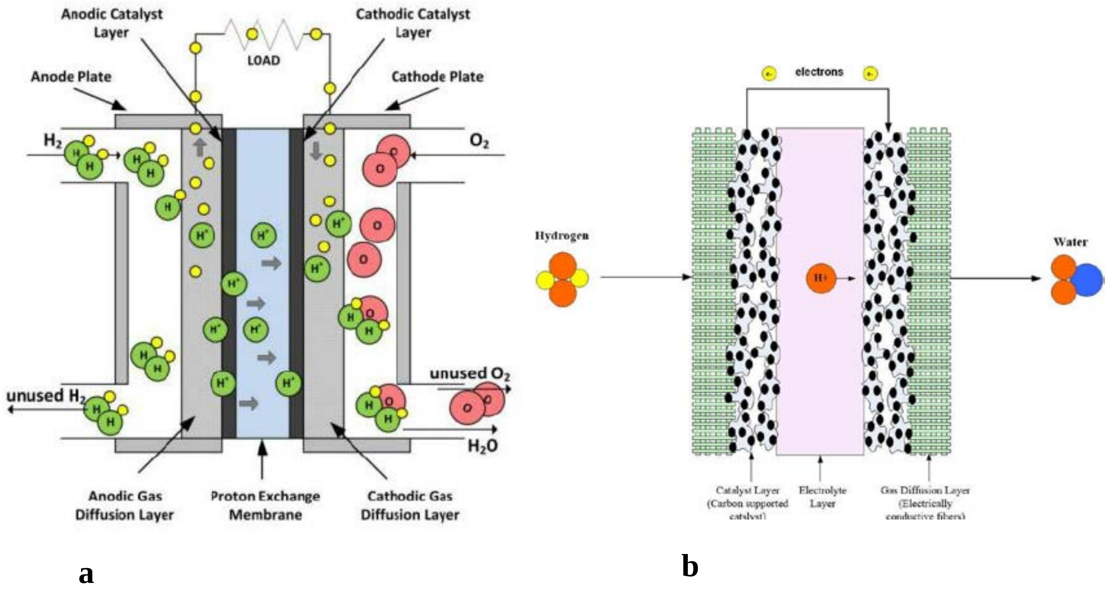

Fig. 1.7. (a) Proton Exchange Membrane (PEM) Fuel Cell schematic representation [11]. (b) A configuration of the layers of a single PEM FC [12].

Reactions:

Anode: $2H_2 \Leftrightarrow 4H^+ + 4\bar{e}$ (1.2a)

Cathode: $O_2 + 4H^+ + 4\bar{e} \Leftrightarrow 2H_2O$ (1.2b)

Overall: $2H_2 + O_2 + \Leftrightarrow 2H_2O$ + *electricity* + ***heat*** (1.2c)

A proton-exchange membrane, or polymer-electrolyte membrane (PEM), is a semipermeable membrane generally made from ionomers and designed to conduct protons while acting as an electronic insulator and reactant barrier, e.g. to oxygen and hydrogen gas (Fig. 1.6b). This is their essential function when incorporated into a membrane electrode assembly (MEA) of a proton-exchange membrane fuel cell or of a proton-exchange membrane electrolyser: separation of reactants and transport of protons while blocking a direct electronic pathway through the membrane [**13**]. PEMs can be made from either pure polymer membranes or from composite membranes, where other materials are embedded in a polymer matrix. One of the most common and commercially available PEM materials is the fluoropolymer (PFSA) Nafion, a DuPont product. While Nafion is an ionomer with a perfluorinated backbone like Teflon, there are many other structural motifs used to make ionomers for proton-exchange membranes. Many use polyaromatic polymers, while others use partially fluorinated polymers [**13**].

Pure hydrogen enters the anode channel in a fuel cell, diffuses through a porous anode towards the catalyst (usually nanometric Pt, Fig. 1.6b) where the hydrogen molecules H_2 are *stripped of their electrons* and become positively charged ions (protons) (reaction 1.2a). Protons then migrate through the proton-permeable polymeric (Nafion) membrane and the electrons generated during oxidation pass through the external circuit to the cathode, thereby creating electric current (Fig. 1.6a). On the cathode side, a humidified air enters the cathode channel and diffuses towards the cathode-side catalyst layer (Fig. 1.6a). At the catalyst Pt surface (Fig. 1.6a and b), hydrogen protons recombine with electrons and oxygen molecules in air to produce water and heat according to the overall reaction 1.2c. And the last but not least is the fact that a hydrogen fuel-cell car can convert hydrogen energy into motion **about 2–3 times as efficiently** as a normal car converts gasoline energy into motion: depending on how it’s designed and run, a good fuel-cell system is about 50–70% efficient, hydrogen-to-electricity, while a typical car engine’s efficiency from gasoline to output shaft averages only about 15–17% efficient [**14**]. **It must be pointed out that hydrogen gas supplied to a fuel cell is required to have slight overpressure, usually within the range 1.1-1.8 bar (even more for a large fuel cell stack).**

A single cell produces voltage between 0 and 1V [11], so to produce a higher voltage, multiple cells have to be connected in series to form a **FUEL CELL STACK.** Fig. 1.7 shows a cutaway of a production fuel cell stack for the Toyota Mirai Fuel Cell Vehicle (FVC)[15]. According to the specifications [16] this particular stack is composed of **370** individual fuel cells which are connected in a single-line stacking (series) resulting in the nominal voltage of 244 V and the capacity of 6.5 Ah [17]. As shown in reactions (1.1) and (1.2c) each individual fuel cell generates some quantity of waste heat. **Its quantity is very small for an individual cell. However, the waste heat quantity dramatically increases when the number of cells increases in a fuel cell stack.** For large stacks like the one used for the Toyota Mirai in Fig. 1.7, this **waste heat can rise a PEM fuel cell operating temperature to 60-80°C** [14](for practical experimental measurements a sort of unwritten consensus is **100°C** considering this as an upper temperature limit for a very large fuel cell stack). Normally, the waste heat of a stack running on hydrogen supplied from a gas cylinder is **extracted** by the cooling system and gradually dispersed. However, it may play an important role when a source of hydrogen are solid state hydrides as will be discussed later.

Fig. 1.8. Toyota Mirai Fuel Cell cutaway exhibited at the Salão Internacional do Automóvel 2016, São Paulo, Brazil showing a fuel cell stack [15]. This particular stack is composed of 370 individual fuel cells [16].

The third obstacle is **hydrogen storage** for supplying PEMFC. Hydrogen storage is a key enabling technology for the advancement of hydrogen vehicles in the automotive industry. In order to standardize the technical approaches for research on hydrogen automotive storage systems the U.S. Department of Energy (D.O.E.) introduced a number of targets for **on board** hydrogen storage systems within the frame work of its FreedomCAR program (2003) for the years 2007, 2010 and 2015 which, for a historical perspective, are listed in Table 1.1 [**17**]. The original targets where set in 2003 based on attempting to be competitive with conventional gasoline fuel systems. They were revised in 2009 to enable greater than **300-mile range** within the allocated package space and weight for hydrogen storage systems in representative fuel cell vehicles.

Table 1.1. U.S. D.O.E. FreedomCAR program (2003) hydrogen storage system historical targets [**10**]

Targeted factor	**2007**	**2010**	**2015**
System gravimetric capacity (kgH_2/kg system)	0.045	0.060	0.090
System volumetric capacity (kgH_2/m^3)	36	45	81
Energy density (MJ/L)	-	5.4	9.72
Storage system cost ($/$kgH_2$)	200	133	67
Operating temperature (°C)	-20/50	-30/50	-40/60
Min/max delivery temperature (°C)	-30/85	-40/85	-40/85
Cycle life-time (absorption/desorption cycles)	500	1000	1500
Flow rate (full throttle) (g/s)	3	4	5
Delivery pressure from storage system (bar)	2.5	2.5	2.5
Transient response (s) (10-90% and 90-0%)	30	15	15
Refueling rate (kgH_2/min)	0.5	1.5	2.0

Since the last major target revision in 2009, significant progress has been made on the development and implementation of FCEVs thus necessitating the need to add and revise several targets. Tables 1.2 below provides a summary of the principal targets that have been revised and added since the last major target update in 2009. The other targets can be found in the original document [**18**]. Note that in 2009, the targets were developed for 2015 and “Ultimate Full Fleet” targets were added to capture virtually all light-duty vehicle platforms (“significant market penetration”). The original 2015 targets were developed based on an assumption that the DOE funding for hydrogen storage research and development would remain fairly constant. Since 2009, funding for the DOE Hydrogen Storage Program has been at reduced levels thus impacting the ability to meet the 2015 targets and shifting these targets to 2025. Still, the targets in Table 1.2 enable **greater than 300-mile range** within the allocated package space and weight for hydrogen storage systems.

Table 1.2. Revised Technical System Targets: Onboard Hydrogen Storage for Light-Duty Fuel Cell Vehicles [a, i] [18]

Targeted factor	2020	2025	Ultimate
System gravimetric capacity (kgH_2/kg system)[b)]	0.045	0.055	0.065
System volumetric capacity (kgH_2/m^3)[b)]	30	40	50
Storage system cost (\$/kgH_2 stored)	333	300	266
Operating temperature (°C)	-40/60	-40/60	-40/60
Min/max delivery temperature (°C)	-40/85	-40/85	-40/85
Cycle life-time (absorption/desorption cycles)	1500	1500	1500
System fill time (min)	3-5	3-5	3-5
Min. delivery pressure from storage system (bar) Max. delivery pressure from storage system (bar)	5 12	5 12	5 12
Transient response (s) (10-90% and 90-0%)	0.75	0.75	0.75
Average flow rate (g/s)/kW	0.004	0.004	0.004

[a)] For a normalized comparison of system performance to the targets, a usable H_2 storage capacity of 5.6 kg H_2 should be used at the lower heating value of hydrogen (33.3 kWh/kg H_2). Targets are for a complete system, including tank, material, valves, regulators, piping, mounting brackets, insulation, added cooling capacity, and all other balance-of-plant components. All capacities are defined as usable capacities that could be delivered to the fuel cell system. All targets must be met at the end of service life.

[b)] Capacities are defined as the usable quantity of hydrogen deliverable to the fuel cell system divided by the total mass/volume of the complete storage system, including all stored hydrogen, media, reactants (e.g., water for hydrolysis-based systems), and system components. Capacities must be met at end of service life. Tank designs that are conformable and have the ability to be efficiently package onboard vehicles may be beneficial even if they do not meet the full volumetric capacity targets.

Finally, it is interesting to compare electric vehicle (EV) vs. fuel cell vehicle (FVC) on a general factors of cruising range and system cost schematically shown in Fig. 1.9. It appears that EV’s are more suitable on the cost basis than FCV’s at short cruising ranges. In contrast, FCV’s are more cost competitive at long cruising ranges. This important consideration was a driving force for implementation the automotive program for an advanced FCV such as Toyota Mirai which is introduced below in this chapter.

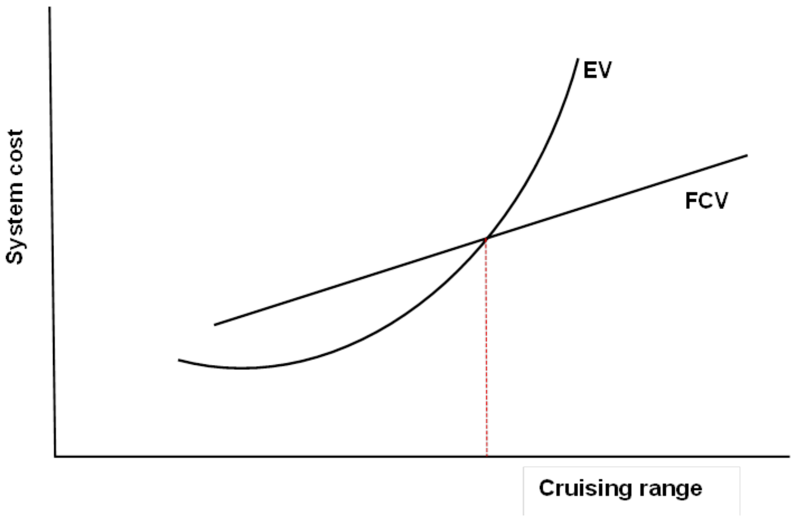

Fig. 1.9. A cruising range/system cost comparison of EV vs. FCV [Private communication by Dr. Katsuhiko Hirose; NSERC Hydrogen Canada (H2CAN) Strategic Research Network; 4th AGM& Conference, June 2---6, 2013; HYDROGEN MARKETS: TODAY AND NEAR FUTURE–INDUSTRY PERSPECTIVE-Keynote Presentation–Automotive Perspective (Toyota)].

1.3. Competing technologies for hydrogen storage for automotive applications

There are three major competing technologies for automotive hydrogen storage which will be briefly characterized. They are as follows: **compressed gas cylinders**, **liquid hydrogen tanks** and **solid metal/complex hydrides** [**10**].

A major drawback of compressed hydrogen storage for automotive is the small amount of hydrogen that may be stored in a reasonable volume (volumetric capacity/density). Compressed hydrogen gas technologies, even at such enormous pressures as 70 MPa, also suffer from low volumetric densities not exceeding 40 kgH_2m^{-3}. As pointed out by Sandi [**19**] even at such a high pressure as 70 MPa the energy content of compressed hydrogen is significantly less than that for the same volume of gasoline, 4.4 MJ/L (at 70 MPa) for hydrogen compared with 31.6 MJ/L for gasoline. Even though considered to be quite simple and inexpensive, the high pressure of 70MPa involved in hydrogen gas cylinders raises safety concern. There is also an additional cost involved with compression to such high pressures. Another consideration is the large pressure drop during use. Furthermore, martensitic steel is eliminated from any considerations for hydrogen reservoirs because there is a concern of well-known hydrogen embrittlement [**19**].

Nevertheless, a gaseous hydrogen storage is the first storage technology used nowadays commercially in the production of the FCV Toyota Mirai (Fig. 1.10) [**15, 16**].

Fig. 1.10. The Toyota Mirai 2016 [**15, 16**].

In the Mirai, hydrogen gas is stored under 70 MPa pressure in two reservoirs of cylindrical shape (Fig. 1.11) [**20**]. Cylinders of this kind are based on carbon fiber reinforced polymeric matrices and are manufactured by a well-known filament winding processes (Fig. 1.12) [**21**]. Filament winding is a process by which continuous high strength/modulus reinforcing fibers like, for example, glass or carbon fibers are accurately positioned in a predetermined pattern on a hollow, generally cylindrical shape. The continuous fiber rovings/tows are first fed through the resin bath and then are wound on a cylindrical mandrel, using an automated winding machine. The required directionality of the fibers is provided by the carriage (Fig. 1.12). After the appropriate number of layers have been applied, curing is carried out either in an oven or at room temperature after which the mandrel is removed. The process affords the high strength to weight ratio laminates

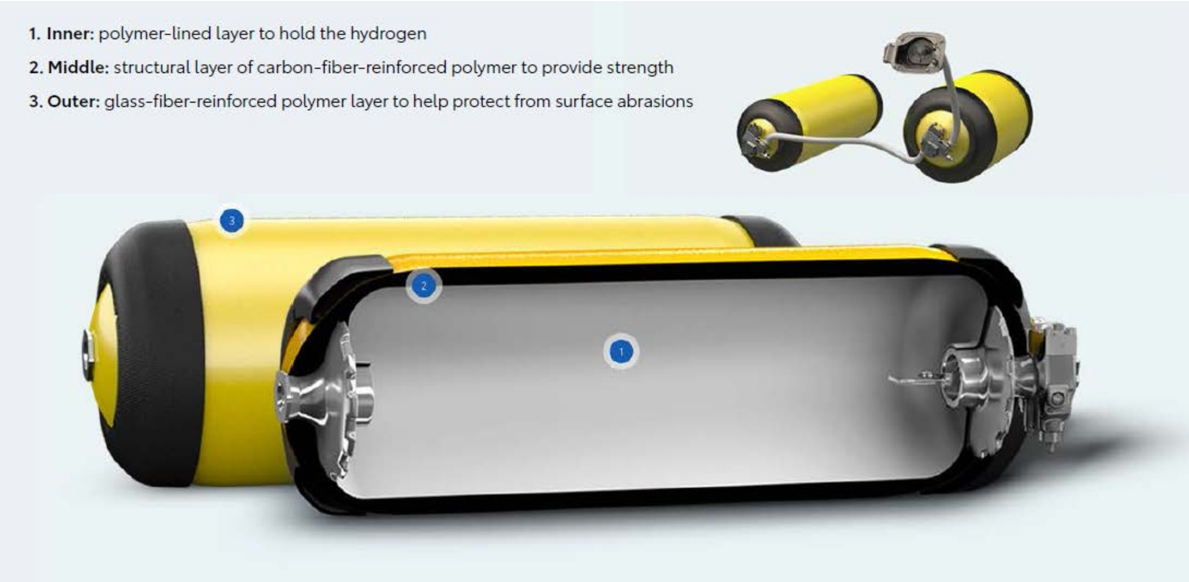

Fig. 1.11. Two cylindrical hydrogen tanks for the Toyota Mirai [20].

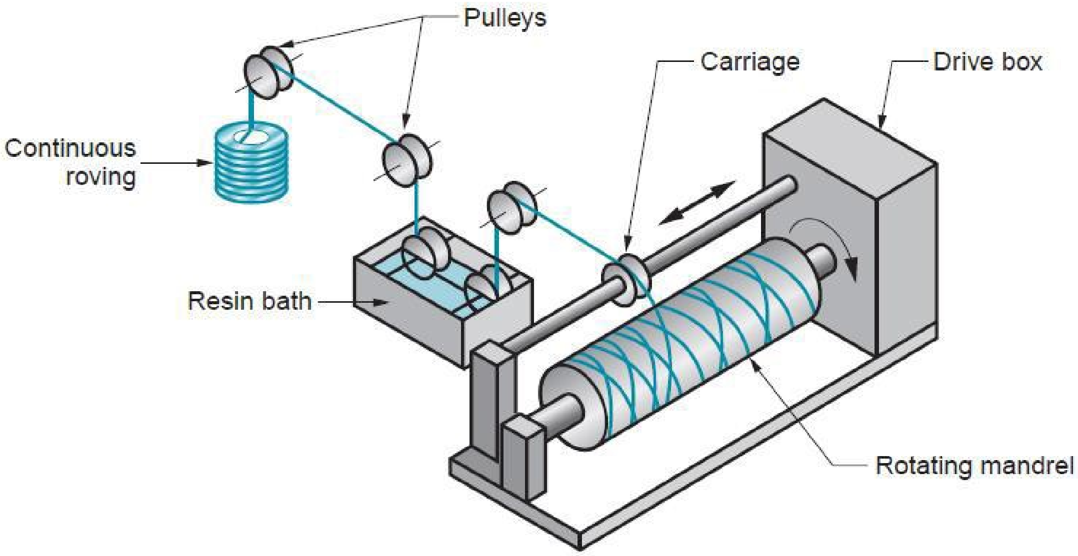

Fig. 1.12. Common form of filament winding process [21].

and provides a high degree of control over uniformity and fiber orientation. Three patterns of filament winding exist that are shown in Fig. 1.13. The polar winding pattern allows formation of reinforced end caps on the cylindrical mandrel but in this case the mandrel cannot be removed after curing. Fig. 1.14 shows the commercial multi-axis filament winding machine making a polar winding product with reinforced end caps [23].

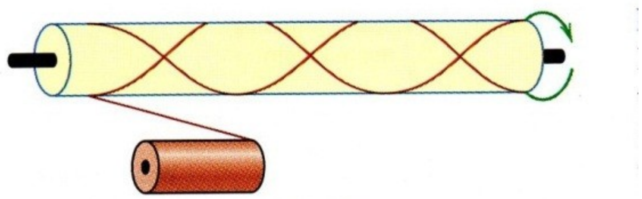

Helical winding

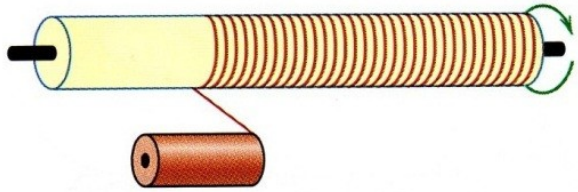

Circumferential winding

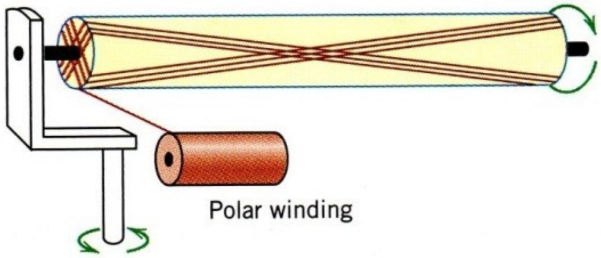

Polar winding

Fig. 1.13. Schematic representations of helical, circumferential and polar filament winding techniques [22].

Fig. 1.14. Multi-axis filament winding machine by VEM, S.p.A. [23].

The **liquid hydrogen tank** for its part offers a high H_2 storage capacity by volume as pressurized hydrogen. However, a major drawback of liquid storage is a big cost of liquefaction which today can add as much as 50% to the cost of H_2 [10]. There are also safety issues associated with the handling of cryogenic liquids and the problem of evaporative loss

Solid state hydrides which include metal/intermetallic and complex (chemical) hydrides are characterized by the highest volumetric capacities and they do not suffer drawbacks as those experienced by compressed and liquid hydrogen. Because of the low pressures involved in metal hydride technologies the safety is better than that for the 70 MPa/liquid H_2 storage. Moreover, the hydrogen released from a metal hydride is of a **very high purity** and therefore, can be used directly to feed a PEM fuel cell (D.O.E targets quote **99.97% H_2** dry basis as per SJ2579 [18, 24]. However, solid state H_2 storage in hydrides has its own serious constraints. A brief comparison of all three H_2 storage technologies is shown in Table 1.3.

Table 1.3. Comparison of three major competing technologies for hydrogen storage (based on [10]).

Storage system	**Volumetric hydrogen capacity (kgH_2m^{-3})**	**Drawbacks**
Compressed hydrogen gas under 70 MPa pressure	~40	Safety problem since enormous pressures are required; cost of pressurization; large pressure drop during use
Liquid hydrogen at cryogenic tank at -252°C (21K)	~71	Large thermal losses (open system); safety; cost of liquefaction
Solid state hydrides	80-160	None of the above

1.4. Brief characterization of solid hydrides as H_2 storage media

It is now appropriate to discuss solid state hydrogen storage in hydrides in the context of the targets shown in Table 1.2 and requirements of a fuel cell stack. We can consider them as "*D.O.E. constraints*" and "*PEM fuel stack constraints*".

D.O.E. constraints (man-made)

First and foremost, the D.O.E. automotive targets/constraints in Table 1.2 require at least a minimum of 4.5 wt.% H_2 (2020) or 6.5 wt.% H_2 Ultimate storage capacities for the entire **storage SYSTEM**. These are **NOT the storage capacities of an H_2 storage medium**. **A general approximate consensus is that the storage medium H_2 capacity should be at least twice as large as a system storage [25] which translates to roughly 9 wt.% H_2 for 2020 and 13 wt.% H_2 Ultimate for automotive applications**.

Another constraint made obligatory by D.O.E. which is not explicitly spelled out but can be invoked from Table 1.2 is that the hydrogen medium in the reservoir must be able to be **REHYDROGENATED ON-BOARD** (cycle life-time system fill time, transient response, etc.). This target of on-board hydrogen storage requires the *reversibility* of solid state hydrides (e.g. onboard hydrogen refueling as shown in Table 1.2). However the problem arises when the **rehydrogenation** process of a solid hydride would be ***exothermic*** in nature (releases heat during rehydrogenation and consumption of heat upon dehydrogenation; the thermodynamics of hydrides will be discussed later). In this case, as pointed out by Sandrock et al. [**26**], there is an immense problem to remove the exothermic heat at the prescribed charging rate. For example, if we charged H_2 at 1.5 kg/min into a vehicular storage tank based on $NaAlH_4$ (ΔH =37 kJ/mol H_2), we would have to remove heat at the rate of 450 kW! This would require very substantial and costly heat-exchangers and in practice would completely eliminate the possibility of quick onboard recharging. Obviously, this problem does not exist for a pressurized gaseous storage reservoir.

PEM fuel stack constraints

The first is that the storage media must desorb hydrogen **at the temperature range not exceeding the waste heat temperature of a fuel cell stack which at maximum is about 100°C**. This is **an upper bound for desorption temperature** and it will be **much lower for small fuel cell stacks, perhaps, closer to room temperature**.

The second is that desorption must occur at **an H_2 overpressure of at least 1.1-1.8 bar** (Table 1.2 even calls for 5 bar although that might be a bit overestimated).

Conventional **metal hydrides** based on metals such as V, La, Nb, Pd and Na have H_2 gravimetric capacities too low for any commercial consideration not only for automotive hydrogen storage but for any other **gaseous** H_2 non-automotive storage for that matter.

One outstanding simple metal hydride is the LiH hydride based on Li which has a high capacity (~13 wt.% H_2) while, simultaneously, it has extremely high desorption temperature [**27**]. A notable exception of a metal hydride is MgH_2 which has a relatively high gravimetric capacity and can desorb at about 300°C after nanostructuring treatment [**10**]. **In essence, none of simple metal hydrides can meet the D.O.E. automotive targets for gravimetric capacity.**

Similarly, hydrides based on intermetallic compounds AB (FeTi, ZrNi), AB_2 ($ZrMn_2$/$TiMn_2$/$TiCr_2$), AB_5 ($LaNi_5$ or $MmNi_5$ where Mm-mischmetal) and A_2B (Mg_2Ni) have relatively low gravimetric storage capacities as shown in Table 1.4 which are unsuitable for automotive storage although a number of them desorbs hydrogen within the range of waste heat generated temperature of a large fuel cell stack at the desorption pressure ($P_{desorption}$) of 1 bar (or 1 atm). Interestingly, the La(Mm)Ni_5H_6-type hydrides are commercially used for a number of years for electrochemical H_2 storage in the Ni-metal hydride (Ni-MH) batteries.

Table 1.4. Hydrogen storage properties of selected intermetallic compounds [10]

Maximum hydrogen capacity				
Type	**Intermetallic**	**Hydride**	**wt.%**	**Temperature for 1 atm $P_{desorption}$ (°C)**
A_2B	Mg_2Ni	Mg_2NiH_4	3.6	255
AB	FeTi	$FeTiH_2$	1.86	-8
AB	ZrNi	$ZrNiH_3$	1.85	292
AB_2	$ZrMn_2$	$ZrMn_2H_{3.6}$	1.77	167
AB_5/MmB_5	$LaNi_5$	$LaNi_5H_6$	1.49	12
AB_2	TiV_2 ($TiV_{0.62}Mn_{1.5}$)	$TiV_{0.62}Mn_{1.5}H_{2.5}$	2.15	-6

However, there exist many complex hydrides that have high and very high gravimetric storage capacities some of which are shown in Table 1.5 [10]. **Their theoretical capacity is simply calculated as the ratio of the atomic mass of hydrogen in the hydride formula to the molecular mass of hydride. (***For example, MgH_2 has one Mg atom having an atomic mass of 24.305 g/mol and* ***two atoms*** *of hydrogen having an atomic mass of 1.008 g/mol each (from The Periodic Table of The Elements) so the molecular mass of H_2=2x1.008 g/mol=**2.016** g/mol. Therefore, the molecular mass of MgH_2=24.305 g/mol+2.016 g/mol=26.321 g/mol. Therefore, the theoretical hydrogen capacity of MgH_2=2.016 g/mol/26.321 g/mol=0.0766 or by multiplying by 100% one obtains 7.66 wt.% H_2 as percentage of hydrogen by weight in a molecule of MgH_2.).*

Some of these hydrides called “complex” hydrides (like borohydrides) decompose in **a multi-stage sequence** such as, for example, **$LiBH_4$ which decomposes in the first stage into LiH+B+(3/2)H_2 and in the second stage LiH decomposes into Li and H.** The first stage reaction releases about 13.8 wt.% H_2 (3/2) mol of H_2 per 1 mol of $LiBH_4$ (*some authors claim that $LiBH_4$ decomposes in a slightly different sequence where the first stage is: $12LiBH_4 \rightarrow Li_2B_{12}H_{12}+10LiH+13H_2$ releasing 10 wt. % H_2 and in the second stage is: $Li_2B_{12}H_{12} \rightarrow 2LiH+12B+5H_2$ releasing 6.5 wt.% H_2* [28-30]).

Therefore, the fourth column in Table 1.4 includes “*theoretical gravimetric capacity of first stage*” for those complex hydrides which desorb through a multi-stage sequence (which is equal to the theoretical maximum for a single-stage hydrides). Unfortunately, as shown in the last column in Table 1.4 **the major problem of high H_2 capacity complex hydrides is that their**

desorption temperatures are not even close to the operating temperature range of a large fuel cell stack (max. 100°C) let alone smaller fuel cell stacks. Furthermore, some of the borohydrides such as $Zn(BH_4)_2$ which start desorbing around 80°C, close to the operating temperature of PEM FC, release a toxic borane gas, B_2H_6, together with hydrogen [**31, 32**] which can quickly destroy a PEM FC membrane and as such are useless as a storage medium. As discovered more recently, some borohydride systems with a relatively high H_2 capacity also desorb varying quantities (rather small) of B_2H_6 together with H_2 [**33-36**]. This will be discussed later in more detail.

In conclusion, one can say that vis-à-vis D.O.E. target constraints in Table 1.2 and constraints provided by a fuel cell stack, most of the high capacity hydrides in Table 1.5 cannot be seriously considered as on board storage materials for PEMFC vehicles. One of them is the inability to meet the need for "on-board" rehydrogenation as targeted by D.O.E. **So far, those serious constraints preclude a full implementation of solid state H_2 storage in the automotive sector.**

Table 1.5. Hydrogen storage properties of selected high-capacity hydrides [**10**]

Metal-hydrogen system	**Hydride**	**Theoretical maximum gravimetric H_2 capacity) (wt.%)**	**Theoretical gravimetric capacity of first stage (wt.%)**	**Approx. desorption temperature range (^{0}C)**
Li-B-H	$LiBH_4$	18.4	~13.8	~ 470
Mg-B-H	$Mg(BH_4)_2$	14.9	~11.2	~ 300
Fe-B-H	$Fe(BH_4)_3$	12.1	Unknown	<0 [Varin et al.]
Ca-B-H	$Ca(BH_4)_2$	11.6	Unknown	~320(?)
Na-B-H	$NaBH_4$	10.6	10.6	400-600
Li-Al-H	$LiAlH_4$	10.6	~7.9	110-260
Al-H	AlH_3	10.0	10.0	~150
Mg-Al-H	$Mg(AlH_4)_2$	9.3	~7.0	110-160
Li-N-H	$LiNH_2(+LiH+TiCl_3)$	8.8	~6.0	150-280
Zn-B-H	$Zn(BH_4)_2$	8.5	8.5(?)	85-140
Ca-Al-H	$Ca(AlH_4)_2$	7.9	~5.9	80-180
Mg-H	MgH_2	7.6	7.6	300-400
Na-Al-H	$NaAlH_4$	7.5	5.6	229-247
Mg-N-H	$Mg(NH_2)_2(+LiH)$	7.2	~7.0	140-250
Mg-Fe-H	Mg_2FeH_6	5.5	5.5	300-400

Na-N-H	$NaNH_2$	5.3	Unknown	<200 (?)

In 2009 we put forward an opinion [10] that a certain solution for automotive solid state storage was **off-board recharging** in which the depleted solid state hydride container was replete with nanostructured solid state storage materials manufactured in a dedicated plant as schematically shown in Fig. 1.15. Accordingly, the refueling station is just a retail station for hydrogen storage containers where "refueling" could become eventually a fully automated process reduced to a quick replacement of containers without any complicated infrastructure. This could also lead to the growth of new businesses for the Hydrogen Economy. Also, an off board re-charging solves the problem of chemical reversibility which creates a difficulty for a number of hydrides otherwise quite attractive as storage materials. Ball milling can be used to induce a "mechanical reversibility" carried out in a ball milling device instead of applying high pressure and temperature for the chemical synthesis. Such hydride storage technology based on mechano-chemical reactions and nanostructuring processes conducted in high-energy ball mills constitute the core of this book.

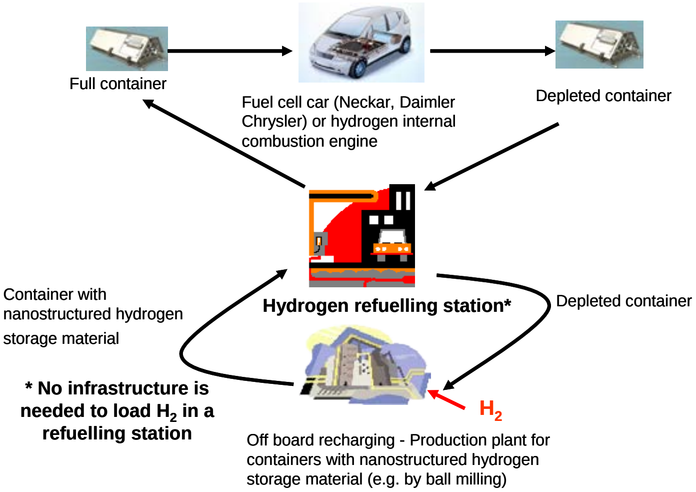

Fig.1.15. A novel vision of refueling/retail station for fuel cell powered vehicles based on the concept of the off-board recharging of spent hydride fuel and the mechano-chemical synthesis of nanostructured hydrogen storage materials in ball–mill plants. Such is not the currently accepted vision of hydrogen economy but one which may turn out to be viable alternative to onboard recharging [10].

However, beside automotive, some other commercial market applications for solid-state hydrogen storage systems may not critically require "on-board" rehydrogenation. Such H_2

storage/generation systems can utilize disposable H_2 cartridges of various sizes whose thermal decomposition products could be either regenerated **“off-board”**, after dehydrogenation, or converted into other useful chemicals. A number of potential, non-automotive applications exist, such as portable electronic devices, stationary auxiliary power systems, off road vehicles (e.g. fork lifts), drones, bulk hydrogen storage, air transportation and many others. Some of solid state hydrides suitable for these non-automotive applications will be discussed later on.

2. BRIEF HISTORY OF DEVELOPMENT OF HYDRIDES (based on [10])

2.1. Early investigations of metal-hydrogen systems and hydrides

In 1671, Robert Boyle discovered and described the reaction between iron filings and dilute acids, which results in the production of hydrogen gas. In 1766, Henry Cavendish was the first to recognize hydrogen gas as a discrete substance, by naming the gas from a metal-acid reaction "inflammable air". He speculated that "inflammable air" was in fact identical to the hypothetical substance called "phlogiston" and further finding in 1781 that the gas produces water when burned. He is usually given credit for the discovery of hydrogen as an element. In 1783, Antoine Lavoisier gave the element the name hydrogen (from the Greek ὑδρο- hydro meaning "water" and -γενής genes meaning "creator") when he and Laplace reproduced Cavendish's finding that water is produced when hydrogen is burned [37]. In the 18th century hydrogen gas was not used commercially expect perhaps for filling early air-travel balloons [37].

Although not considered to be stored and delivered from metal-hydrogen systems, hydrogen has been used for energy generation since the 1800s. Being a major constituent, up to 50 vol.%, of so-called *syngas*, synthetic gas manufactured by gasification of coal, wood or waste, it was widely used in homes in Eastern USA and Europe from circa 1850 until the Second World War. The *water gas reaction* utilized in production of *syngas* was the first in the man’s endeavor to generate energy from *hydrogen*, the most energetic and the most abundant ingredient of our geosphere and biosphere.

$$C + H_2O\ (\text{steam}) \rightarrow CO + H_2 \qquad (2.1)$$

At about same time when the hydrogen-rich *syngas* had been combusted for electricity generation in gas-fueled electric plants, some studies driven by pure scientific curiosity were conducted which led to observation of a direct conversion of hydrogen chemical energy into electrical energy. Sir Humphrey Davy (1802) experimented on a cell that utilized a carbon anode in aqueous nitric acid and Sir William Grove built a gaseous voltaic battery, what is considered the first *hydrogen fuel cell* (Fig. 2.1).

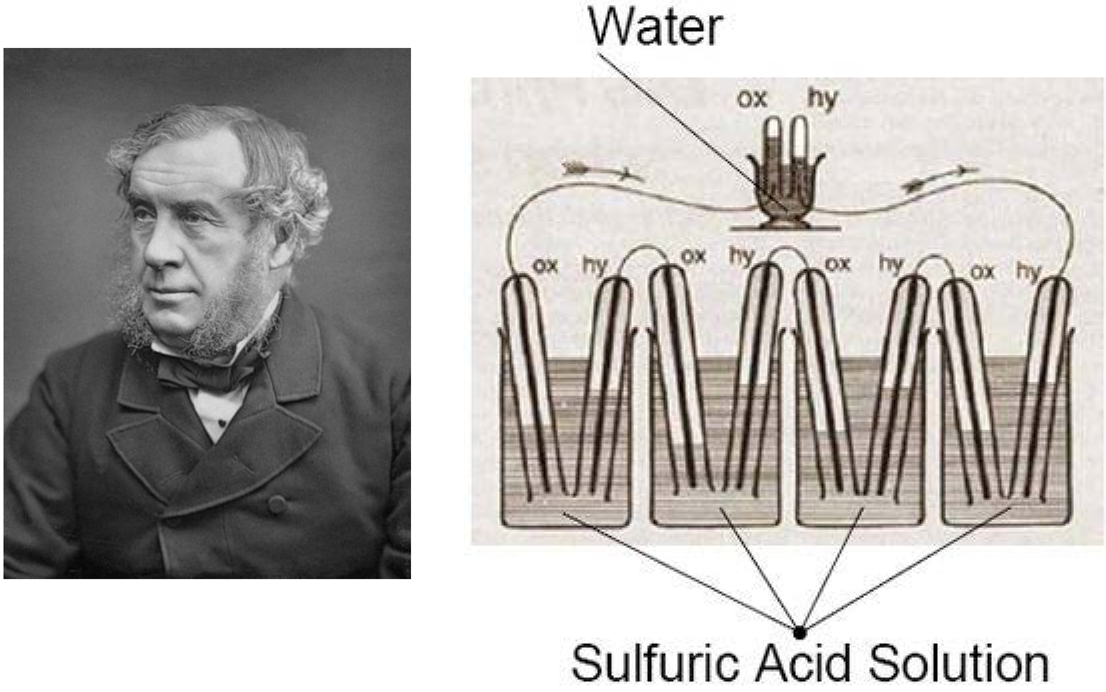

Fig. 2.1. Grove's 1839 gas voltaic battery diagram which produced electrical energy by combining hydrogen and oxygen; the term “fuel cell” was coined later in 1889 by Ludwig Mond and Charles Langer, who attempted to build the first practical device using air and industrial coal gas. (Sir William Robert Grove, PC, QC, FRS (11 July 1811 – 1 August 1896) was a Welsh judge and physical scientist. He anticipated the general theory of the conservation of energy, and was a pioneer of fuel cell technology) [**38**].

Obviously, flameless burning of hydrogen in such a fuel cell as to generate electric current was not in the ranks with direct combustion of the hydrogen in syngas for generation of electric energy in just launched electromagnetic generators. This was also long before concerns have become raised about pollution of air and the change to the environment and the climate brought by burning coal-bearing fuels for heat, electricity and mass transportation. Simply, both the economical drivers and the technology to directly convert hydrogen energy into electric energy were not in place.

Some 100 years after Cavendish's discovery of hydrogen, and only 3 years after it was realized that hydrogen sorbed from chemical or electrochemical sources causes blistering and 'embrittlement' to steel vessels, Thomas Graham [**39**] observed the ability of palladium to absorb hydrogen and wrote in Philosophical Transactions of the Royal Society of London :

"Hence palladium has taken up a large volume of gas when the temperature of the metal never exceeded 245 ℃", and again

" 1 vol. palladium held 643.3 vols. hydrogen.

By the care of my zealous assistant, Mr. W.C. Roberts, the hydrogen employed in these experiments was purified to the highest degree by passing it in succession through alcohol, water, caustic potash, and tubes of 0.7 meter each, filled with broken glass impregnated with nitrate of lead, sulphate of silver, and oil of vitriol. The gas was inodorous, and burned with a barely visible flame".

The reversible absorption was observed to proceed in presence of either metallic palladium or in palladium-silver alloys; much less hydrogen was absorbed in Cu sponge (1vol. Cu : 0.6 vol. H.), and not at all in Os-Ir. The reaction of hydrogen with palladium, so being described by Graham, was:

$$Pd + H_2 \leftrightarrow PdH_x \qquad (2.2)$$

Palladium hydride is not a stoichiometric chemical compound but simply a metal in which **hydrogen is dissolved and stored in solid-state, in space between Pd atoms of crystal lattice of the host metal.** Relatively high solubility and mobility of H in the FCC (face-centered-cubic) Pd lattice made the *Pd-H system* one of the most transparent, and hence most studied from microstructural, thermodynamic and kinetic points of view. Over the century that followed many *metal-hydrogen systems* were investigated while those studies were driven mostly by scientific curiosity. Researchers were interested in the interaction of hydrogen molecule with metal surfaces adsorption and diffusion into metals. Many reports on absorption of H_2 in Ni, Fe, Ni, Co, Cu, Pd, Pt, Rh, Pd-Pt, Pd-Rh, Mo-Fe, Ag-Cu, Au-Cu, Cu-Ni, Cu-Pt, Cu-Sn, and lack of absorption in Ag, Au, Cd, Pb, Sn, Zn came from Adolf von Sieverts and co-workers [**40-43**].

At the time when Adolf von Sieverts and co-workers reported first studies on absorption of hydrogen by metals and alloys, a series of seminal papers had been published by Avrami [**44-46**] on the kinetics of phase transformations driven by nucleation and growth of nuclei and leading to microstructural 'granulation', viz. grain size distribution in solid material. Therefore, foundations for hydrogen storage and for formation of fine and *ultra-fine-grained microstructures* in solid materials had been developing concurrently.

At that time when world emerged from the Second World War, and become falling into another Cold War with the Soviet Union, liquid hydrogen has been intensively studied as a rocket fuel. In contrast to the dangers of a new world deal, and in the climate of overwhelming optimism triggered by the end of war, hydrogen was also contemplated as the fuel of the future for a civil supersonic aircraft flying between Europe and North America, with Canadian Montreal's super-modern Mirabel airport being considered for accommodating overseas flights from Europe.

After World War II investigations of hydrides were driven mostly by nuclear reactor applications as to understand *hydride-caused embrittlement* of reactor metals, like Zr, or to take advantage of high populations of hydrogen atoms in hydrides to scatter, moderate or shield from energetic neutrons in high-temperature, mobile nuclear reactors. Zirconium alloys in water-cooled reactors, in particular, were known to pick up hydrogen, and precipitate zirconium hydrides on cooling. Therefore, zirconium-hydrogen system was the one studied in close reference to development of nuclear reactors. The first *intermetallic hydride* reported was $ZrNiH_3$ [**47**].

Now, let's come back to our other historical thread: the development of hydrided materials. Large body of results was coming in the 1960's from research on apparently nanometric structures observed in fine metal powders and deposits, like dispersed Fe, and *cathodically charged Ni layers* prepared in electrochemical cells [**48**]. Yet, the thermodynamic information extracted from such electrochemically charged metals concerned inherently non-equilibrium processes, and was considered doubtful and less of value. In fact, an important experiment on direct synthesis of nickel hydride, NiH, at 18 kbar of H_2 gas in high-pressure cell, carried out by Baranowski in Poland's Institute of Physical Chemistry in Warsaw in 1966 [**49**] was driven by desire to achieve true equilibrium conditions between H_2 gas and solid *nickel hydride* phase. At that time a common approach in investigations of metal-hydrogen systems was to conduct studies on well-ordered polycrystalline metals or, if possible, single crystals. Obviously, ordered metals used in experiments let investigators to construct the most transparent and instructive models for a metal-hydrogen system.

Although by the end of 1960's many metals were reported to form hydrides, those were either too stable, like ZrH_2, or too unstable, as NiH to attract interest in respect to *reversible hydrogen sorption*.

2.2. Historical development of classical hydrogen storage AB_5 alloys

Development of first practical hydrogen storage alloys, AB_5-type intermetallics, had its beginning in a typical accidental laboratory experimentation, although, it was predetermined by a vigorous development of a new discipline of materials science and engineering in late 1960's. The outstanding hydrogen sorption properties of rare-earth AB_5 intermetallics was accidentally discovered in Philips Laboratories in Eindhoven, Netherlands at about 1969 in a program to develop a new permanent magnet alloy [**50**]. In the work on Sm-Co magnet alloy it was observed that a loss of coercivity occurs, when magnets were aged in humid air, which was related to two concurrent reactions: corrosion of $SmCo_5$ intermetallic with release of hydrogen, and sorption of the released hydrogen by still uncorroded alloy:

$$2\ SmCo_5 + 3H_20 \rightarrow Sm_2O_3 + 10Co + 3H_2 \qquad (2.3)$$

$$SmCo_5 + 1.25\ H_2 \leftrightarrow SmCo_5H_{2.5} \qquad (2.4)$$

Zijlstra et al. [**51**] demonstrated that the reaction of Eq. (2.4) is reversible at several bars of pressure at ambient temperature. In the following studies on the origin of magnetic coercivity in these new magnets, Phillips laboratories came with the hydride of *lanthanum-nickel hydride*, $LaNi_5$, which reversibly bonded more than 6 atoms of H per one formula unit (H/M ratio >1) [**52**].

$$LaNi_5 + 3.35\ H_2 \leftrightarrow LaNi_5H_{6.7} \qquad (2.5)$$

Reversibility of hydrogen charging was very good at room temperature. This is because the hexagonal lattice of the metal host, like this of $LaNi_5$, does not undergo major transformation as hydrogen is inserted interstitially. This was the first *AB_5-type interstitial hydride*, in which hydrogen is stored between metal atoms.

Those *rare-earth AB_5 –type hydrides* were quickly utilized in rechargeable *nickel metal hydride batteries* where electrochemical hydrogen charging and discharging take place at ambient temperature. Such *electrochemical hydrogen storage* is reversible, when the negative hydride electrode (anode) is combined with the positive Ni electrode (cathode) in the battery cell.

$$AB_5H_x + xOH^- \leftarrow\rightarrow AB_5 + xH_2O + xe^- \qquad (2.6)$$

$$NiO(OH) + H_2O + e- \leftarrow\rightarrow Ni(OH)_2 + OH^- \qquad (2.7)$$

As a matter of fact, **the first hydrides with practical hydrogen storage capacities were realized in rechargeable nickel metal hydride batteries.**

Renewed interest in solid-state hydrogen storage came with first Oil Crisis in 1970's. By early 1973 a patent was granted to US Brookhaven National Laboratory, where Reilly had produced first *$MmNi_5$ alloy* for hydrogen storage [**53**]. $MmNi_5$, **where Mm-mischmetal is** unrefined (cerium free) **mixture of rare-earth metals, mostly La and Nd**, obtained from Bastanite from California (also found in large deposits in Inner Mongolia, China), **was much less expensive** than La and has already been used as deoxidizer in steel industry. Soon after, the potential for energy-related application for nickel and nickel alloys attracted the major Ni metal and alloy producer in Canada and the USA, INCO. Garry Sandrock, then with INCO, achieved optimization of $MmNi_5$ compositions for gas hydrogen storage through careful partial substitutions for A and B in AB_5 formula [**54**]. The compositional changes have reduced the raw materials costs to about 30 % of that for the $LaNi_5$ alloy.

$LaNi_5$ has an attractive value of the equilibrium hydrogen desorption pressure dropping in the range between 1 to 2 atmospheres at 25°C. In the $MmNi_5$ this pressure rises to a much less attractive 30 atmospheres, which can imply difficult engineering design for gas hydrogen storage, and was completely impractical in $MmNi_5$ used for the anode in a Ni-MH battery cell; obviously battery cells operate at near-atmospheric pressure. The substitutions of $MmNi_5$ with Ca for Mm and Al for Ni were quite effective in lowering the equilibrium pressure of hydrogen back to about 1-2 atmospheres at 25°C, which was desired for easy hydrogen charging and discharging at ambient conditions. Approaches along the same line came in the same time from Japan [**55**]. The alloying of polycrystalline AB_5 alloy was an excellent (and very practical) result of new materials design involving adjustment of the strength of chemical bonds between metallic elements in AB_5 hexagonal lattice and its interstitial hydrogen atoms. The bond strength in the metallic host lattice was further optimized with Co substitutions which was effective in reducing the volume change on hydriding of the hexagonal AB_5 unit [**56**]; the density of material can, indeed, be related to the bond length, R_o, through an approximate formula: $R_o=0.0115\ A_{av}/a^2c$, where A_{av} is an average atomic weight for the AB_5 formula unit, and the a and c are the hexagonal lattice parameters in nanometers [**57**]. The lower dilatation of the AB_5 unit cell on placing hydrogen in it was equivalent to better cohesiveness of atomic structure in this intermetallic, hence improved

resistance to alloy **decrepitation on repetitive (cyclic) charging and discharging, hence better corrosion resistance of $MmNi_5$ alloys in an aggressive caustic battery electrolyte**.
Although substitution with Al came at the price of the lowered hydrogen capacity, another Mn substitution ameliorated this problem [58]. With compliance with the well-observed 10-15 year shift from new material development to its full commercialization, the Al and Mn substitutions have been combined in multi-element $MmNi(Co, Mn, Al)_5$ battery alloy and optimized for the use in anodes in Ni-MH commercial batteries. A typical commercial AB_5 alloy can consist of many elements, like in Hydroalloy F from GfE Metallen und Materialen GmBH: $(La_{0.64}Nd_{0.36})Ni_{0.95}Cr_{0.19}Mn_{0.41}Co_{0.15}$ (in wt.%) [59]. Again, one can observe how the development of materials for gas hydrogen storage for fuel cells has been intertwined with a parallel development of alloys for electrochemical hydrogen storage in rechargeable battery cells.

2.3. Historical development of interstitial hydrides in other intermetallic systems

The first systematic research into **gas hydrogen storage** for practical applications began in the early 1970's at the Brookhaven National Laboratory (BNL) on New York's Long Island. The investigations were conducted in a program that explored possibility of **storing electric energy produced in off-peak hours by nuclear power stations through generation of hydrogen, and then the storage of hydrogen in metals instead of storing electric current.** So, at the same time as the AB_5-group hydrides were intensively investigated in the BNL, new *AB-type hydrides* came into view. *Iron-Titanium*, FeTi, hydride was discovered in 1974 by Reilly and Wiswall [60] in the same Brookhaven National Laboratory. This metal hydride formed from a 50-50 atom ratio of titanium and iron, the lowest cost and the most convenient hydride, offered a reversible capacity of almost 1.5 wt.% H_2 operating at ambient temperatures. A desirable feature of this new hydride was that the hydriding-dehydriding reaction occurs near ambient temperature and during the charging pressure ranges between 500 and 15 psi. The prototype 400 kg FeTi hydride storage unit was built by a New Jersey's electric utility. The charge-discharge reactions were observed to be very rapid **but strongly limited by the rate of heat transfer**. FeTi material was not losing hydrogen storage capacity even after thousands of cycles when high-purity hydrogen was used. Yet, **the alloy was very sensitive to O_2 and CO poisons**, **and even to traces of H_2O**. Obviously, while meeting expectations of stationary storage of nuclear energy in form of solid hydride **it was too heavy for storage of hydrogen for transportation energy**. Anyway, the needs for cars propelled by hydrogen fuel were not in place at the end of 1970's.

2.4. Historical development of AB_2 intermetallic hydrides [61]

The AB_2's are largely based on two related Laves phase crystal structures: hexagonal (prototype $MgZn_2$, Strukturbericht C14, Pearson hP12, space group P63/mmc) and cubic (prototype $MgCu_2$, Strukturbericht C15, Pearson cF24, space group Fd-3m). The most typical AB_2 intermetallic alloys are as follows (at.%): $TiCr_{1.8}$, $TiMn_{1.5}$, $ZrMn_2$, $Ti_{0.98}Zr_{0.02}V_{0.43}Fe_{0.09}Cr_{0.05}Mn_{1.5}$, $ZrFe_{1.5}Cr_{0.5}$ and $TiMn_{1.4}V_{0.62}$. As can be seen B can be either one or multi-element group (see Table 1.4 for their hydrides).

The first reported Laves phase hydrides were reported in the 1950s and 1960s by principal USA authors Trzeciak, Pebler and Beck. Practical AB_2 hydrides were identified in the 1970s by groups led by Shaltiel (Israel), Gamo (Japan), Buschow (Netherlands), Wallace (USA), Reilly (USA), Burnasheva (USSR) and others. The AB_2 alloys do offer significant advantages over the AB_5's in cost, at least if the A-element is mostly Ti and not Zr.

It is to be pointed out that pure V is a very expensive element compared to ferrovanadium, a low-cost product used by the steel industry. Therefore, V-containing alloys should also have some Fe present to allow the use of low-cost ferrovanadium.

AB_2 alloys are generally somewhat more difficult to activate than AB_5's, although some will activate without heating, especially those higher in Zr or Mn (as opposed to Ti and Cr). Once activated, hydriding/dehydriding kinetics are usually high.

2.4. Historical development of lightweight metals hydrides and hydride complexes

Formation of a *magnesium and calcium hydride* compounds was first recognized by German chemists yet at the end of 19th century [62] but it took more than a half a century before a substantial yields of Mg hydride was obtained from direct synthesis of the elements and the first determination of values for the decomposition pressure on temperature, the enthalpy of formation and the activation energy were obtained [63]. Since then, Mg metal with its hexagonal lattice was well researched for hydrogen storage in the interstitial magnesium dihydride phase.

$$MgH_2 \leftarrow\rightarrow Mg + H_2 \qquad (2.8)$$

Magnesium dihydride can store several times as much hydrogen per unit weight as AB-type TiFe hydride. One problem with hydriding metallic Mg is that **it does not react with hydrogen at low temperatures, and reacts only very slowly at high temperatures.** Because of the relative inertness with respect to hydrogen Mg was even recommended as a structural metal suitable for contact with hydrogen up to the melting temperature [sic!]. Not surprisingly, many controversial and poor reproducing data have been published on the hydrogenation/dehydrogenation kinetics. The natural inertness of Mg to molecular hydrogen can be attributed to well-known factors: (i) thick surface oxides that cover magnesium metal do not provide sites catalytically active for dissociation of hydrogen molecule, which is known to occur on contact with a metallic surface (clean metallic surface often provides active sites for catalytic breaking of very strong H-H bond); (ii) surface adsorbed impurity gases further slows the kinetics of hydrogen absorption into the bulk grains.

Dehydrogenation of magnesium hydride (MgH_2) can only be achieved **by heating at about or above 300°C** which is the results of its **high enthalpy of dehydrogenation** (it will be discussed in more detail later). Stable MgH_2 was prepared as early as 1951 by direct heating of Mg in gaseous hydrogen under high pressures, however, reaction was slow and difficult to complete [**64**]. While the chemical reactivity of Mg metal to hydrogen is poor it was early realized in works by Dymova et al. [**65**] that its dihydride can be a strong chemical reducer, and its increased reactivity depends strongly on small grain size. So the effect of grain size was pointed on as being one of high importance.

Mg_2Ni alloys and *magnesium-nickel A_2B –type complex hydrides***,** Mg_2NiH_4 were well known, being first developed in the US Brookhaven National Research Laboratory [**60**], and studied in Nordic countries [**66**], where the interest in Mg has been stimulated by availability of hydropower required to produce Mg metal in the first place. (Even earlier, Pebler studied A_2B-type hydride of Zr_2Ni [**67**]). The new Mg_2Ni alloy alleviated the problem inherent to Mg metal: very poor kinetics of hydrogenation reaction. Reilly and Wiswall [**60**] noticed that by the presence of intermetallic magnesium compounds, Mg_2Ni and Mg_2Cu, on the Mg surface this reaction can be greatly accelerated. The hydrogen release can proceeds without major crystallographic transformation as the hydride is converted back to the Mg_2Ni:

$$Mg_2NiH_4 \leftrightarrow Mg_2Ni + 2H_2 \qquad (2.9)$$

2.5. Early studies of non-interstitial transition metal ternary hydrides

With the beginning of the 1990's an interest was somehow refocused. Firstly, came interest in other hydrides of Mg with transition metals, beyond already well-researched Mg_2Ni stoichiometry. Mg and Fe does not alloy to form Mg_2Fe binary intermetallic by either ingot casting or metal powder sintering procedures, however, when sintering is done in hydrogen, a very stable Mg_2FeH_6, *non-interstitial, ternary magnesium-iron hydride* forms [**68**]. The Fe and Co *transition metal hydrides* (in reality they are *complex* hydrides) with Mg were firstly synthesized in the University of Geneva in 1991 in the same group that observed formation of this hydride during sintering of powders. While presenting a formal derivative of A_2B stoichiometry, the hydrides were, in essence, Fe-metal and Co-metal *hydride anionic complexes* [**69**]. The new anionic complexes of Fe and Co were stable rendering the desorption temperature too high. When desorbed, the hydrides could not change to the hydrogen-free A_2B alloys because Mg_2Fe and Mg_2Co do not exist in the binary Mg-Fe and Mg-Co systems (e.g., iron and magnesium are immiscible in the solid state and form a large miscibility gap in the liquid state) and in contrast to Mg_2Ni ((2.9)), dehydrogenation reaction occurs through the formation of intermediate MgH_2 as shown below:

$$Mg_2FeH_6 \rightarrow 2MgH_2 + Fe + H_2 \qquad (2.10)$$

One can notice that in Eq. (2.10) the Fe^{3+} in the (FeH_6) complex is reduced to metallic Fe, the process that requires a major rearrangement of atoms. Therefore it is not surprising that the kinetics of desorption was poor while being controlled by diffusion of the metal atoms.

Although more research had been coming, particularly from groups in the University of Geneva and in Stockholm, research on Mg_2FeH_6 and similar transition-metal complex hydrides was put aside for some time. Some other ternary hydrides formed with alkali earths and transition metal complexes, viz. $BaReH_6$ [**70**], exhibited interesting storage properties: desorption below 100°C and 2.7 wt.% H_2 capacity at very high volumetric density of 134 g H_2/L. However, this hydride is too expensive for any practical applications.

A stable *aluminum hydride*, AlH_3, has been known to exist since some time. It has been prepared by various techniques including the direct reaction of metallic Al with atomic hydrogen by Siegel [**71**]. AlH_3 is soluble in ether when freshly synthesized but **polymerizes while aged and forms** insoluble precipitate which structure depends on the degree of polymerization of -(AlH_3)-monomer.

2.6. Towards chemical/complex hydrides

Of particular interest became complex hydrides with participation of alkaline metal ions and metal complexes and in mixed ionic and covalent coordination compounds. This class of hydrides has become known as *chemical* or *complex* hydrides. Among them are *non-transition metal sodium* and *lithium alanates* and *borohydrides.* The two most investigated are *sodium aluminum hydride (sodium alanate)*, $NaAlH_4$, and *sodium borohydride*, $NaBH_4$. The former, alanate, was synthesized almost two decades earlier in Russia by Dymova et al. [72]. Those complex hydrides were not thought to be suitable for solid-state hydrogen storage media as they release hydrogen irreversibly at conditions that are outside the temperature-pressure range desirable for fuel cell propelled cars. In particular, their hydriding and dehydriding characteristics have been creating significant challenges. This opinion has been changed with a breakthrough work by Bogdanović and Schwickardi [73], who discovered that the addition of Ti compound (chloride) to the complex hydride $NaAlH_4$ causes reversible hydrogen storage in the range up to 3.7 wt.%H_2 under moderate conditions of temperature and pressure. However, the reaction has long been known to proceed in two steps [74]

$$NaAlH_4 \leftrightarrow 1/3\ Na_3AlH_6 + 2/3\ H_2 \rightarrow NaH + Al + 3/2\ H_2 \qquad (2.11)$$

and again, like in the reaction of Eq. (2.11), the completely discharged phase did not form an alloy, NaAl, from the original metals; instead alanate is reduced to metallic Al, in fact *nanoaluminum* that do not easy recharge with H_2.

Since then, search for new reversible lightweight complex hydrides was heating up. Interest aroused in other complexes of hydrogen with Al and B that have been known since 1950's. Alkali metal and magnesium tetrahydroborides were synthesized [75, 76] and investigated by Germans and Russians for thermal decomposition from the late 1950's to the early 1970's. *Lithium tetrahydroboride, $LiBH_4$*, which have already been known as a strong reducing agent in organic synthesis, have received renewed attention after Züttel [77] reported the onset of hydrogen desorption at approx. 200°C promoted by SiO_2 admixed to this borohydride. Among the alanates, the sodium alanate and the lithium alanates has been well studied. *Magnesium aluminum hydride (magnesium alanate)*, $Mg(AlH_4)_2$, with the total 9.3 wt.%H_2 , has been known since its synthesis by Wiberg in the 1950’s, however, there have been difficulties with good reaction yield to produce this hydride until more than 50 years later Fichtner and colleagues [**78**] produced a sufficiently pure compound for structural investigations. Again, the reversibility of the reaction was questionable as the experiments so far demonstrated that after discharge of hydrogen the alanate yields Al phase, not unlike sodium alanate in the reaction of Eq. (2.11). Nevertheless, the intensive research on complex hydrides has established itself solidly in place in early years of the new Millennium.

3. THERMODYNAMICS OF SOLID STATE HYDRIDES

3.1. General thermodynamic quantities

First, it is important to explain/remind some fundamental thermodynamic quantities [**79**, **80**].

Enthalpy (H)

The **sum of the internal energy of the system (E_{sys}) plus the product of the pressure of the gas (P) in the system and its volume (V)**:

$$H_{sys} = E_{sys} + PV \qquad (3.1)$$

After a series of rearrangements, and if pressure if kept constant, we can arrive at the following equation:

$$\Delta H_{sys} = q \text{ (at constant pressure)} \qquad (3.2)$$

where ΔH is the H_{final} minus $H_{initial}$ and **q is heat.**

Enthalpy of Reaction/Formation (ΔH)

Standard Heat (Enthalpy) of Formation, **ΔH_f^0**, **of any compound is the enthalpy change of the reaction by which it is formed from its elements, reactants and products all being in a given standard state.** By definition, **the standard enthalpy (heat) of formation of an element in its standard state is zero**, **$\Delta H_f^0 = 0$.**

Standard Molar Enthalpy (Heat) of Formation, **ΔH_m^0**, of a compound is the enthalpy change that occurs when one mole of the compound in its standard state is formed from its elements in their standard states.

Standard Enthalpy (Heat) of Reaction, ΔH^0, is the difference between the standard enthalpies (heats) of formation of the products and the reactants.

$\Delta H^0_{(reaction)}$ = the sum of the enthalpy (heat) of formation of products - the sum of the enthalpy (heat) of formation of reactants:

$$\Delta H^0_{(reaction)} = \Sigma H^0_{f(products)} - \Sigma H^0_{f(reactants)} \tag{3.3}$$

By looking at whether **q is exothermic or endothermic** we can determine a relationship between ΔH and q. If the reaction **absorbs heat** it is **endothermic** meaning the reaction consumes heat from the surroundings so **$q>0$** (positive). Therefore, at **constant temperature and pressure**, by the equation above, if **q is positive then ΔH is also positive** (Fig. 3.1a). And the same goes for if the **reaction releases heat**, then it is **exothermic**, meaning the system gives off heat to its surroundings, so **$q<0$** (negative). If q is negative, then ΔH will also be negative (Fig. 3.1b).

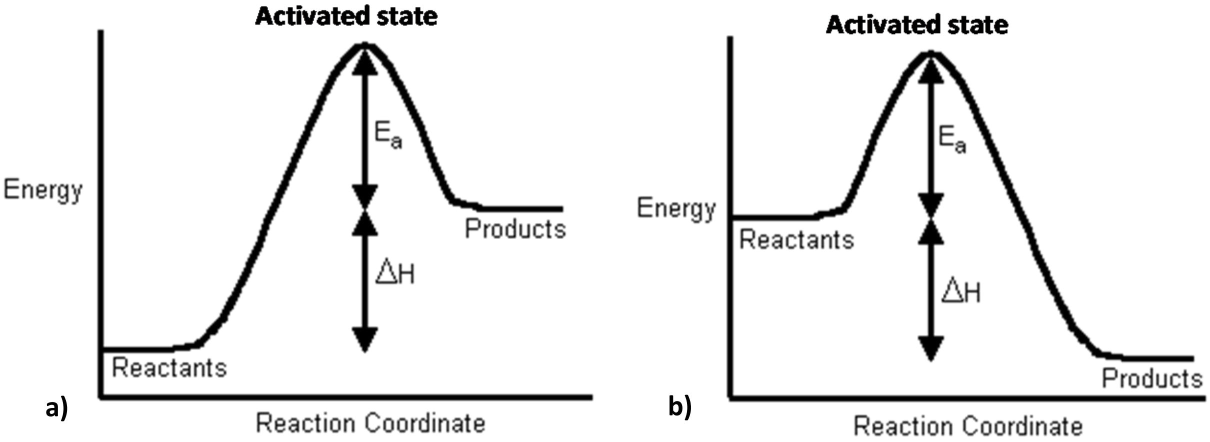

Fig. 3.1. (a) **Endothermic** reaction in which a system ABSORBS heat from its surroundings; ΔH is positive (**$\Delta H>0$**). (b) **Exothermic** reaction in which a system RELEASES heat to its surroundings; ΔH is negative (**$\Delta H< 0$**). E_a – the **activation energy**. **ΔH** can also be considered as a **driving force** for reaction.

Arrhenius equation

The activation energy (E_a) which is shown in Fig. 3.1 is the energy level that the reactant molecules must overcome before a reaction can occur. It is calculated from the Arrhenius equation in the form:

$$k = Ae^{-Ea/RT} \qquad (3.4)$$

where k is the rate coefficient, A is a constant, E_a is the activation energy (Fig. 3.1), R is the universal gas constant, and T is the temperature (in kelvin). R has the value of 8.314 x 10^{-3} kJ $mol^{-1}K^{-1}$.

By taking natural logarithm of both sides the equation can be presented in a linear fashion:

$$\ln k = -E_a/R(1/T) + \ln A \qquad (3.5)$$

Now the equation is in a linear form: y= mx+b. When the lnk (rate constant) is plotted versus the inverse of the temperature (kelvin), the slope is a straight line as shown in Fig. 3.2. The value of the slope (m) is equal to -Ea/R where R is a constant equal to 8.314 J/mol-K. It is now easy to obtain the value of E_a (negative sign means a negative slope not E_a).

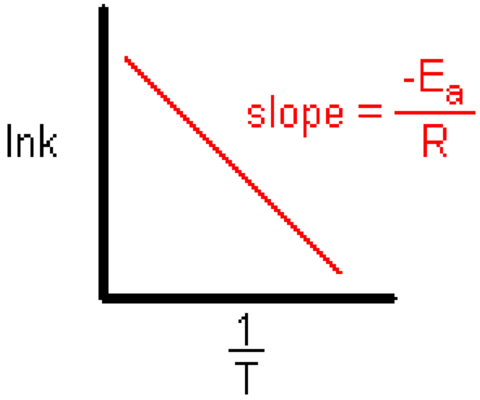

Fig. 3.2. Arrhenius equation plotted as a straight line.

3.2. Pressure-Composition-Temperature (PCT) properties

Pressure-Composition-Temperature (PCT) curve called also Pressure-Composition Isotherm (PCI) curve can be a source of important fundamental information related to thermodynamic properties of solid hydrides. There are several methods of determining PCT properties ranging from thermogravimetric to precise volumetric measurements obtained by using a classical Sieverts-type apparatus. The thermogravimetric methods unfortunately are extremely limited in pressure applied during test to the maximum 2 MPa, which is usually around equilibrium pressure only for low capacity hydrides. The plateau pressure at the decomposition temperature for high capacity hydrides is much higher and sometimes reaches hundreds of MPa.

A typical isotherm of a reversible hydride is shown in Fig. 3.3. By measuring the changes in hydrogen pressure and corresponding changes in hydrogen concentration in metal at a given temperature, PCT curves can be constructed that are expected to give a flat plateau. Most practical hydrides do not show perfectly flat plateau or zero hysteresis. Sloping behavior is observed possibly due to different equilibrium pressure, localized defects and surface inhomogeneities [81].

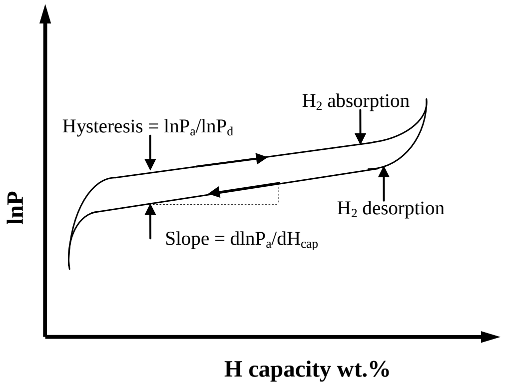

Fig. 3.3. Schematic isothermal pressure-composition hysteresis loop [10].

The effect of temperature on the PCT curves is shown in Fig.3.4a. The metal initially dissolves only small amount of hydrogen (<0.3wt.%) which creates a solid solution of hydrogen in a metal matrix α-phase. As the hydrogen pressure and hydrogen concentration in the metal are increasing, interactions between hydrogen and metal atoms become locally important and nucleation and growth of a new metal hydride β-phase is observed. In the plateau region there exists a mixture of solid solution α-phase and metal hydride β-phase. The length of plateau determines how much H_2 can be stored reversibly with a small pressure variation. It can be seen in Fig.3.4a that increasing temperature increases plateau pressure and beyond the critical temperature T_c, plateau region disappears and the α phase converts to the β phase continuously.

The relation between mid-plateau pressure P and temperature T is given by the well-known **Van’t Hoff equation**:

$$\mathbf{\ln(P/P_0) = -(\Delta H/RT)+\Delta S/R} \tag{3.6}$$

where P_0 is atmospheric pressure, ΔH and ΔS are enthalpy and entropy changes of the hydriding/dehydriding reaction, respectively, T is the absolute temperature and R is the gas constant (8.314472 J/mol·K). For a number of hydrides the *enthalpy* and *entropy* of *hydriding* reaction are negative i.e. the hydriding reaction is *exothermic* and dehydriding reaction is *endothermic* (Fig.3.1). **To avoid confusion, both ΔH and ΔS are always expressed per 1 mol H_2.** The knowledge of ΔH is especially important to the heat management required for practical engineering devices and is a fundamental measure of the M–H bond strength.

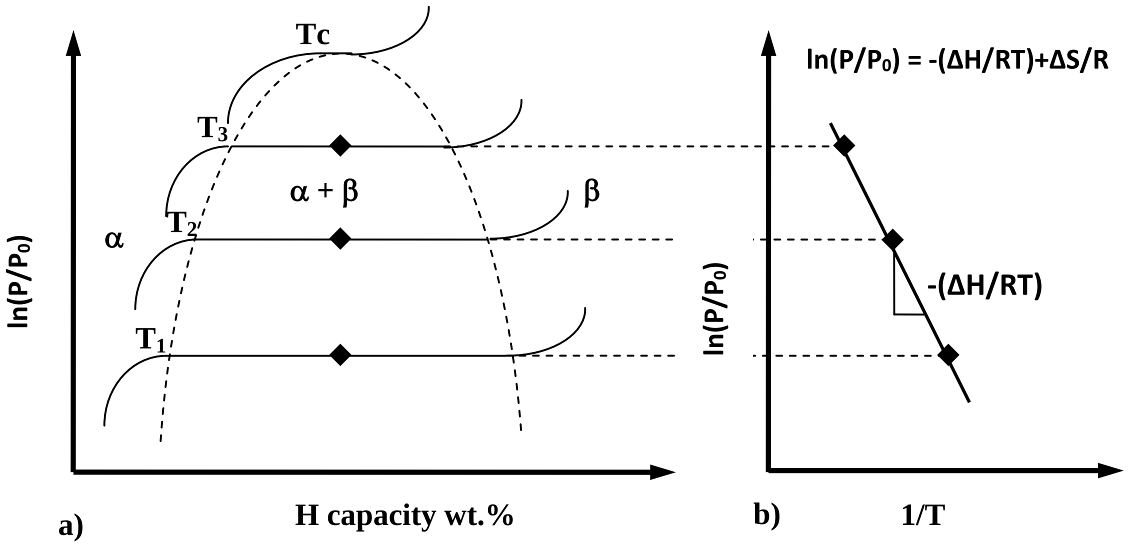

Fig. 3.4. (a) Pressure-Concentration-Temperature plot and (b) Van’t Hoff plot [10].

The enthalpy of absorption and desorption process *ΔH* can be determined from the slope (ΔH/R) using the Van’t Hoff plot (logarithm of the mid-plateau pressure against the reciprocal temperature: lnP vs. 1/T (or more preferably 1000/T)(where P is most conveniently given in atm.) presented in Fig.3.4b. The enthalpy term characterizes the stability of metal-hydrogen bond and the operating temperature of the metal hydride is fixed by the plateau pressure thermodynamically and by the overall reaction kinetics. The entropy term corresponds mostly to

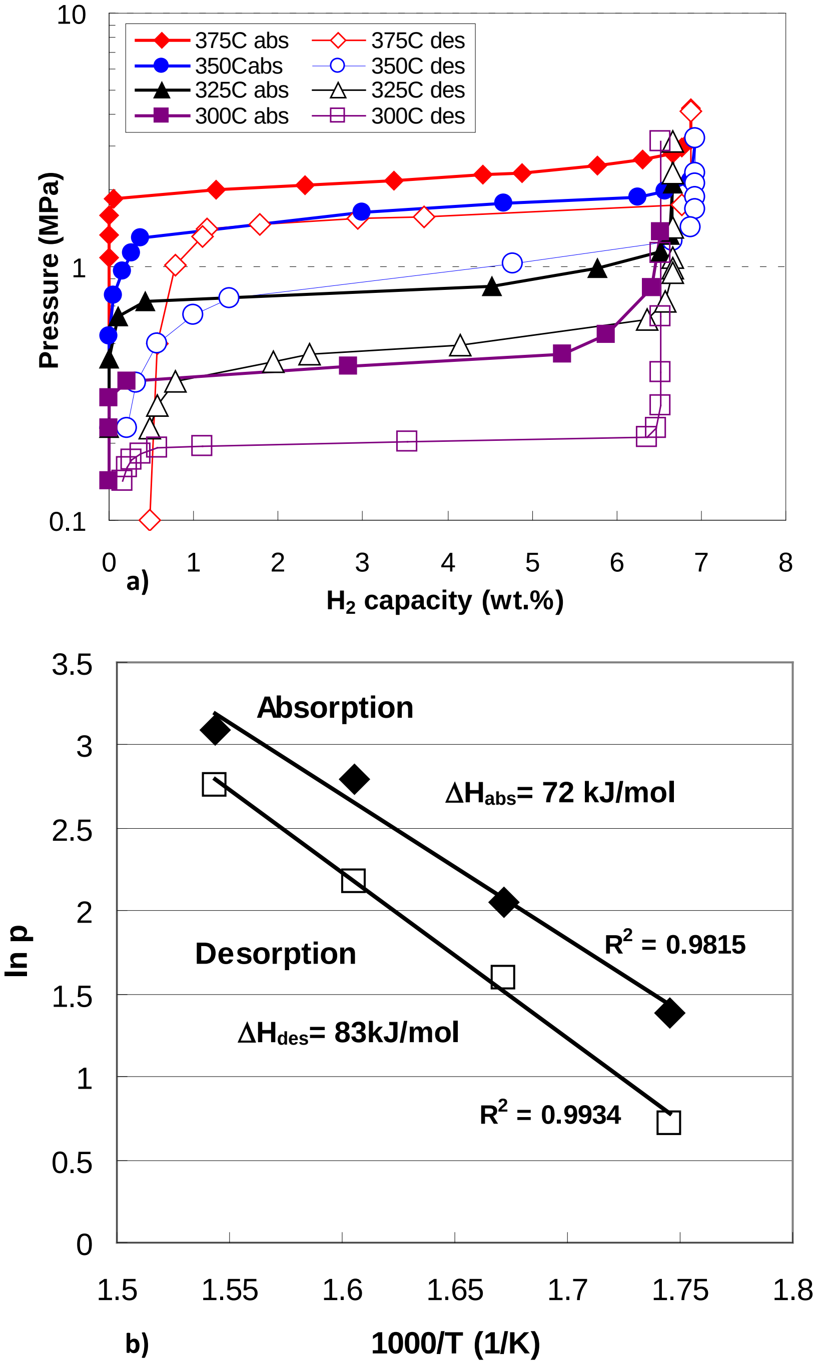

Fig. 3.5. (a) PCT curves for absorption and desorption of the MgH_2 (designation Mg6H in [10]) powder reactively synthesized for 150 h. (b) Van't Hoff plot (ΔH_{abs}=72 kJ/mol, ΔH_{des}=83 kJ/mol, ΔS_{abs}=138 J/molK and ΔS_{des}=151 J/molK) [10].

the change from molecular hydrogen gas to dissolved atomic hydrogen and is more or less constant for all hydrides.

A typical example of PCT curves and resulting enthalpies of formation from the Van't Hoff plot for the MgH_2 hydride synthesized by **reactive milling** of metallic Mg under 880 kPa H_2 pressure for 150 h is shown in Fig. 3.5 a and b, respectively. XRD measurements revealed that powder **particles contained nanograins about 8 nm in size** with 0 lattice strain (powder Mg6H in [**10**]). The powder after such a long reactive milling contains both γ-MgH_2 and β-MgH_2 [**10**]. In order to eliminate the presence of γ-MgH_2 and its effect on PCT curves, the powder was desorbed at 350°C under pre-vacuum for 60 min. Subsequently, absorption/desorption cycles for acquiring PCT curves were conducted as follows:

(1) Abs-350°C; des-350°C; annealing 325°C/pre-vacuum/30min-temperature stabilization.
(2) Abs-325°C; des-325°C; annealing 300°C/pre-vacuum/30min-temperature
(3) Abs-300°C; des-300°C; annealing 375°C/pre-vacuum/30min-temperature stabilization.
(4) Abs-375°C; des-375°C.

The plateau region on the PCT curves in Fig. 3.5a is relatively flat, showing only a minimal slope. However, each absorption-desorption pair of PCT curves clearly exhibits **a pressure hysteresis** (as already shown in Fig. 3.3). This means that the pressure needed for absorption (hydride formation), P_{abs}, is always greater than that of hydride decomposition, P_{des}. The cause of pressure hysteresis in metal-hydride systems is not fully understood. A number of models which attempted to explain this phenomenon have been proposed throughout the last 70 years. Models developed up to 1992 were reviewed by Qian and Northwood [**82, 83**] and Esayed and Northwood [**84**]. **A general observation is that PCT pressure hysteresis seems to be an inherent feature of all metal-hydrogen systems.** If hysteresis is measured by the ratio P_{abs}/P_{des}, its degree usually **decreases with increasing temperature** (or increases if it is measured as ΔP) which is quite clearly observed in Fig. 3.5a.

As shown in Fig. 3.5b the enthalpy of absorption and desorption, calculated from the Van't Hoff plots using the mid-plateau pressures of PCT curves in Fig. 3.5a is equal to -72 kJ/molH_2 and 83 kJ/molH_2, respectively. The value of entropy is 138 J/molK and 151 J/molK for absorption and desorption, respectively. The enthalpy value for absorption is very close to the other values found in the literature for MgH_2 [**10**]. Surprisingly, however, the enthalpy of desorption at 83 kJ/molH_2 is greater than the former one and also greater than the enthalpy of desorption of the as received and activated MgH_2 (71 kJ/molH_2)[10]. The coefficients of fit are excellent which gives good credibility to the obtained values.

The cause of greater enthalpy of desorption than that of absorption for the synthesized and desorption/absorption cycled MgH_2 is not well understood. The γ-MgH_2 originally present after reactive milling synthesis was eliminated from the microstructure by desorbing the reactively synthesized powder at 350°C under pre-vacuum for 60 min, so this factor could not affect the results. Particle size is stable during any further thermal processing of ball milled MgH_2 without any sintering which could affect the average size, so this factor can also be eliminated. Another factor, grain size of MgH_2, usually grows rather quickly in milled powders to about 60-80nm range after desorption at 350-400°C (Table 2.13 in [10]). Since the synthesized powder was desorbed at 350°C under pre-vacuum for 60 min its grain size should be in this range. During further thermal cycling the grain size becomes rather stable without measurable growth [10]. Also, this factor seems not to be responsible for the greater desorption energy. However, in general, as has been shown in [10], the kinetics of desorption process of ball milled MgH_2 powders are always more sluggish than that of absorption. Apparently, in view of our results, desorption process is also more difficult thermodynamically having greater enthalpy than its absorption counterpart.

Hydrogen capacity H_C in Fig. 3.6 can be expressed in either atomic H/M ratio (H-number of H atoms, M-number of metal atoms) or weight percent (wt.%), both of which are commonly used [61]. It must be noticed that calculating wt.% both atomic mass of hydrogen m_H and atomic masses of metal/non-metal m_M (not only mass of metal) must be considered in the denominator.

$$H_C = \frac{m_H}{m_{Hydride}} \text{x}100\% \quad [\text{wt.\%}] \qquad (3.7)$$

where $m_{Hydride}$ – mass of hydride = $m_M + m_H$ as shown earlier in Sec. 1.4.

Capacity presentation in wt.% is very useful from technological point of view, because it gives direct information on how much of hydrogen can be stored in a material. Regardless of the units, there are several ways to express hydrogen capacity. The reversible capacity $\Delta(m_H/m_{Hydride})_R$, is conservatively defined as the plateau width, which can be considerably less than the maximum capacity $\Delta(m_H/m_{Hydride})_{max}$ (Fig.3.5). In practice, depending on available pressure and temperature ranges, engineering capacity is usually between reversible and maximum capacity.

Substituting P=1 bar (or 1 atm) in Eq. 3.6 one can find a simple relationship between the equilibrium temperature ($T_{plateau}$) required to give a mid-plateau pressure of 1 atm H_2, ΔH and ΔS in the following form

$$\Delta H = \Delta S T_{plateau} \tag{3.8}$$

Eq. 3.8 is plotted for a number of hydrides in Fig. 3.7. As can be seen all the data points fit very well a simple straight line whose slope is equal to **ΔS≈ 130 J/mol•K** [85]. This clearly shows

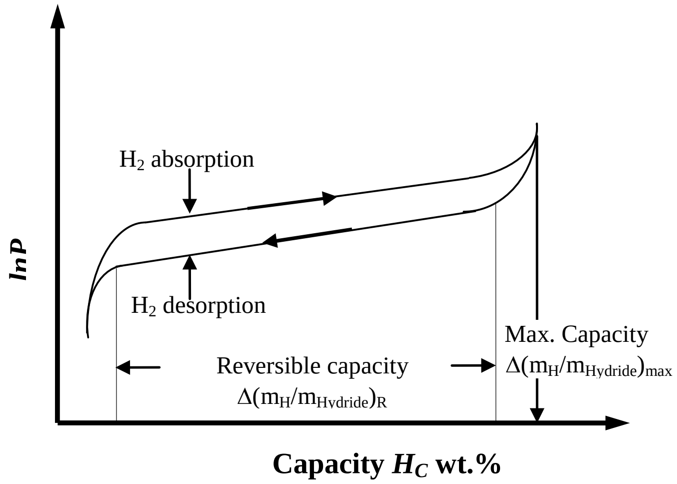

Fig. 3.6. Schematic presentation of hydrogen capacity defined by various methods [10].

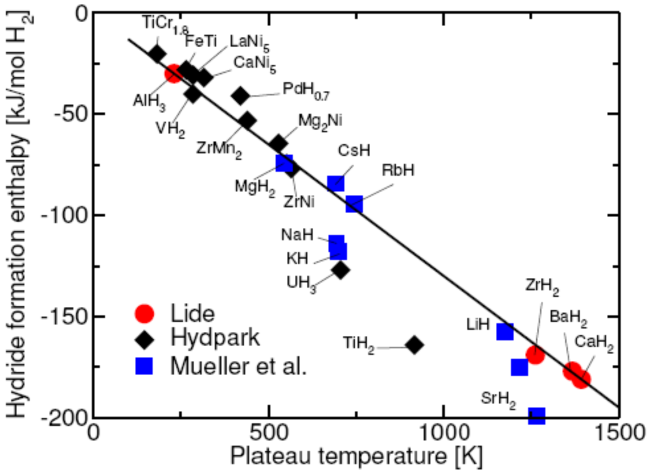

Fig. 3.7. Hydride formation enthalpy, ΔH, per mole H_2 as a function of the plateau temperature at 1 bar. The plateau temperature is calculated from reported thermodynamic parameters using the Van't Hoff equation [85].

that the entropy term is, indeed, a nearly constant value for all the solid state hydrogen systems. Fig. 3.7 also shows that a low desorption temperature at 1 bar/atm of pressure (**more or less an operating pressure of a PEMFC** as discussed earlier) can only be achieved with hydrides having the formation/decomposition enthalpies **not larger than 50 kJ/molH$_2$**. For example, hydrides which desorb at room temperature such as LaN$_5$ and TiFe have **ΔH ~ 30 and 33.3 kJ/molH$_2$**, respectively [86]. However, **too small an enthalpy term would require T$_{plateau}$ at 1 atm to be much below 0°C**. From this point of view the enthalpy term is one of the most important factors characterizing any hydride.

3.3. Calculation of activation energy

Thermodynamics can be used only to calculate enthalpy of transformation but it cannot say **how fast a transformation will proceed**. The study of how fast process occurs belongs to kinetics which in turn is related to the activation energy, E_a (Fig. 3.1).

The **first method** of calculating the activation energy is the ***Kissinger* method** [87] which is based on Differential Scanning Calorimetry (DSC) analysis of decomposition or formation processes and related to these reactions endo- or exothermic peaks position connected with heating rate. The **second method** is based on **the *Arrhenius* equation** and determination of formation or decomposition rate from kinetic curves obtained at various temperatures. The critical point in this method is a selection of correct model to estimate the rate of reaction.

The Kissinger method

By performing the Kissinger analysis [87], i.e. an analysis of the sensitivity of the DSC temperature peak positions, T_m, to the applied heating rate, β, the apparent activation energy, E_a, can be obtained from the following equation:

$$d\ln(\beta/T^2_m)/d(1/T_m) = -E_a/R \qquad (3.9)$$

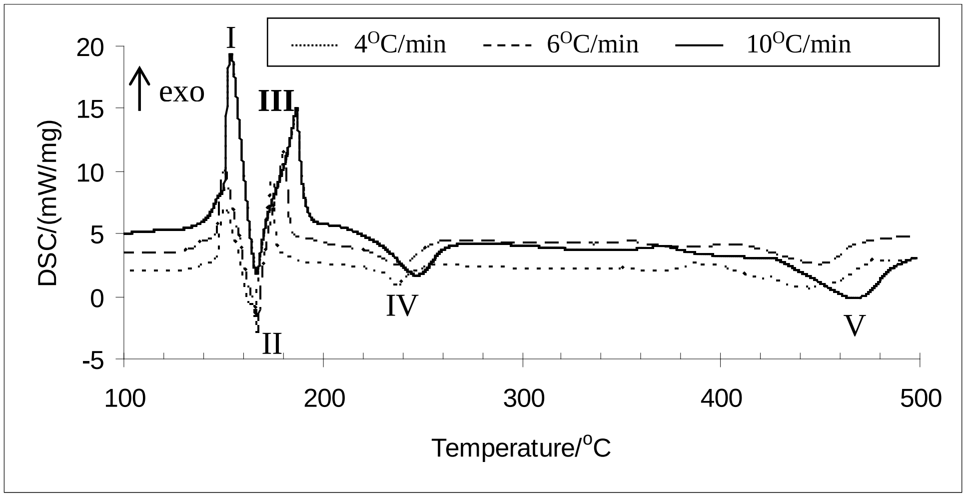

Fig. 3.8. Dehydrogenation of as-received $LiAlH_4$ investigated by DSC [10].

Table 3.1. The temperatures of peaks connected with various processes during thermal dehydrogenation of as-received $LiAlH_4$ investigated by DSC [10].

Heating rate °C/min	Temperature/°C				
	I	II	**III**	IV	V
4	150.76	166.04	**174.83**	237.35	447.09
6	150.32	167.33	**180.90**	238.30	449.26
10	153.69	166.66	**186.67**	246.98	466.59

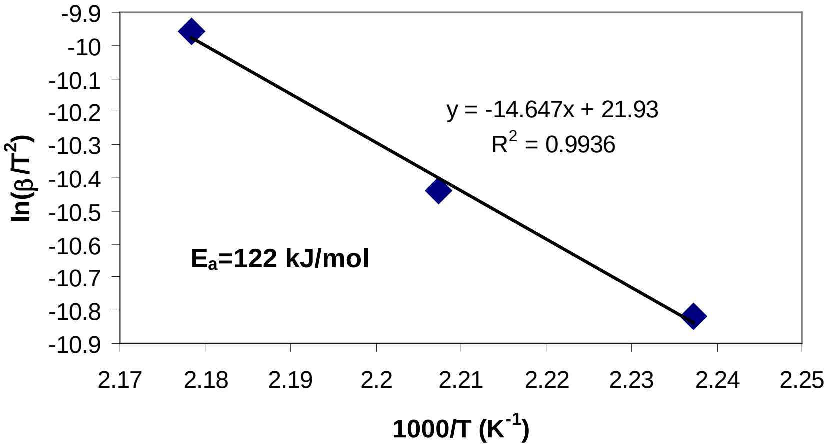

Fig. 3.9. Kissinger plot for dehydrogenation of as-received $LiAlH_4$. The activation energy, E_a, for the decomposition $LiAlH_4 \rightarrow$ **⅓Li_3AlH_6 +⅔Al+H_2** (**peak III** in Fig. 3.8) [10].

In Fig. 3.8 and Table 3.1, a typical DSC peak position shift related to various heating rates for thermal decomposition of $LiAlH_4$ is presented. Fig. 3.9 shows a Kissinger plot for dehydrogenation of $LiAlH_4$ (lithium alanate). Thus, E_a can be obtained as the slope in a plot of $\ln(\beta/T_m^2)$ versus $1000/T_m$ (Fig. 3.9). It must be mentioned that the E_a values obtained from the Kissinger method **are not always equal/similar to those obtained by the JMAK method below**.

Calculation of activation energy from the JMAK model and the Arrhenius equation

The hydrogen absorption/desorption kinetics are more commonly analyzed by applying the **JMAK (Johnson-Mehl-Avrami-Kolmogorov) theory of phase transformations** which is based on **nucleation and growth** events [88-90] where α **is the fraction transformed at time** ***t*** **or alternatively for hydrides the fraction absorbed**

$$\alpha = 1 - e^{-(k \cdot t)^{\eta}} \tag{3.10}$$

or desorbed at time *t*. It must be kept in mind that the JMAK model applies **when growth of a new phase begins randomly in the bulk and at the surface (nucleation is spatially random)**, the sample size is much greater than any individual transformed region, growth proceeds homogeneously throughout the sample, and nucleation rate is constant [88-90].

The parameters describing the reaction kinetics, such as the nucleation and growth rates, are contained within an **effective kinetic parameter**, ***k*****,** while the exponent,η**, called the Avrami exponent or reaction order**, provides some **information about the dimensionality of the transformation**, i.e., whether it is one, two-or three-dimensional and whether it is interface-limited or diffusion-limited. Eq. (3.10) can be rearranged to the following linear equation

$$\ln[-\ln(1-\alpha)] = (\eta \ln k) + \eta \ln t \tag{3.11}$$

from which the values of the reaction order η and subsequently the rate constant **k** can be interpolated **by plotting ln[-ln(1-α)] vs. ln(*t*)**. Such a plot for each constant temperature should give a straight line **with slope** η and **intercept** η**ln(*k*)**. From the latter, **the rate constant *k* can be easily computed knowing the** η **value**. **It must be pointed out that only a nearly linear initial portion of the isothermal kinetic curve** α **vs. time (*t*)** is to be taken into account for calculations. From our experience it is common that **the** η **values can differ depending on temperature for which they are being calculated**. The **different values of** η **suggest** that

different mechanisms are rate controlling of absorption/desorption **at various temperature ranges**. Therefore, **we recommend the usage of free *η* values obtained from a double-logarithm fitting procedure as more “true” than the fixed *η* values** [91].

The apparent activation energy for the absorption/desorption process is usually evaluated from the Arrhenius plot of rate constant *k* values with temperature [88] **by simply plotting a straight line lnk vs. 1/RT (or 1000/RT).**

$$k = k_0\exp(-E_a/RT) \qquad (3.12)$$

where ***E_a* is the apparent activation energy**, *R* is the gas constant (8.314472 J/mol·K) and *T* is the absolute temperature in K. A typical isothermal kinetic desorption curve for the MgH_2 hydride and the corresponding Arrhenius plot for E_A are shown in Fig. 3.10a and b, respectively.

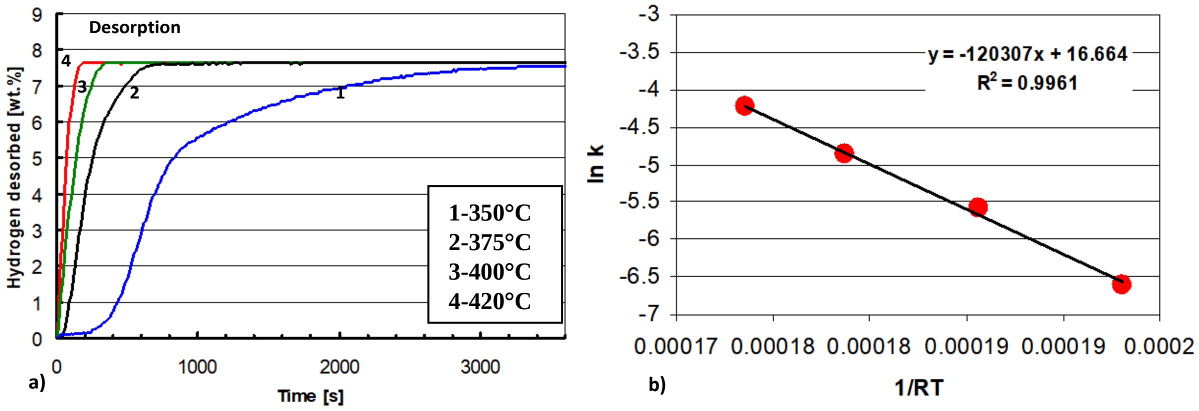

Fig. 3.10. (a) Desorption kinetic curves at various temperatures under initial hydrogen pressure of 0.1 MPa (1 bar) of the as received, non-activated, commercial MgH_2 powder Tego Magnan and (b) the Arrhenius plot of the desorption rate for the estimate of the apparent activation energy, EA, using kinetics data for four temperatures: 350, 375, 400 and 420°C (**E_a=120 kJ/mol**). Coefficient of fit R^2=0.996 [10].

The most popular and universal model describing absorption and desorption process in hydrides seems to be the JMAK and we will focus on calculation of energy of activation using this approach. However, it must be noticed that in same particular cases other mechanisms of hydride formation and decomposition can be applied. There are **a few other kinetics models** listed in Table 3.2. For example, Barkhordarian et al. [92, 93] and Liang et al. [94] have applied **contracting volume model** for the kinetic analysis of sorption process in MgH_2 catalyzed by Nb_2O_5 and V, respectively. Nevertheless, in similar composites (Mg+Nb, MgH_2+V) [88, 95] the kinetic of sorption was analyzed using JMAK. **We tested the three respective models from**

Table 3.2: **JMAK**, **contracting volume** $1-[1-\alpha]^{1/2}=kt$ (**two dimensional growth with constant interface velocity**) and **surface reaction** $\alpha=kt$, **for MgH_2 hydride doped with 5 wt.% of micrometric Ni catalyst** [**10**]. The results of these calculations are presented in Fig. 3.11 and 3.12. The obtained activation energy values equal 105, 101 and 105 kJ/mol, respectively. **This shows that in practical situation each of these three models gives almost identical activation energy**.

Table 3.2. Kinetic equations used for fitting experimental hydrogen sorption data [**10**].

Model equation	**Description**	**Ref.**
$\alpha = kt$	Surface controlled (chemisorption)	[**90**, **92**]
$[-\ln(1-\alpha)]^{1/\eta} = kt$	Johnson-Mehl-Avrami-Kolmogorov (JMAK): $\eta = 3$ - three-dimensional growth of existing nuclei with constant interface velocity $\eta = 2$ - two-dimensional growth of existing nuclei with constant interface velocity	[**92, 93**]
$1-(1-\alpha)^{1/\eta} = kt$	Contracting volume (CV): $\eta = 3$ - three-dimensional growth with constant interface velocity $\eta = 2$ - two-dimensional growth with constant interface velocity	[**92, 93**]
$1-(2\alpha/3)-(1-\alpha)^{2/3} = kt$	contracting volume (CV): three-dimensional growth diffusion controlled with decreasing interface velocity	[**92, 93**]

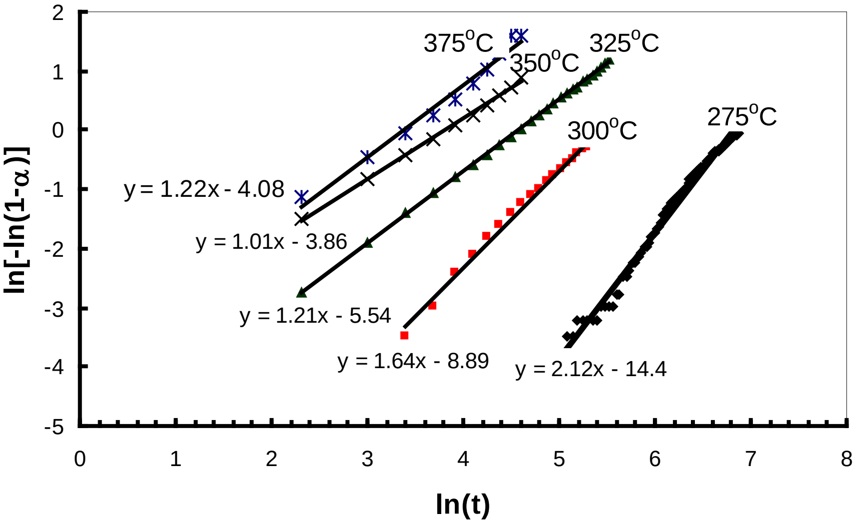

Fig. 3.11. Plot ln(-ln(1-α)) vs ln(t) for dehydrogenation of MgH_2 (Tego Magnan®) milled for 20 h and catalyzed by 5wt.%Ni (tests were done in temperature range 275÷375°C using non-activated powder) [10].

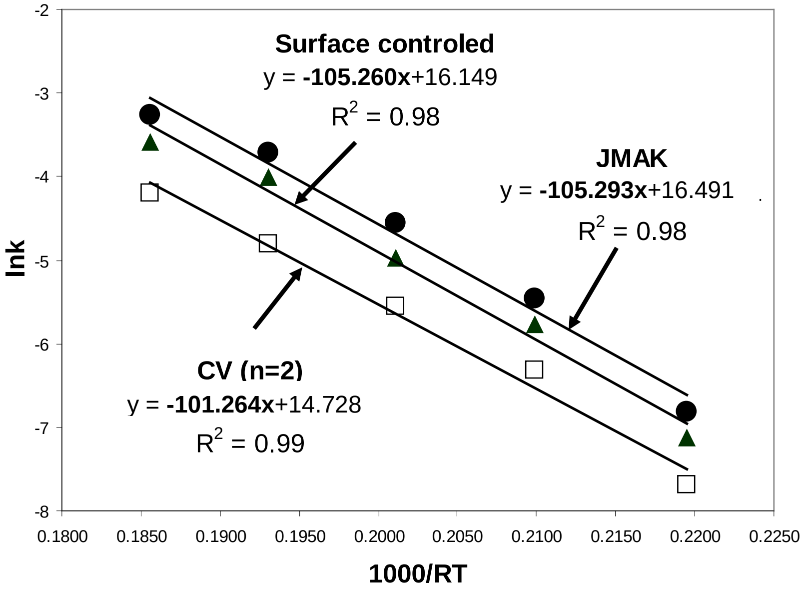

Fig. 3.12. Arrhenius plots for dehydrogenation of MgH_2 (Tego Magnan®) milled for 20 h and catalyzed by 5 wt.%Ni (tests were done in the temperature range 275÷375°C using a non-activated powder). Arrhenius plots were obtained using various models of decomposition process (Table 3.2) [10].

3.4. PCT and kinetic curves determination by volumetric method in a Sieverts-type apparatus

The hydrogen desorption or absorption PCT curves of various hydrides can be evaluated using a Sieverts-type apparatus. The scheme of typical Sieverts-type apparatus is shown in Fig. 3.13.

The Sieverts-type apparatus consist of: a calibrated volume determined physically, a reactor whose temperature is controlled by the temperature control system and the cooling system, a vacuum system, a pressure monitoring system, valves and source of hydrogen and argon delivery. The quantity of desorbed hydrogen (number of moles) is calculated using ideal gas law:

$$PV = nRT \qquad (3.13)$$

where ***P***–gas pressure, ***V***–gas volume, ***n***–number of moles of gas, ***T***–absolute temperature of gas, ***R***–the universal gas constant. The value and units of ***R*** depend on the units used in determining ***P***, ***V***, ***n*** and ***T***

- The quantity of gas, ***n***, is normally expressed in ***moles***
- The units chosen for pressure and volume are typically *atmospheres* (***atm***) and *liters* (***L***), however, other units may be chosen

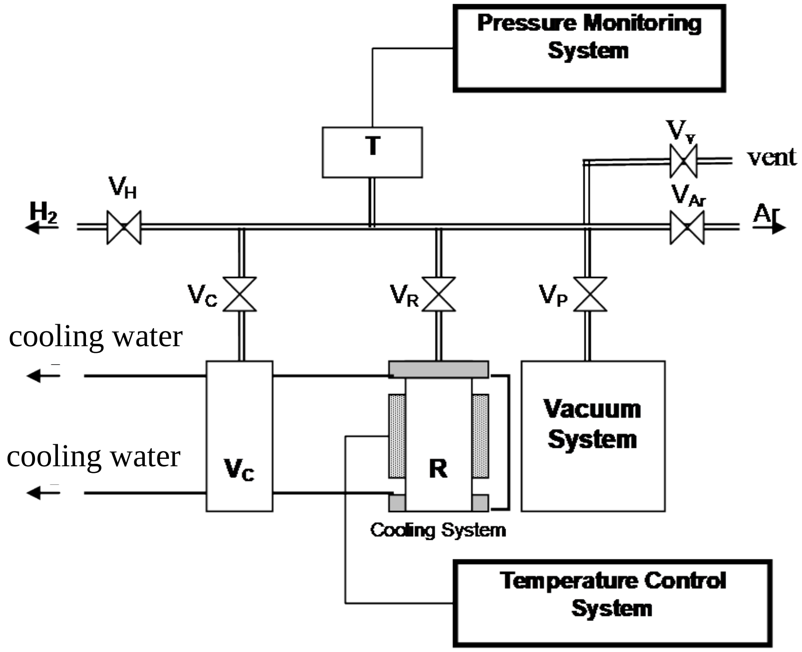

Fig. 3.13. Scheme of Sieverts-type apparatus where: T- transducer for pressure, V_H – hydrogen cut off valve, V_{Ar} – argon cut off valve, V_P – vacuum system cut off valve, V_R – reactor cut off valve, V_C – calibrated volume and its cut off valve, V_v - vent valve, R – reactor [10].

Therefore, ***R*** can be expressed for example in **L·atm/mol·K** where ***R***=0.08206. For thermodynamic calculation the universal gas constant includes energy unit ***R***= 8.314472 J/mol·K. Let us assume that we can treat hydrogen as an ideal gas. Before beginning of absorption or desorption the relation between pressure of hydrogen in a system and number of moles of hydrogen at temperature T of the analyzed process can by described by:

$$P_1V = n_1RT \tag{3.14}$$

After desorption or absorption we have:

$$P_2V = n_2RT \tag{3.15}$$

where $P_1 > P_2$ for absorption and $P_1 < P_2$ for desorption

Rearranging (3.14) and (3.15) we obtain:

$$n_1 = \frac{P_1V}{RT} \qquad n_2 = \frac{P_2V}{RT} \tag{3.16}$$

Therefore, the difference between number of moles of hydrogen in the system resulting from absorption or desorption is:

$$\Delta n = n_1 - n_2 = \Delta P \frac{V}{RT} \tag{3.17}$$

where $\Delta P = P_1 - P_2$.

The mass of absorbed or desorbed hydrogen can be calculated using number of moles of gas and molecular mass of hydrogen: $\boldsymbol{m_H = 2.016 \cdot \Delta n}$ which finally gives us:

$$m_H = 2.016\Delta P \frac{V}{RT} \tag{3.18}$$

When change in hydrogen mass is known we can easily calculate hydrogen capacity (wt.% H_2) in the investigated material using Eq. (3.7).

The ideal gas law should be corrected by the Van der Waals equation for the volume of gas molecules and molecular interactions **at high hydrogen gas pressures**.

$$\left(p+\frac{n^2a}{V^2}\right)(V-nb)=nRT \tag{3.19}$$

where ***a* is the measure of attraction between hydrogen particles** (0.2476 L^2bar/mol^2) and *b* is the volume excluded by a mole of hydrogen particles (0.02661 L/mol). **From our tests it seems that (3.19) should be used for pressures higher than about 5 MPa**.

From the scheme of Sieverts apparatus presented in Fig. 3.13 we can see that volume which must be taken into account during calculation of quantity of desorbed or absorbed hydrogen does not consist of only a reactor volume. **The volume *V* in (3.18) in a real system is made up of volume of reactor plus internal volume of connecting pipes, valves and as well as the transducer**. The direct measurement of these parameters is impossible. Moreover, the transducer **measures pressure changes in this part of apparatus where temperature is ambient, so for calculation using (3.18) we apply T=297 K (ambient temperature 24°C)**. Nevertheless, **increasing the reactor temperature to the process temperature of process (usually in the range from 40÷400°C), increases the temperature of hydrogen gas in the entire system**. That is why an application of the ideal gas law would not be possible. Therefore, to evaluate the volume of gas that participates in sorption process, the system volume calibration process is necessary.

Calibration process consists of a few steps. At first we have to obtain advisable pressure P_1 (usually about 10 atm) of argon in a calibrated volume V_C and atmospheric pressure in the rest of the system (reactor and connections). Then by opening calibrated volume cut off valve V_C and by pressure reduction to the value P_2 the total volume of the system for the apparatus with the relative transducer can be calculated using formula:

$$P_1V_c=P_2\left(V_c+V_s\right) \tag{3.20}$$

where **V_s is made up of volume of reactor plus internal volume of connecting pipes, valves and as well as the transducer**. Rearranging (3.20) we obtain

$$V_s = \frac{(P_1 - P_2)}{P_2} V_c \qquad (3.21)$$

To eliminate the temperature effect, the calibration curve must be obtained by repeating described process within the temperature range RT-T_{max}, where RT-room temperature and T_{max}–maximum temperature of process).

To determine PCT curve by volumetric method at first we have to know mass of analyzed powder (hydride or pure metal). The typical mass of powder used in volumetric method is in a range 50-500 mg and depends on V_R (reactor volume with volume of connecting pipes, valves and transducer). After the mass measuring, the powder is loaded in to specimen holder and then it is placed in the Sieverts apparatus reactor. **To prevent any oxidation and for safety reason system must be purged a few times by argon and then evacuated. However, one must be careful how much powder is appropriate for the absorption/desorption volume of a Sieverts-type apparatus.**

Fig. 3.14 shows the desorption experiments from two different masses of MgH_2 doped with nano-Ni (n-Ni) powder. It is seen that the mass of 140 mg gives about 3.0 wt.% of desorbed hydrogen while the smaller mass of powder (50 mg) let more hydrogen to be desorbed.

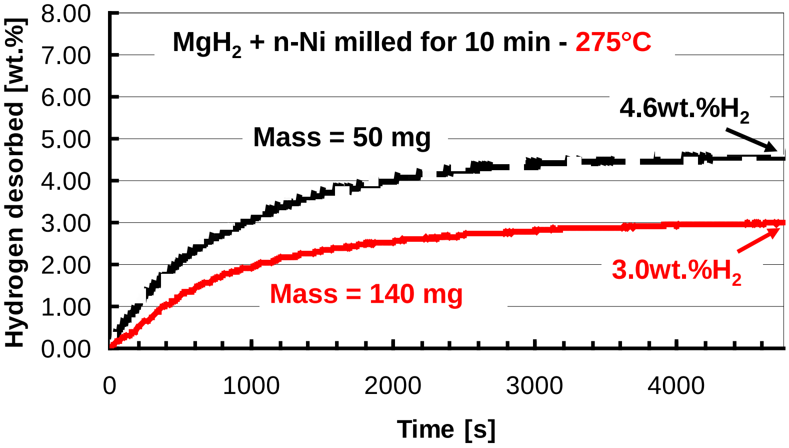

Fig. 3.14. The effect of the mass of desorbing hydride powder on the amount of hydrogen desorbed at 275°C at 0.1 MPa from MgH_2 doped with 5 wt.% of nano-nickel (n-Ni)[10].

This behavior can be explained if we resort to the imaginary desorption PCT curve at 275° in Fig. 3.15. **The equilibrium plateau pressure at 275°C** is **higher** than **0.1 MPa (1 bar=1 atm) at**

which desorption is carried out and at this temperature MgH$_2$ can desorb. However, the kinetics of desorption will depend on the driving force (as shown in Fig. 3.1). **Since a larger mass of hydride will produce a higher overpressure, much above 0.1 MPa, in a confined desorption volume of a Sieverts apparatus, which is closer to the plateau at 275°C, then kinetics could be slower and as a result a smaller amount of hydrogen could be desorbed as opposed to a small amount of hydride that creates lower overpressure and higher driving force allowing more complete desorption.**

When we want to obtain **a PCT curve for decomposition process the pressure of hydrogen must be set up above the expected equilibrium pressure to prevent decomposition during heating to this temperature.** If **we do not have any information about equilibrium pressure for investigated material we should apply maximum pressure which is allowable by our Sieverts apparatus. High hydrogen pressure should prevent decomposition of hydride during heating up to the temperature of the test.** When temperature of the test is reached and system is thermally stable we can start gradually decreasing the pressure and registering amount of released hydrogen related to the equilibrated pressure.

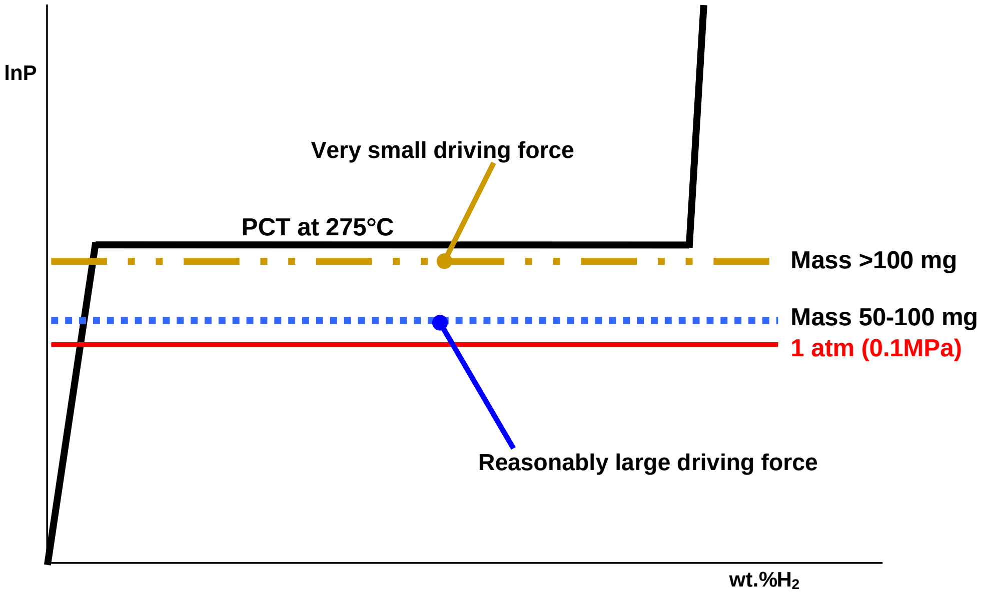

Fig. 3.15. Schematic plot showing the effect of a mass of MgH$_2$ hydride on the driving force for desorption at 275°C at atmospheric pressure [10].

In a case of **the PCT absorption curve** after evacuation, the system must be heated up to a test temperature and **thermally stabilized**. **Then by gradually increasing pressure we will observe hydrogen absorption related to a particular pressure of hydrogen. It is important that time of visible pressure change at every step is closely connected with the kinetics of process at an applied temperature.**

An analysis of absorption and desorption kinetics is very similar to the PCT curve determination. **Before starting the desorption test, the inner tubing of the apparatus is also evacuated and purged a few times with argon and then two times with hydrogen.** Subsequently, **hydrogen at a high pressure preventing desorption is admitted into the airtight desorption chamber containing the hydride powder and the temperature of the chamber is gradually increased up to the desired desorption temperature.** The high pressure barrier should be applied to prevent any desorption during the period of temperature stabilization within the desorption chamber. Once the **temperature is stabilized** the hydrogen pressure is quickly reduced to 0.1 MPa (1 atm or 1 bar) and the hydrogen desorption process begins (pressure increases above initial 0.1 MPa). No elaborate activation procedure usually is applied to the powders. **Absorption test** starts with purging process as well as evacuation and then system is thermally stabilized under vacuum. Subsequently, hydrogen at desired absorption pressure is admitted into the system and by observing the pressure decreasing as a function of time, the kinetic curve is registered. T**he difference in pressure between the initial pressure and that at the instant of time is taken for calculation of the mass of absorbed/desorbed hydrogen from (3.18) and (wt.%) of absorbed/desorbed hydrogen (capacity) from (3.7).**

To be absolutely sure that thermal stabilization of measuring system under high preventing pressure of hydrogen does not affect hydrogenation/dehydrogenation properties of analyzed hydride, **we studied some properties, important from a decomposition point of view, for powder before and after annealing process**. **MgH_2 ball milled for 100 h** was heated up to various temperatures (300, 325 and 350°C) under preventing 4.5 MPa pressure of hydrogen in a Sieverts apparatus exactly in this same manner as during thermal stabilization. To eliminate any doubts **the annealing time was increased up to 45 minutes**. After annealing, the powder was cooled down up to ambient temperature and investigated by DSC and XRD analysis. Figure 3.16 shows the influence of annealing temperature during thermal system stabilization on DSC test results.

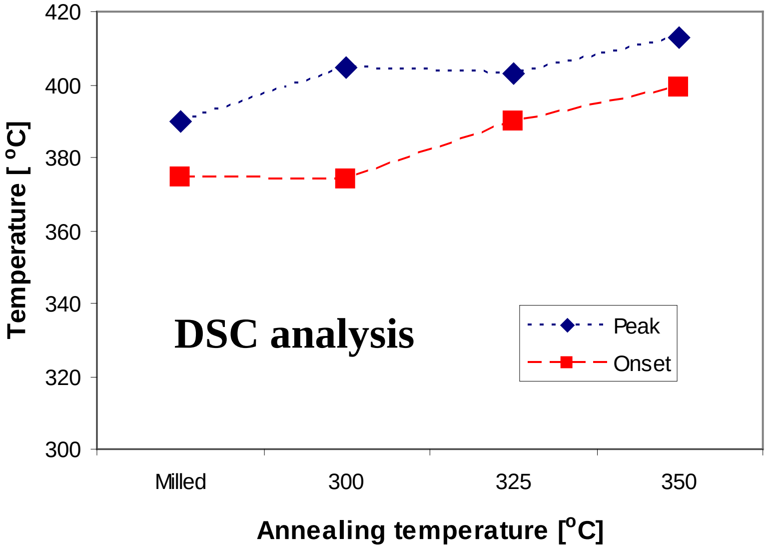

Fig. 3.16. The influence of annealing temperature on onset and peak temperature of decomposition peak obtained by DSC test for MgH_2 [**10**].

A slight increase of both onset and peak temperature is observed which means that tendency to the decomposition of annealed powder is even less than that for the powder directly after milling. The structural analysis by XRD method (will be discussed later) in Table 3.3 and Fig. 3.17 shows **progressive decrease of the amount of γ-MgH_2 in powder after annealing as compared to phase composition in a powder directly after milling**. Moreover, **slight increase of crystallite (grain) size of β-MgH_2 during thermal stabilization of a Sieverts apparatus is observed**. However, **the crystallite (grain) size of magnesium hydride is still in the nano range (35 nm for powder annealed up to 350°C)**. These observations clearly prove that **the thermal stabilization of Sieverts apparatus under high pressure of hydrogen carried out under previously specified conditions cannot be treated as an activation process and it causes**

negligible structural changes in the investigated hydride (true for MgH_2 but for other hydrides?).

Table 3.3. Phase composition and grain size of β and γ-MgH_2 after milling and annealing in Sieverts apparatus during thermal stabilization of the measuring system, at 300, 325 and 350°C under high pressure of hydrogen (4.5 MPa) [10].

Sample	Grain size of β-MgH_2 [nm]	Grain size of γ-MgH_2 [nm]	Phases present in powder
milled	13±2	13±0.1	β-MgH_2, γ-MgH_2, MgO
Annealed 300°C	19±1	19.±0.3	β-MgH_2, γ-MgH_2, MgO
Annealed 325°C	28±1	29±2	β-MgH_2, γ-MgH_2, MgO
Annealed 350°C	30±2	---	β-MgH_2, MgO

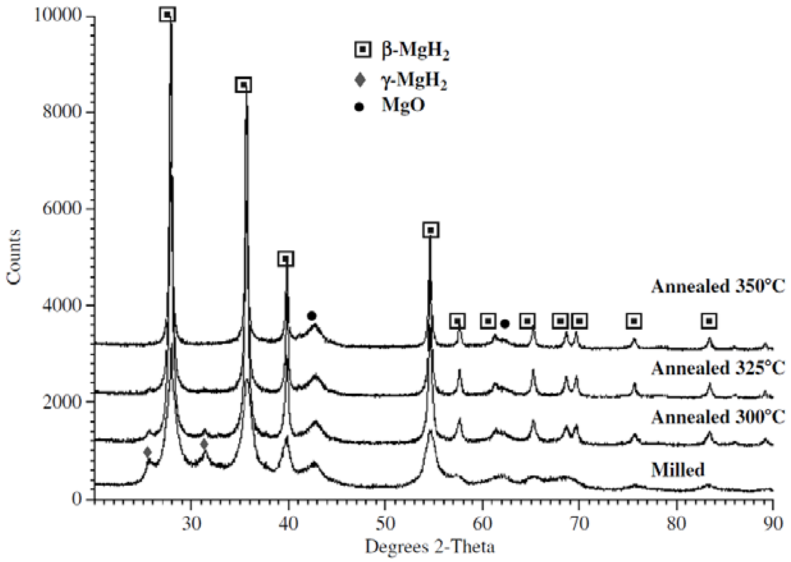

Fig. 3.17. XRD pattern of MgH_2 hydride after milling and annealing in Sieverts apparatus during thermal stabilization of the measuring system for 45min at 300, 325 and 350°C under high pressure of hydrogen (4.5 MPa) [10].

Alternatively, in my laboratory at the University of Waterloo, we technically modified our original Sieverts unit (Fig. 3.18) such that it allowed **loading a powder sample into a separate small stainless steel reactor in a glove box under high purity argon, which was then sealed with a cap and subsequently transferred to the main unit without any exposure to the environment.** Then before starting the desorption test, the inner tubing of the apparatus was evacuated and purged four times with ultra-high purity hydrogen and the small reactor was pressurized to 1 bar H_2. We used samples with a nearly constant masses of 30–40 mg for a desorption test. The **furnace of the apparatus was heated separately to the desired test temperature** and **subsequently inserted onto a tightly sealed powder sample reactor.** It was measured experimentally that the powder sample in the reactor usually reached **the furnace temperature within 100-400 s** in the temperature range of 100–200°C which was negligible compared to desorption completion time. Hence, the test can be considered as **“pseudo-isothermal”**.

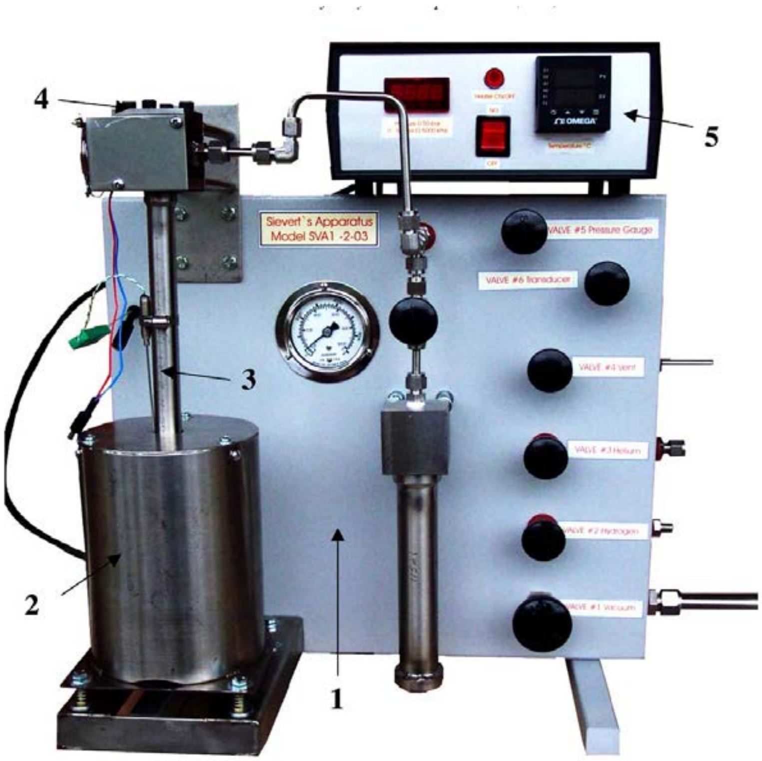

Fig. 3.18. A Sieverts-type apparatus custom-built by A.O.C. Scientific Engineering Pty Ltd., Australia, for evaluating hydrogen storage properties. (1) Gas pressure unit up to 5000 kPa; (2) furnace up to ~500°C; (3) tubular specimen chamber; (4) specimen chamber lid; (5) electronic control unit (pressure transducer &thermocouple) [96].

Finally, a small but important technical detail related to the method of measuring pressure by a transducer attached to a Sieverts apparatus (T in Fig. 3.13) may be in place here. **Some transducers measure pressure relative to the atmospheric and display a zero value when pressure equals atmospheric.** In this case, during constructing PCT curve a 1 atm should be always added to each pressure reading from the transducer’s display. If a Sieverts’ system is

equipped with a transducer measuring and displaying the value of 1 atm at an atmospheric pressure, this correction is redundant. **Also, this correction is redundant during measuring hydrogen absorption/desorption kinetic curve because in this case what is needed for calculation of the hydrogen quantity is just ΔP in (3.18).**

4. NANOSTRUCTURED HYDRIDES [10]

An important question arises **why nanostructured hydrides?**

The first and the most important alloy, for which the H_2 storage properties clearly benefited from nanostructuring, was Mg_2Ni, an A_2B –type intermetallic. While yet in 1961 Dymova et al. [65] pointed to the small grain size as a primary factor in improving hydrogen sorption in Mg, and other Russians, Ivanov et al. [97] demonstrated the high energy ball milling route to hydrogen storage in magnesium, it took another four decades and series of studies reported from the McGill University in Canada to bring again the benefits of fine-grains to attention of community of researchers in hydrogen storage. The clear demonstration of the effect of nanostructuring came in works of Zaluskis' [98] for Mg_2Ni. A study of ball milled powders showed that when the smallest X-ray diffracting metal grains in milled particles reach the range 5-50 nm **the kinetics** of both **absorption and desorption are improved** by an order of magnitude. These were nanostructured hydrides or nanohydrides. It must, however, be pointed out that they completely ignored the **effects of simultaneous decrease of particle size during milling** (will be discussed later).

4.1. Conventional routes for the synthesis of nanostructured materials

Since the interest arouse in unusual chemical, physical and mechanical properties of nanostructured materials, progress in the synthesis of such materials has only been accelerating. Already established **wet chemistry** methods, with use of **aqueous and non-aqueous solutions**, have been re-examined in respect to feasibility to conduct **chemical precipitation** of nanocrystalline phases under conditions that hinder growth of customary crystalline phases. In general, methods have been explored that accelerate the rate of reaction thus limit the time available to ions to diffuse and contribute to growth of the nucleating crystals. Among the advantages of the established wet chemistry methods, like sol-gel processing, **are good control over microstructure and particle morphology, and no needs for special equipment.** Sol-gel approaches were delivering good results even when a synthesis of complex structures was required (e.g. in complex multimetal oxides). Generation of nanometer-sized phases through **deposition of metals and metal oxides from gas phase** were among the **first dry-chemical** methods [99]. Many of new processes required development of special equipment or methods as to conduct physical vapor deposition (PVD) or chemical vapor deposition (CVD) under thermodynamically non-equilibrium conditions. Among these old and new processes for preparation nanocrystalline alloys and compounds are:

- solution- precipitation methods, e.g., these with use of strong borohydrides reductors
- sol-gel technologies
- reverse –micelle synthesis
- polymer-mediated synthesis
- protein-templated methods
- rapid solidification and devitrification of amorphous metals and metallic glasses
- combustion-flame chemical vapor condensation processes (Kear)
- induction –heating chemical vapor condensation processes
- DC and RF –magnetron sputtering, incl. method of thermalization
- laser ablation methods
- supercritical fluid processing
- sonochemical synthesis and microwave hydrodynamic cavitation synthesis

Many if not all of these processes have already been developed and well established even before the term “nanomaterials” was coined; they remain further refined with focus on manufacturing materials for particular properties, electronic, etc. All of them are well covered in books and monographies, which are too many to make good recommendation to our Reader. For recent progress the Reader can consult *Nanomaterials Handbook*, where the editor, Yury Gogotsi, assembled impressive body of authors to write chapters on processing and properties of many nanomaterials, particularly well covered being carbon-based nanomaterials, metallic, semiconductors and ceramic nanomaterials [100]. **All of these methods stem from a natural property of atoms to self-organize into ordered structures and crystallites as being driven by energy benefits when atoms join into structures**. Short-range ordering in metal alloys may be formed during deposition of atoms or atom clusters from gas phases, and survive non-equilibrium processing of metals via solidification from rapidly quenched melts. The short-range order of atoms may even be preserved in amorphous metallic alloys. The approach to build up nanocrystals through such self-organization of atoms is well recognized in preparation of nanomaterials and termed the ***bottom-up nanotechnology approach*****.**

Bottom-up processing of nanomaterials relies upon use of either liquid solvents and vapor gas phases, or solidification from molten metals and compounds. However, **in this lectures we concentrate on nanoprocessing conducted entirely in a solid state.** This is a class of methods based on processes conducted in **high-energy ball mills.** Such methods are based on high-energy grinding and milling of materials. They provide ***top-bottom approach*** towards manufacturing nanomaterials.

4.2. New routes to nano-hydrides: mechanical milling, alloying and mechano-chemical activation

High-energy ball milling is the only ***nanotechnology top-down approach*** for **the synthesis of nanoparticles**. In the process of mechanical milling (MM) brute force is applied to material, whether it is a metal, a pre-alloyed intermetallic, or a solid chemical (stoichiometric) compound: the force which is sufficient to disperse the material into fine nanometric particulates or agglomerates of such. Even short milling times can break thin chemically passive surface coatings (e.g. surface oxides) and **expose fresh, clean chemically-active metallic surface**. Such milling can also introduce **lattice defects** into solid compounds. It results in an increased chemical activity of milled media towards both gasses and chemical reactions in solutions and electrolytes; the process often termed ***mechano-chemical activation synthesis (MCAS)***. Longer milling of intermetallics leads to changes in the long-range order in intermetallics. Such a process termed sometimes ***mechanical disordering*** **(*MD*)** leads to formation of **disordered intermetallic compounds**.

A process when mixture of **elemental metal powders, or powders of metal and non-metal are milled long enough** to trigger alloying of elemental powders in a solid-state process is termed ***mechanical alloying (MA)***. This **non-equilibrium synthesis of new metal alloys by high-energy ball milling of powders was developed almost 40 years earlier** by John Benjamin and his coworkers at the International Nickel Company (INCO) [**101**]. The development came from research on new alloys intended for gas turbines, and was an outcome of an effort to produce nickel superalloys, which were mechanically hardened through an inoculation with fine refractory metal oxides, Al_2O_3, Y_2O_3, and ThO_2, in so-called oxide dispersion–strengthened (ODS) process. In his research Benjamin pointed out that *mechanical alloying (MA)*, a new process induced by intensive milling of metal and compound powders, could make new materials with unique properties [**101**]. (*In a historical note like this, the credit for coining the term "mechanical alloying" must be given to Ewan C. MacQuinn, a Patent Attorney for INCO company*).

Mechanical alloying is conducted through **milling of two elemental metal powders**. Longer milling, order of hours, leads to atomic-level mixing of the metals and produces an alloy consisting of these metals. Until the advent of this new, non-equilibrium and low-temperature solid-state processing method, metal alloys could only be manufactured by melt casting and metal foundry practices.

There is a sequence of consecutive **mechanical events** together with **concurrent events of chemical nature** that leads to the realization of the mechano-chemical process described as mechanical alloying. **Mechanical alloying can be regarded as a repeated stressing, deformation, fracture and cold welding of powder particulates, as illustrated schematically in Fig. 4.1.** These mechanical processes are interlaced with **enhanced diffusion of chemical species and increase in structural disorder**. **The first step is development of high-rate stresses in the milled powders. The key step is repeated high-rate, *severe plastic deformation* followed by series of chemical and mechanical processes which result in generation of structural disorder, extended solid solubility of chemical species, and formation of metastable phases and nanostructures.** The sequence of concurrent mechanical and chemical events can be written as follows:

mechanical stressing → severe plastic deformation→ formation of a submicron lamellar microstructure→ cold interdiffusion of metal atoms between lamellae or nanograins (cold welding) → fracture → formation of nanostructure→ extended solid solubility→ mechanical alloying with formation of thermodynamically stable and/or metastable phases → amorphization (if any).

A great deal of research papers, also review articles, was published on the subject of mechanical alloying. Also, there are serial conferences and international meetings on the subject, where new developments in mechanical alloying for processing of nanomaterials, including those for use in hydrogen storage, are reported. Since this field of materials science is growing rapidly at the time we write this book it would be difficult to select scholarly papers published on this complex subject. Instead, we will refer this reader to an extensive review, which could be of particular help [**102**].

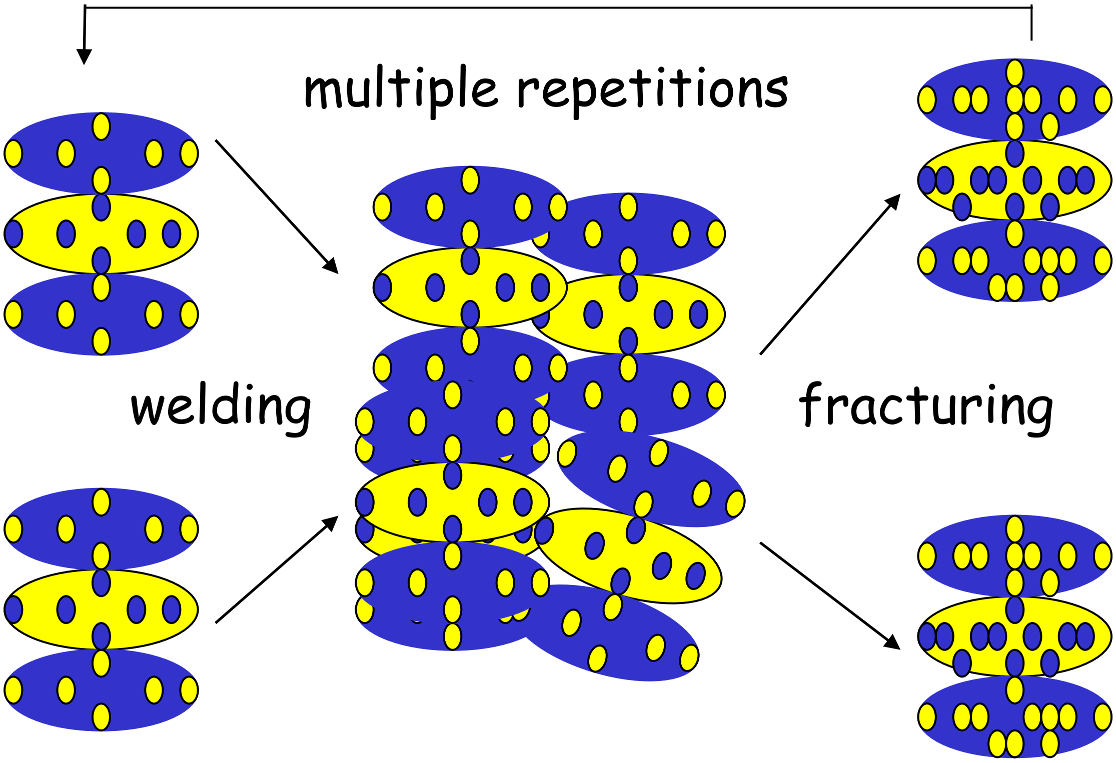

Fig. 4.1. Mechanical alloying through repetitive welding and fracturing. Blue-metal A, Yellow-metal B (particles and atoms) [**10**].

When the milling process initiates a **solid-state reaction and yields a new stoichiometric or quasi-stoichiometric chemical compound**, like carbide, nitride, silicide, etc. such a process can be termed **reactive mechanical alloying or reactive mechanical milling (RMA/RMM)**. **When mechanical modes of milling (shear, impact) are controlled we have *controlled reactive mechanical alloying or controlled reactive mechanical milling (CRMA/CRMM)*.** Reactive mechanical milling can be realized **by reacting a solid compound A in gas B in a solid-state synthesis that yields a distinct chemical compound C**. Reactive milling can be conducted by milling metal powders in ball mills **filled with a reactive gas, like N_2 or H_2.** Milling with hydrogen can also lead to reduction of oxides during milling. Hydrogen can also alloy with metals to form interstitial metal-hydrogen solutions, hydrides or chemical hydrides.

This approach to preparation of new hydrides and hydride nanocomposites has been developed at the University of Waterloo and CANMET's government laboratories in Ottawa, Canada around years 2002-2005. The milling is conducted in a specialty, **magnetic high-energy ball mill**, where **trajectories of balls are well controlled, and H_2 gas can be supplied and absorbed during milling**. The complex Mg_2FeH_6 hydride was prepared in this way by Varin et al. [**103**] in the direct, mechanically-driven synthesis, viz. ***direct mechanosynthesis reaction*** by reacting inexpensive elemental Mg and Fe metals:

$$2Mg + Fe + 3H_2 \longleftrightarrow Mg_2FeH_6 \tag{4.1}$$

The reaction of Eq. (4.1) follows directly reverse path to the thermal decomposition reaction of Eq. (2.10) and **proceeds at room temperature and only slight overpressure of hydrogen supply**. This presented a new **mechanical activation route to manufacturing of nanomaterials for hydrogen storage**.

If a hydride is ball milled with **halides**, e.g. **metal chlorides**, a new type of usually complex hydride could be synthesized. This is termed ***mechanochemical activation synthesis (MCAS)***.

A primary method of mechanochemical synthesis of nanostructured hydrides (nanohydrides) is processing by mechanical (ball) milling. Processes of manufacturing of nanocrystalline/nanostructured hydrides by ball milling are shown in Fig. 4.2.

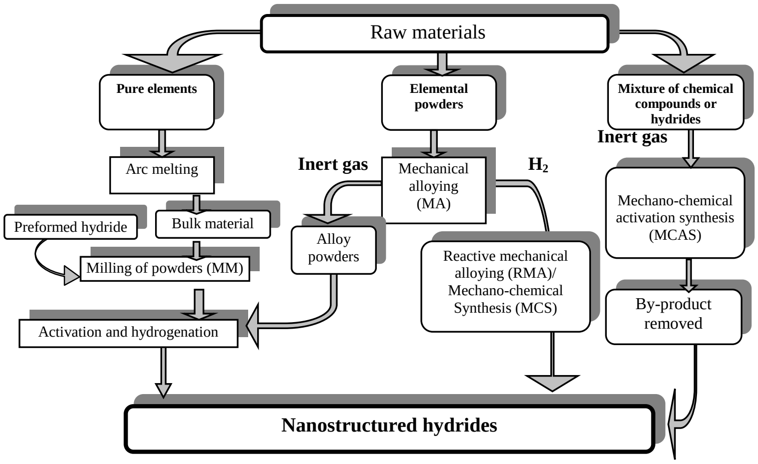

Fig. 4.2. Flow chart showing the possible methods of manufacturing nanocrystalline/nanostructured hydrides. Modified from [**104**].

There are **three major processes all of which start from raw metallic/non-metallic elements** [**104**].

(1) In the first procedure, called a ***two-step method***, either **pre-milled pure metallic elements or a mechanically pulverized pre-cast intermetallic ingot are hydrogenated under gaseous hydrogen** to form a desired metallic or intermetallic-based hydride such as for example MgH_2 or Mg_2NiH_4. For hydrogen alloying of a powder mixture, elemental powders are mixed in desired proportion and then mechanically alloyed (MA) by ball milling under inert gas (e.g. argon) to form intermetallic compounds. The formation of intermetallics in milled metal-metal and metal-metalloid (e.g., B, Si, C) systems is the first step of mechanosynthesis [**105**]. The general reactions for a binary system A and B are as follows:

$$nA + mB \rightarrow A_mB_n \qquad \textit{via}\text{ ingot/powder} \qquad (4.2a)$$

$$A_mB_n + (x/2)H_2 \rightarrow A_mB_nH_x \qquad \text{hydrogenation} \qquad (4.2b)$$

(2) In the ***one-step method***, ***reactive mechanical milling*** (***RMM***), **elemental metallic powders are milled under hydrogen atmosphere**. The reactions are a direct alloying of metals with hydrogen, i.e. hydrogen alloying (Eq. 4.2b). When sufficient amount of the hydrogen reactant is supplied this reaction yields hydrides with well-defined stoichiometry:

$$A^0 + (x/2)H_2^0 \rightarrow A^{x+}H_x^{-1} \qquad (4.3)$$

As seen from the change in valence of metal and hydrogen this is a *redox* reaction because the metal is oxidized (loses n electrons) by the hydrogen, while the valence of hydrogen becomes, formally, -1. Magnesium dihydride, MgH_2, can be manufactured in ball mills in such a manner, with a reasonable reaction yield. The reaction of Eq. (4.3) is accompanied by both the particle- and the grain-reduction, as will be shown later.

In a variant of the second method described above the **pre-mixed metallic powders (or pulverized ingots) are milled under hydrogen atmosphere to directly form an intermetallic hydride.** It can be also viewed as **hydrogen alloying of metal powders and powder mixtures in hydrogen alloying mills**. This method is called a ***reactive mechanical alloying*** (***RMA***) **or *mechano-chemical synthesis*** (***MCS***).

$$nA + mB + (x/2)H_2 \rightarrow A_mB_nH_x \qquad (4.4)$$

MCAS –type reactions can occur while milling a simple metal hydride with a metallic element M,

$$2AH+2Al+3H_2 \rightarrow 2\ AAlH_4 \qquad (4.5a)$$

for instance NaH with Al [106]:

$$NaH+Al+3/2H_2 \rightarrow NaAlH_4 \qquad (4.5b)$$

Mechanosynthesis reaction can also be conducted with use of **a second hydride, instead of hydrogen gas** reactant. Most often the first hydride is a simple metal hydride, while the second hydride is a complex hydride.

$$2NaH+ NaAlH_4 \rightarrow Na_3AlH_6 \qquad (4.6)$$

Such reactions have been observed to occur where an alanate like $NaAlH_4$ is milled with alkali metal hydride, like NaH or LiH.

(3) In the third method called ***mechano-chemical activation synthesis*** (***MCAS***), **a mixture of metal compound, viz. metal halide (e.g. chloride, fluoride) is ball-milled with a hydride** to induce a reaction to yield a high-hydrogen capacity hydride.

If an n-valent metal chloride or fluoride (AX_n) is used in the reaction with alkaline metal borohydride $B(BH_4)$ then in general terms the reaction can be written as

$$AX_n+nB(BH_4) \rightarrow A(BH_4)_n +nBX \qquad (4.7)$$

where $A(BH4)_n$ is a newly synthesized complex metal borohydride and BX is a salt (X=Cl or F). Either Li or Na borohydrides, like $LiBH_4$ or $NaBH_4$, are used as source of hydride complex. Similar reactions are used for preparation of alumohydrides, viz. alanates, using Li or Na alanates, $LiAlH_4$ or $NaAlH_4$. **These reactions are mutual substitution reactions where the ions in two compounds change sites in the crystalline lattice**. The valence of the metals and the hydrogen do not change from the reactants to the products. This is analogous to well-known **metathesis reaction**, which is a common method for **preparation borohydrides in donor non-aqueous wet solvents (tetrahydrofuran (THF) and ethers)**. **The MCAS advantage is that solid-state process does not require use of an organic solvent (tetrahydrofuran (THF) or ethers)**, **whereby the borohydride does not come with the organic solvent molecules bonded in its crystalline lattice**. Said this, we must observe that the MCAS process yields a mixture with alkali metal chloride or fluoride (**salts**), and **to purify the complex hydride product from the salts, one must call upon a difference in solubility between the borohydride and the metal chloride (salt) in the same THF or ether solvents.** There are also disadvantages that can be mentioned when opting for preparation borohydrides or alanates by solid-state mechanosynthesis. Certain hydride complexes are not stable, and become stable only when borohydride or alanate molecule is solvated. Also, certain structures based on hydride complexes may be not stable under mechanical ball milling. The mixture of Mg and B milled with hydrogen yields an amorphous phase, instead of the anticipated $Mg(BH_4)_2$, with release of hydrogen gas [**107**].

4.3. Milling processes and equipment

The milling, grinding and pulverizing of materials has always been one of unit operations in chemical engineering. They are well described in chemical engineering handbooks along with heat transfer, mass transfer, fluid flow, and thermodynamic processes. Each of these unit operations gather knowledge of physical laws and practice that is necessary for reliable engineering design in many industries, viz. mineral, ceramic, and powder metallurgy. The **primary objectives of milling have always been mixing or blending, change in particle shape (morphology), and first of all: size reduction**. **The use of the milling and pulverizing for causing the change in fundamental mechanical, chemical and physical properties of the materials itself was not the target of milling or grinding. Use of mechanical milling for synthesis of new alloys, compounds and nanomaterials was not envisioned until recent decades.**

Equipment used for milling may be classified according to the way in which mechanical forces are applied: (i) **between two solid surfaces (crushing, shearing),** and (ii) **at one solid surface (impact)**. **The milling in ball mills combines both crushing/shearing and impact forces combined in various proportions, depending on the equipment used.** There are many different designs of ball mills, which can be used for processing of advanced materials. Among them are:

- Tumbler, jar, dram or cannon ball mills
- Szegvari attritor vertical mills and other vertical stirred ball mills
- Planetary Fritsch and Retsch model mills
- Shaker (vibratory) SPEX model mills
- A.O.C. magnet controlled mechanical model mill (Uni-Ball magneto-mill)
- A.O.C. electric discharge assisted mechanical mill
- ZOZ continuous-fed horizontal mill, and other horizontal high-energy bead mills

Ball or tube mills have **a cylindrical or conical shell, rotating on a horizontal, vertical axis.** The **ball mill** differs from the tube mill by **being short, and having the milling vial length and diameter almost identical.** The typical ball mill, used as much in laboratory like in industry, has been the **tumbler ball mill** (in laboratory practice also known as the jar mill and in industry drum mill). The grinding balls (usually in large numbers) impact upon the powder charge when cylindrical container placed on rollers rotates along horizontal axis. **The balls may roll down the inside wall surface, which produces shear forces on powder trapped between the wall and the ball, but mostly they fall freely accelerated only by gravitation force, then impacting the powders (and other balls) beneath them**. To **maximize the impact** forces imposed on powder the criterion of critical speed may be applied, where N_c expressed in rotations per minute (RPM), is the theoretical speed. N_c, at which the centrifugal force on a ball (at the height of its orbital path) becomes equal the force on it due to gravity [**108**]:

$$N_c\,[\mathrm{RPM}] = 42.3\,/D^{½} \qquad (4.8)$$

where **D is diameter of the mill in meters**, and the **ball diameter is kept small** with respect to the mill diameter.

The milling in ball mills can be described as kinetic processing when the contact of the balls with the material is the main event of **kinetic energy transfer from the grinding media into the powder**. Well-known fundamental equation describe the relation between the kinetic energy - E_{kin}, and the mass- m and the velocity -v

$$E_{kin} = (1/2)\,mv^2 \qquad (4.9)$$

The velocity-v of ball in free fall is g·t, where g is the Earth gravitational (downward) acceleration of the ball, equal to 9.8 m/s^2, and t is the time to cover a distance from the height of its path on the shell to the impacted powder at the bottom of the shell. Hence

$$E_{kin} = (1/2)\,m\,(g\,t)^2\ \ [\mathrm{kg\ m^2/s^2}]\ \text{or}\ 48.02\ m\,t^2\ [\mathrm{Nm}] \qquad (4.10)$$

where the N in brackets represent force units in Newtons. Since the time-of-flight of a ball in free downward direction is greatly limited by diameter-D of the shell, and the energy scales as square root of time, **the kinetic energy, which can be achieved in a simple jar ball mill, is greatly limited. The contact, on impact, between the grinding (balls) and grinded (powder) media is also limited.** Therefore, **laboratory jar and industrial drum (tumbler) mills are *low-energy mills*.**

From the equations above it becomes clear that **the maximum velocity of balls relative to milled material is the primary factor in determining the energy transferred to or deposited in the material.** Larger acceleration than gravitational, hence higher velocity and higher kinetic energy of balls can be achieved in **Szegvari *attritor mills*** (Fig. 4.3). In such mills the milling is conducted in a cylinder filled with balls that are stirred by rotating a horizontal shaft (agitator). The impact of shaft causes differential velocities between the balls, and the powder. This can be seen in Fig. 4.3. The collective impact of a group of balls, and the impact on powder particulates trapped between a ball and the wall, are suppressed.

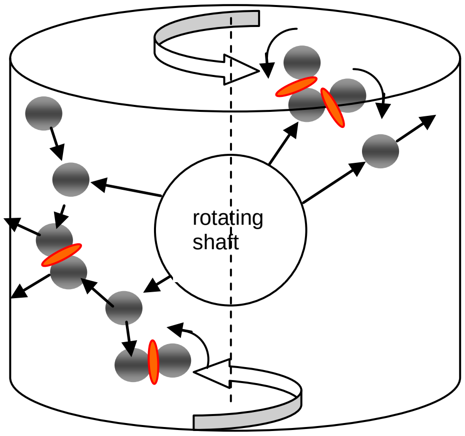

Fig 4.3. Motions of balls in attritor mills; the dotted vertical line represents the axis of rotation of a vertical shaft on which a number of horizontal shafts (arms) are mounted, which strike balls and agitate their motion in very energetic manner; powder particles trapped between the balls (red) are subjected to high-rate deformation processes [**10**].

Attritor mills are vertical mills but the same mechanical milling principle is extended to variety of other vertical mills generically referred to as ***stirred ball mills***. **There are also horizontal stirred mills.** In the latter the shell is stationary and filled with multitude of small balls or beads (dia. 0.6 cm; 1/4” or smaller); hence they are also known as *bead mills*. Stirred-type bead mills stir the milled media at speeds from 100-1500 RPM. These mills are available commercially in batch, continuous and circulation types. The **shear mechanical milling is predominant mode** [**109**] in these mills as the energy of accelerated balls is dispersed among the other balls in the mill (see Fig. 4.3) whose relative motion exerts mostly shearing forces on trapped powder particulates. An **attritor-type ball mill delivers 10 times more energy than comparable size drum ball mill** and some its models can be considered as ***medium energy ball mills***. Although, the efficiency of vertical attritor mills can be low (when the volume available for powder is small and the reactor cylinder is full with balls; and when the powder has tendency to fall by gravity to the bottom of the cylinder) the new horizontal *bead mill* attritors are quite efficient in preparation fine–grained materials.

In ***planetary ball mills*** the force acting on balls is increased. **Centrifugal force of fifty times gravitational force - m•g can easily be produced**. The motion of the shell and the balls in a planetary mill is shown in the schematic Fig. 4.4a. The size of a planetary ball mill will be smaller than the size of a drum (tumbler) ball mill of the same energy. Like attritor and horizontal ball mills they can be considered as ***medium- to high- energy ball mills***, however, milling times needed to process submicron size and nanostructured powders may be long. The commercially available, and popular in research laboratories, particularly in Europe are **Fritsch Pulverisette™ planetary mills**. The models where two or four batches of powders can be processed in the cylinders mounted on rotating plate were the workhorse instruments in many laboratories. The recent Pulverisette Model 7 was designed with larger rotational speeds specially for processing of powders to nanometric-level size. The Fritsch model Pulverisette™ mills, models 4, 5 and 6, are compatible with an interesting reactor cylinder, in which the cover is equipped with pressure and

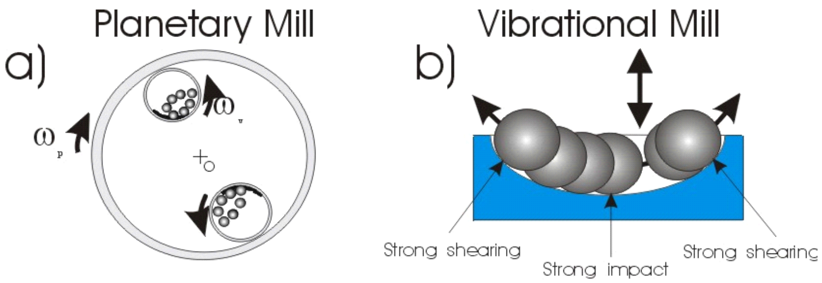

Fig. 4.4 (a) Motion of balls in a planetary and (b) a vibrational mill [10].

temperature sensor and a small radio-frequency unit allows for wireless transfer the sensors data to the receiver interfaced with computer. This GTP (temperature-pressure) system developed by the Fraunhofer Institute in Dresden, Germany, allows for monitoring temperature and pressure of gasses evolved (or absorbed) in the reactor vial in in-situ and real–time conditions. This vial is shown in Fig. 4.5.

Fig. 4.5. A planetary mill vial with the antenna mounted on cover equipped with temperature and pressure sensors for GTP wireless monitoring gas conditions during milling [10].

Since the energy transferred to the material under processing in solid state increases with the frequency of impacting as square of the ball velocity **the most energetic ball mills are such that the balls are “shot” at high speeds and at high frequencies**. This takes place in the ***vibratory ball mills*.** In those mills, known also as ***shaker mills***, an **eccentric motion** is imparted to the cylindrical container (or rather armature on which it is mounted) at frequencies ranging from several impacts per minute, viz. several hertz, up to 1800 hertz, and at small amplitudes of vibrations. The balls oscillate in three mutually perpendicular, or more, planes within a small vial (several tens cm^3) as illustrated in Fig. 4.4b. At average frequency 1200 and the amplitude of ball vibration ca. 5 cm (diameter of the rotating vial) the balls achieve velocities ca. 5 m/s at the moment of impact. The kinetic energy transferred to the material can be very high, even with one 5-gram ball, as one can realize substituting the square of this velocity to Eq. (4.9).

Most of energy transfer in vibratory mills is conducted in the **mechanical impact mode** although **substantial shear of powder particulates is also present**, as the balls rotate on the shell and the particulates are trapped between the shell and the balls. Maurice and Courtney [110] have calculated that **the shock pressure impacts imparted on the powder in the high-energy SPEX model vibrational mill are typically 40 kbars with stainless steel balls of 6 mm in diameter vibrating in a vial 50 mm of diameter**. The SPEX model mill has been used extensively in research laboratories to process small batches of nanomaterials (*ca.* 10 cm^3 or 5 grams). Although this mill has been developed for grinding hard materials, like $ZrSiO_4$, TiO_2, SiO_2, Al_2O_3, in analytical spectroscopy laboratories, this has been the mill that brought the solid nanoprocessing and mechanical alloying research to laboratories worldwide, and particularly in North America. Fig. 4.6 shows the SPEX Model 8000 Duo high-energy mill for simultaneous milling two powder batches, as manufactured by the CertiPrep Company (Metuchen, NJ. USA). The vials, Fig. 4.6, are made of hardened ferritic steel, but vials made of zirconia, alumina, agate and hard-metal tungsten carbide are also used to greatly limit contamination by grinding media (Fig. 4.7), which can be as high as several percent of Fe when milling in steel vials. The milling that yields **nanometric structure** takes place about **10 times faster in a SPEX ball mill than in a planetary ball mill**. The milling time needed to produce fine powders and nanostructure depends obviously on nature of material, but also on other milling parameters. The weight of the milling balls is one important parameter, the ratio of the powder charge to the weight of balls, B/P, is another. One can opt for balls having particular density, which can vary from 2.3 g/cm^3 to 4.0, 5.7, 7.8 and 16.4 g/cm^3 for alumina, zirconia, stainless steel, and tungsten carbide, respectively. The powder-to-balls weight ratio can vary too, from 1 to 100, and obviously, this is important to maintain the same ratio when one intends to compare results from different milling. As a first approximation one can expect the frequency of the impacts to be proportional to the number of balls used (usually two or three balls are sufficient) but also on the B/P ratio. The time needed for milling to the same fines of a powder usually decreases with the increase in the B/P ratio. Said this, we have to bring the reader's attention to often unexpected behavior of powder during high-energy milling. For example, the charge of pure aluminum powder milled for as short as 30 min in a SPEX mill changes to a multiplicity of small aluminum balls with 2-4 mm diameter, instead grinding the coarse Al powder into fine Al powder [sic!]. **Agglomeration and cold welding of metal particulates to the reactor wall and the milling balls** or to form "balls" made of the milled powder itself, are common phenomena that occur during milling pure ductile metals in vials filled with inert gas, like argon. On the other end, milling of graphite leads rapidly to amorphous carbons. Therefore, when formation of nanostructure is this intended task, one must design process carefully so neither "cold-welded balls" nor amorphous powders are produced.

Fig.4.6. Vibratory high-energy SPEX ball mill [10].

Fig. 4.7. Tungsten carbide and agate vials for Spex mill [10].

Other way to apply force to a milling ball, besides the gravitational and the centrifugal means discussed above, is to **drive ball motion by magnets**. On such a magnetic principle works the A.O.C. model **Uni-Ball Mill magnetic mill** developed in Australia (Wollongong, NSW, Australia). **The martensitic steel balls** in the reactor cylinder are attracted to the inside surface of the shell by strong Nd-Fe-B permanent magnets placed outside this shell (Fig. 4.8 and Fig. 4.9). The direction of the strong magnetic force is well defined by the lines of magnetic induction, which penetrate the shell made of **non-magnetic austenitic stainless steel** to end up in the martensitic (hence magnetic) balls. The **pull imparted by the external magnet on the magnetic balls inside is so strong that the centrifugal force acting on the balls becomes a secondary factor in milling.** High-energy milling can be achieved at low rotations (30-200 rpm). At low rotation the mill design is greatly simplified and two cylinders rotated on the same horizontal shaft can be filled sequentially with a process gas (like hydrogen). **What is more important, the**

motion of the balls inside the shell is well controlled by the external magnets to the point that the fraction of the impact and the shear modes of mechanical milling can be controlled. The **high-energy mechanical shear** force is imparted on the powder trapped between the shell and the ball when the magnet is in the 6 o'clock position. **In high-energy impact mode** each ball travels from the 6 o'clock position, at the bottom of the cylinder, to the 3 o'clock position, and then falls to the bottom of the reactor. The point where each ball is detached from the wall is well determined by the position of magnet; hence each ball imparts the same energy impact on the milled powder. Since each ball travels only quarter of the circumference of the shell it falls four times per one rotation. This results in 525 impacts per minute for a shell rotating at relatively low speed of 175 rpm.

At this frequency of impacts the energy transferred to the powder would be comparable with this achieved in a planetary ball mill. The milling cylinder suitable for reactive milling is shown in Fig. 4.9.

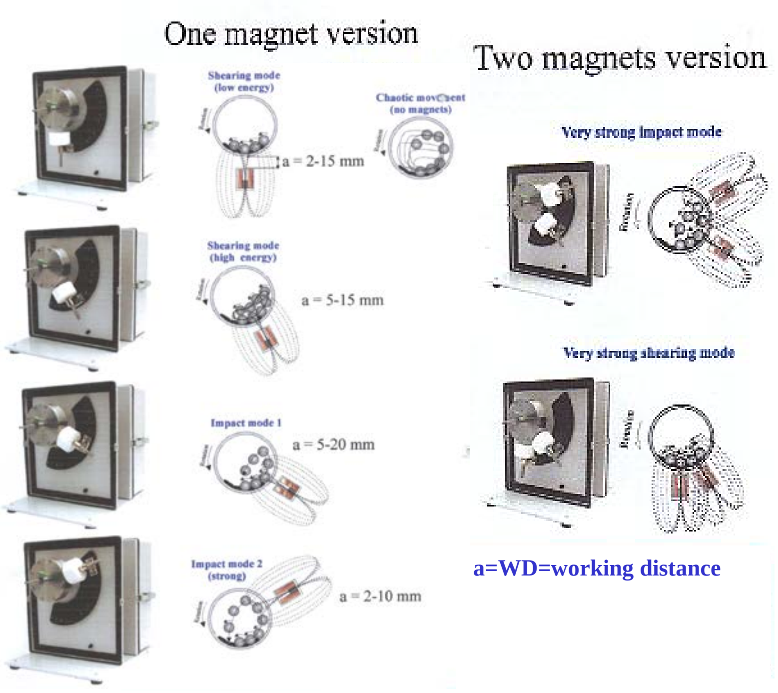

Fig. 4.8. Motion of balls in the magnetic Uni-Ball-Mill (courtesy A.O.C. Scientific Engineering, Australia) [10].

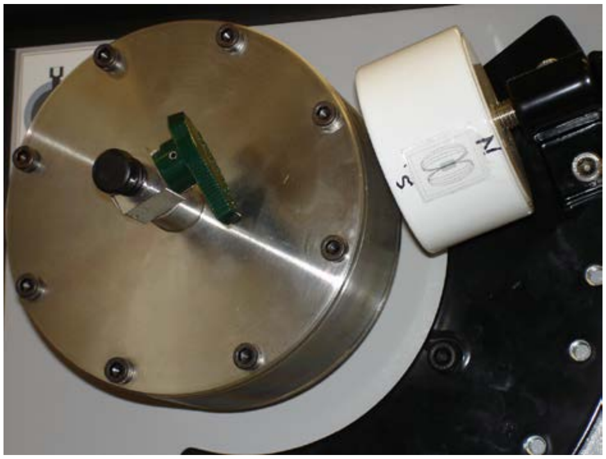

Fig. 4.9. Milling cylinder and magnet mounted for mechanical nano-processing in the mechanical low-energy impact mode (IMP) [**10**].

High-energy ball milling is a complex process, which requires optimization of many parameters to assure repeatability of nanostructure from batch to batch. To illustrate this complexity we can list the important parameters that must be decided when conducting the process in the magnetic A.O.C. model Uni-Ball Mill:

- Milling mode depends on the magnet position. Changing the magnet position one can change milling mode from low-energy shearing, through high-energy shearing, to low-energy impact and to strong impact. Two magnets options are also possible: (very strong shearing mode and very strong impact mode)
- Number of balls used for milling usually varies from two to four balls. Maximum 5 ball bearing balls with 1” diameter each can be used in one cylinder but the optimal number is four.
- Milling speed which can be controlled in a range 0-200 rpm depends on milling mode. More energetic modes usually requires fast rotation
- Milling time which is closely related to milling mode, working distance and type of process. Ball milling requires usually shorter time than mechanical alloying or reactive ball milling

- Milling atmosphere which is a neutral protective gas (helium or argon) during mechanical milling or hydrogen under pressure up to 0.9 MPa under reactive mechanical alloying processes
- Ball-to-powder weight ratio. This parameter depends on the mass of milled powder and number of balls and usually is in a range 10÷100. The maximum mass of powder in one cylinder is 25 g what allows for milling 50 g of powder at once in two cylinders. Ball-to-powder ratio affects efficiency of milling or synthesis process and can be controlled by changing mass of milled powder or number of balls. However, there is no visible influence of the ball-to-powder weight ratio on the particle size of the synthesized MgH_2 after reactive milling for 30 h
- Working distance (WD) is the distance between magnet (magnets) and cylinder. This parameter affects mainly the attractive force between the magnet and balls inside the cylinder. It is shown that increasing the WD reduces substantially the attractive force between the magnet and the 25mm steel ball. Neodymium (NdFeB) magnets used in the A.O.C. mills may vary in attraction force. High energy ball milling requires two magnets (Fig. 4.8). Ideally, magnets should have opposite polarity to double magnetic induction on balls operating in magnetic “air gap”.

Since there are so many variables in the magneto ball milling we carried out semi-empirical analysis to find just one parameter, viz. milling energy/mass powder that could be adequately used to characterize a specific mode of milling.

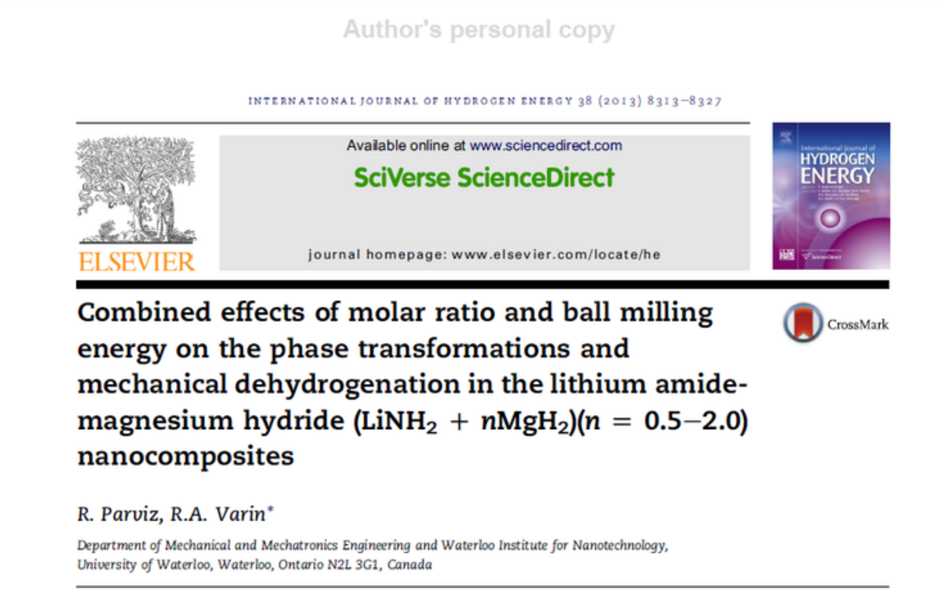

INTERNATIONAL JOURNAL OF HYDROGEN ENERGY 38 (2013) 8313–8327

Available online at www.sciencedirect.com

SciVerse ScienceDirect

journal homepage: www.elsevier.com/locate/he

Combined effects of molar ratio and ball milling energy on the phase transformations and mechanical dehydrogenation in the lithium amide-magnesium hydride ($LiNH_2 + nMgH_2$)($n = 0.5–2.0$) nanocomposites

R. Parviz, R.A. Varin*

Department of Mechanical and Mechatronics Engineering and Waterloo Institute for Nanotechnology, University of Waterloo, Waterloo, Ontario N2L 3G1, Canada

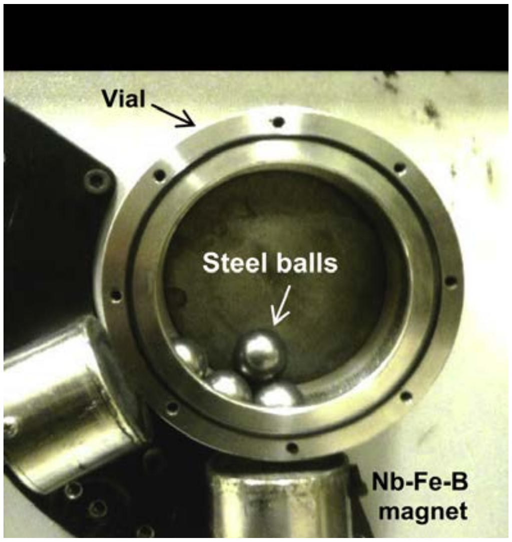

Fig. 1. The magneto ball mill, Uni-Ball-Mill 5 manufactured by A.O.C. Scientific Engineering Pty Ltd, Australia with the IMP68 magnets position.

$Li_2Mg(NH)_2$ and MgNH hydride phases. The powders were ground with KBr and pressed into pellets. All the samples were prepared and inserted into the machine through a purged box of high purity argon.

3. Semi-empirical study of ball milling energy

In this study we have been tried to estimate the total energy produced during the milling process. This energy can be separated into shearing and impact energies which are substantially increased by applying the strong magnets on ball mill machine. These two energies were calculated separately based on simple friction and kinetic energies concept. The following simplifying assumptions are used in calculations:

- Friction coefficient between balls and walls is constant.
- Each ball imparts the same impact energy on the milled powder.
- Both friction and kinetic energies resulting from the gravity force acting on balls are negligible.
- Temperature of vial, balls and hydrogen gas in the vial is the same during ball milling.

Table 1 lists the experimental parameters used in the calculations.

3.1. *Shear energy*

The sliding of steel balls on the layer of milled powder spread on the wall surface of milling vial under a big magnetic force causes to produce a significant amount of shear energy, Q_s, due to friction that is estimated from the following relationships:

$$Q_s = F_f \times S \text{ (J)} \tag{1}$$

$$F_f = F_N \times \mu \text{ (N)} \tag{2}$$

where F_f, S, F_N and μ are the friction force, sliding distance, normal force, and the friction coefficient between ball and wall, respectively. Fig. 2 illustrates the variations of magnetic force, as the normal force of friction with the distance, *d*, between the magnet and the ball. This plot was achieved by installing the magnet and a steel pin (with the same diameter as the ball) on the upper and lower grips of the tensile test machine and performing a pseudo-tensile test. The magnetic force vs. *d* fitted to the experimental data (Fig. 2) changes according to the following functional dependence:

$$F_m = -3.3623d + 84.547 \tag{3}$$

where F_m is in N and *d* is in mm. The energy Q_s per one rotation ($2\pi \times R_{vial}$) can be expressed by substituting in Eqs. (1) and (2) the sliding distance (rotation) $S = 2\pi \times R_{vial}$ and $F_m = F_N$ which results in the following equation:

$$Q_s = 2\pi \times R_{vial} \times F_m \times \mu \text{ (J/rotation)} \tag{4}$$

Table 2 shows the friction coefficients of some ceramics and oxides against a rotating steel counterpart. One can assume that the friction coefficient between steel ball and the ($LiNH_2 + MgH_2$) powder mixture is near the average of these values (~0.3). Substituting F_m from Eq. (3) and taking R_{vial} and the average $\mu = 0.3$ from Table 1 one obtains

$$Q_s = -0.477d + 12 \text{ (J/rotation)} \tag{5}$$

3.2. *Impact energy*

Direct observations of the ball movement show that in the high-energy impact modes each ball travels from the 6 o'clock

Table 1 – The values of different parameters used for calculations.

R_{vial}	75 mm
r_{ball}	12.5 mm
ω	200 rpm
m_{vial}	4030 g
m_{ball}	65 g
$m_{insulation}$	220 g
WD_6	10 mm
WD_8	2 mm
μ	0.3 [23–26]
$C_{vial(316)}$	0.5 (J/g°C) [27]
$C_{balls(420)}$	0.46 (J/g°C) [27]
C_{vH_2}	3.33T + 27.37 (J/mol°C) [28]
η_{H_2}	0.116 mol
m_{R40}	6.500 g
m_{R60}	4.300 g
m_{R132}	1.969 g

Note: C – heat capacity, η_{H_2} – mol of hydrogen, *m* – mass, m_R – mass of powder corresponding to a constant ball-to-powder weight ratio (R), $WD_{6 \text{ and } 8}$ – working distance for magnets at 6 and 8 o'clock positions (Fig. 3).

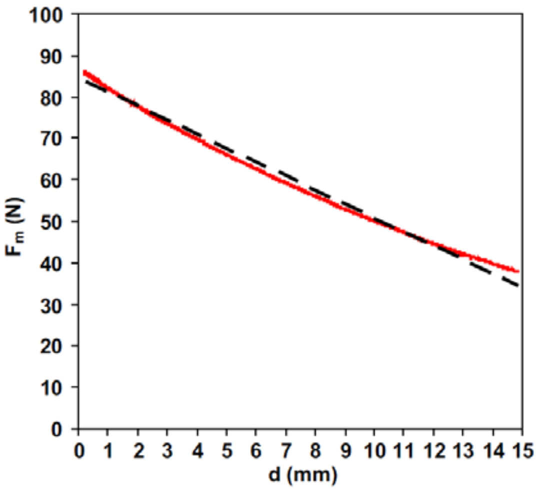

Fig. 2 – Variations of magnetic force with the distance *d* between the magnet and the ball. The continuous line is obtained from the experiment and the broken line is a fitted straight line (Eq. (3)).

Table 2 – Coefficients of friction (COF) for selected ceramics and oxide powder against the steel counterpart.

Ceramic	Counterpart	COF
Sialon (grade TCQ)	Steel	0.45 [23]
β-Sialon	Steel	0.22 [24]
95 mol.% ZrO_2, 5 mol.% Y_2O_3	Hardened steel	0.30 [25]
92 mol.% ZrO_2, 4 mol.% Y_2O_3, 4 mol.% CeO_2	Hardened steel	0.40 [25]
Y-TZP ceramics	Steel	0.35 [26]

to the 9 o'clock position, and then is aggressively attracted by the 6 o'clock magnet and impacts the wall. Eq. (3) shows that at the critical distance $d_{crit} = 25$ mm the magnetic force $F_m = 0$. We assume that a steel ball starts falling under gravity forces from the position at the center of the vial ($R_{vial} = 75$ mm) until it reaches a critical distance $d_{crit} = 25$ mm. At the exact critical distance the kinetic energy of a moving ball is very small and negligible. From this point, a ball is strongly affected by the magnetic force which increases by decreasing the distance to the impact point at the bottom of the vial at the working distance WD from the magnet (Fig. 3). In order to simplify the calculations, it is assumed that the ball is falling under a constant force, which is the average magnetic force between these two points expressed as follows:

$$F_{avg} = \frac{\left(F_m^{d_{crit}} + F_m^{WD}\right)}{2} \tag{6}$$

The kinetic energy per impact, Q_i, can be approximated by a general equation for the kinetic energy in the following form:

$$Q_i = ½m_{ball} \times v^2 \text{ (J/impact)} \tag{7}$$

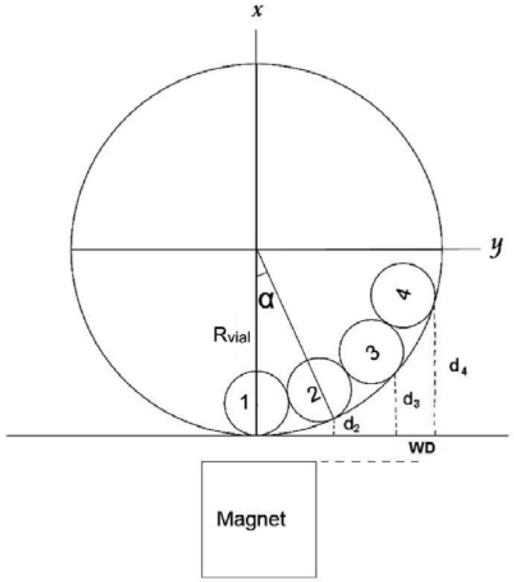

Fig. 3 – A schematic of ball trajectories in the vial with a 6 o'clock magnet position.

Now substituting the acceleration, a

$$a = F_{avg}/m_{ball} \tag{8}$$

and the ball velocity, v

$$v^2 = 2a \times d \tag{9}$$

the final equation for Q_i is obtained in the following form:

$$Q_i = -0.04d + 1.05 \text{ (J/impact)} \tag{10}$$

3.3. *Ball positions*

Since the total number of balls which can be placed along the total vial circumference is 13, therefore the angle between each two balls is as shown in Fig. 3:

$$\alpha = 360°/13 = 27.7°$$

The maximum number of balls which can stay in contact in equilibrium with the rotating vial during the ball milling is 4 as shown in Fig. 3. The distance between these balls and the magnet surface can be calculated by means of angular equation of a circle as follows:

$$y_n = R_{vial} \cos \alpha_n \tag{11}$$

$$x_n = R_{vial} \sin \alpha_n \tag{12}$$

$$\alpha_n = 27.7(n - 1) \ (n = 1,2,3,4) \tag{13}$$

$$d_n = R_{vial} - y_n + WD \tag{14}$$

where n, α_n and d_n are the ball number in Fig. 3, the angle between position 1 and the instant position of ball "n" and the distance from the vial-ball contact point to the magnet surface, respectively. Substituting the values of R_{vial} and WD from Table 1 in Eq. (14) reveals that the distances of balls 2, 3 and 4 ($d_2 = 28.6$ mm, $d_3 = 52$ mm and $d_4 = 86$ mm) are bigger than the critical distance ($d_{crit} = 25$ mm). This means that these three balls are not affected by the magnetic force of the magnet at the 6 o'clock position and do not contribute to any significant friction on the wall.

3.4. *Total energy of ball milling*

The number of balls acting in shear (N_s) and the number of impacts per rotation which will be now called "an impact factor M" are changed by adding the second magnet to the ball mill (Fig. 1). These two parameters, N_s and M, were measured for 5 different milling modes, by means of a transparent epoxy vial lid and a HD video recording camera. Each test was repeated 3 times and the average values used for calculations. The impact factor, M, for each milling mode is given by

$$M = N_{imp} \ (t_r/t_m) \text{ (impacts/rotation)} \tag{15}$$

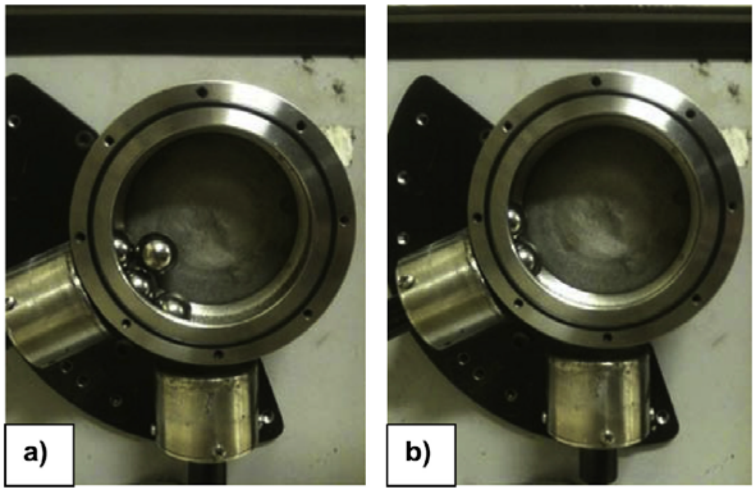

Fig. 4 – Ball positions in the vial for (a) IMP68-4B and (b) IMP68-2B milling modes.

where N_{imp} (impacts/rotation) is the number of impacts within t_m milling time and t_r is the time per one rotation of vial which equals 0.3 s for 200 rpm.

The visual examination reveals that in the IMP68-4B (Fig. 4a) and IMP68-2B (Fig. 4b) milling modes, impact and shearing are occurring at the magnet located at the 8 o'clock angular position and the second magnet (at 6 o'clock) is not involved directly in either shearing or impact. Therefore, the total milling energy which is calculated based on the experimental observations and theoretical analysis, is expressed by Eq. (16)

$$Q_T = MQ_i + N_sQ_s \text{ (J/rotation)} \quad (16)$$

In order to convert MQi and NsQs to (J/h) both must be multiplied by (200x60)(rotation/h). The calculated values of total milling energy Q_T in (kJ/h) for several different milling modes are shown in Table 3.

3.5. *Mechanical energy conversion to heat*

A considerable fraction of the total milling energy (Q_T) converts to heat and locally increases the temperature during ball milling. By measuring the inside temperature of vial during ball milling we can calculate the amount of energy converted to heat, Q, according to the following general relationship:

$$Q = \Delta T \times C_{material} \quad (17)$$

where ΔT is the temperature difference and $C_{material}$ is the heat capacity of a material (Table 1). Therefore, the total amount of heat produced during ball milling can be expressed in the following manner:

$$Q_{heat} = Q_{vial} + Q_{balls} + Q_{H_2} \quad (18)$$

Table 3 – Calculated values of impact, shearing and total milling energy for several different milling modes.

Mode	N_{imp}	t_m (s)	M (Impacts/rotation) average	N_s		MQ_i (kJ/h)	N_sQ_s (kJ/h)	Q_T (kJ/h)
				Magnet at 6 o'clock (WD = 10 mm)	Magnet at 8 o'clock (WD = 2 mm)			
LES6-2B	84	18	1.50	1	0	11.7	86.76	98.46
	80	16						
	76	14						
LES6-3B	100	17	1.67	1	0	13	86.76	99.76
	106	20						
	90	15						
LES6-4B	128	20	1.92	1	0	14.97	86.76	102.73
	200	30						
	108	18						
IMP68-2B	90	15	1.80	0	1	20.9	132.50	153.40
	120	20						
	120	20						
IMP68-4B	111	9	3.45	0	2	40.16	265.00	305.16
	162	15						
	138	12						

Table 4 – Experimental values of produced heat inside the vial during ball milling and the fraction of total energy Q_T converted to heat, Q_{heat}.

Milling time (min)	T_o (°C)	T (°C)	Q_T (kJ)	Q_{heat} (kJ)	Q_{heat} (%)
1	23.7	24.6	4	2.10	52.48
2	23.7	27.1	14	7.93	56.65
3	23.7	29	24	12.37	51.52
4	23.7	36.1	49	28.95	59.08
5	23.7	38.4	73	34.32	47.02
10	23.7	45	98	49.76	50.78

where Q_{vial}, Q_{balls} and Q_{H_2} is the amount of heat which increases temperature of vial, balls and hydrogen gas inside the vial. Q_{H_2} can be calculated from the well-known equation [28]:

$$Q_{H_2} = \int_{T_0}^{T} \eta_{H_2} C_{vH_2} dT \quad (\Delta V = 0) \tag{19}$$

where η_{H_2} is the number of moles H_2 and C_{vH_2} is the thermal capacity of H_2 at a constant volume, which from Table 1 equals 0.116 mol and (3.33T + 27.37) J/mol °C, respectively. After substituting these values into Eq. (19), solving it and substituting the solution and other pertinent constant values from Table 1 into Eq. (18), one obtains:

$$Q_{heat} = 0.193(T^2 - T_o^2) + 2206.48(T - T_o) \text{ (J)} \tag{20}$$

where Q_{heat} (J) is the necessary energy to increase the temperature from T_o to T (ΔT). As mentioned before, this energy is a fraction of the total milling energy Q_T. In order to estimate this fraction, the temperature changes inside the vial loaded with the ($LiNH_2$ + $0.7MgH_2$) powder ball milled under IMP68-4B-R40 milling mode were measured. For this propose the milling vial was fully insulated using a glass wool to keep the produced heat inside the vial. In each measurement, the temperature of three different points of the vial (bottom, middle and top) was measured by entering a NiCr–NiAl (chromel/alumel) thermocouple into the vial from a hole on the vial lid. Table 4 shows the values of total mechanical energy and measured heat energy at different milling time.

According to these results, on average, approximately 53% of total mechanical energy Q_T converts to heat and the rest, that means 47% designated here as $Q_P = 0.47Q_T$, is injected into the powder and consumed for powder compressing, particle refining (breaking) and microstructural evolution. Since the mass of powder can be changed for each milling mode, it is convenient to express the injected energy, Q_P, as a normalized energy per unit mass of powder which is conveniently expressed by the ball-to-powder mass ratio, R, according to the following equation:

$$Q_{TR} = Q_P/m_R \text{ (kJ/g h)} \tag{21}$$

where m_R is the mass of powder corresponding to a constant ball-to-powder mass ratio, R. Table 5 shows the calculated values of the normalized energy, Q_P and corresponding Q_{TR} for various milling modes with a constant ball-to-powder mass ratio R.

Table 5 – The amount of energy injected into the milling powder which varies by variation of ball-to-powder weight ratio (R).

Milling mode	Q_P (kJ/h)	Q_{TR40} (kJ/gh)	Q_{TR60} (kJ/gh)	Q_{TR132} (kJ/gh)
LES6-2B	46.3	7.1	10.8	23.5
LES6-3B	46.9	7.2	11.0	23.8
LES6-4B	48.3	7.4	11.2	24.5
IMP68-2B	72.1	11.1	16.8	36.6
IMP68-4B	143.4	22.1	33.3	72.8

Table 6 – The estimated grain size and lattice strain of $LiNH_2$ in the ($LiNH_2$ + $nMgH_2$) composite as a function of total milling energy (kJ/g).

Hydride system/ball milling mode and time	Q_{TR} (kJ/g)	Grain size $LiNH_2$ (nm)	Strain (%)
As-received $LiNH_2$	0	200	0.06
$LiNH_2$-IMP68-R40-4B-25h	552	32	0.20
$0.5MgH_2$-IMP68-R40-4B-25h	552	21	0.42
0.7 MgH_2-LES6-R60-3B-21h	231	53	0.20
0.7 MgH_2-LES6-R132-3B-21h	500	18	0.34
0.9 MgH_2-LES6-R60-4B-24h	269	14	0.12
0.9 MgH_2-IMP68-R60-4B-12h	400	20	0.40
1.0 MgH_2-LES6-R40-3B-25h	190	30	0.30
2.0 MgH_2-LES6-R40-3B-21h	151	35	0.49

Note: IMP-impact mode; LES-low energy shearing; B-number of steel balls, e.g. 4B = 4 steel balls.

4. Results and discussion

4.1. *Structural refinement*

In general, it is very well documented that ball milling of metal/intermetallic alloys introduces a substantial refinement

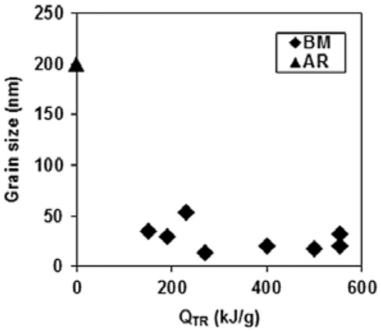

Fig. 5 – The estimated grain size of $LiNH_2$ in the ($LiNH_2$ + $nMgH_2$) composite as a function of the injected milling energy Q_{TR} (kJ/g) for n = 0.5, 0.7, 0.9, 1.0 and 2.0. AR-as received, BM-ball milled.

4.4. Stresses, deformations and equilibrium mechanical processing

One can notice that the atoms in the stressed body during ball milling change their relative positions (with respect to one another) mostly under **the shear elastic stress** than under tensile or the compressive elastic stresses. In simple terms **elastic deformation (strain)** is defined as the **reversible deformation (strain) that occurs when a load is applied**. Most materials **deform in a linear elastic fashion** i.e., the amount of **reversible deformation is a linear function of the applied stress up to a certain stress level**, i.e., the strain (tensile, compressive or shear divided by original length) **-ε** is proportional to the applied stress, **σ** (force divided by cross-section) according to the Hooke's Law

$$\boldsymbol{\sigma} = E\boldsymbol{\varepsilon} \qquad (4.11)$$

where E - Young's/elastic modulus is materials constant which quantifies elastic behaviour. Most **non-metallic materials**, like salts, oxides and ceramics deform also in such a linear fashion, although in a very small range: if the applied force is further increased the compound fractures in a catastrophic manner.

If, further to the above, one assumes proportional relationship to reflect on lowering energy by the action of mechanical force then a term proportional to the elastic shear stress, $\alpha\times\boldsymbol{\sigma}$**,** must be subtracted from the activation energy E_A [**111**]:

$$k = k_0 \exp[-\frac{(E_A - \alpha\sigma)}{RT}] \qquad (4.12)$$

where **α is a proportionality constant,** and **k is the rate at which covalent bond in non-metallic material** is ruptured. Now, one can substitute the stress for the strain, and the relation between applied elastic stress and the rate k can be proposed:

$$k = k_0 \exp[-\frac{(E_A - E\alpha\varepsilon)}{RT}] \qquad (4.13)$$

Therefore, **the rate, at which chemical bonds break, increases with elastic shear stressing of the** material. **The rupture of chemical bonds, hence fracture of material, leads to its fragmentation into particles.** This reduces the average particle size in powder as fractured particles multiply into even smaller particles. The Eq. (4.13) points to the importance of **elastic shear strains in mechanical activation of chemical bonds for *particle size refinement* and production of nanoparticles.**

Most metals initially deform elastically and then begin to **deform plastically (non-reversible strain)**. Plastic deformation is **due to formation and movement (slip) of dislocations**. Plastic deformation **allows energy of stresses to be dissipated rather than building up to the point where the material breaks**. **Such dissipated energy is used for** ***grain size refinement*** in **each of the deformed material particles**. **This results in decrease of the average grain size**. Therefore, **the energy of balls, which was transferred to the material, is utilized for both: particle and grain size refinement**. The "beauty" of nanostructuring in ball mills comes in the observation made that **both the particle size and the grain size are equally rapidly decreased with even short processing in a high-energy ball mill**, as shown in Fig. 4.10.

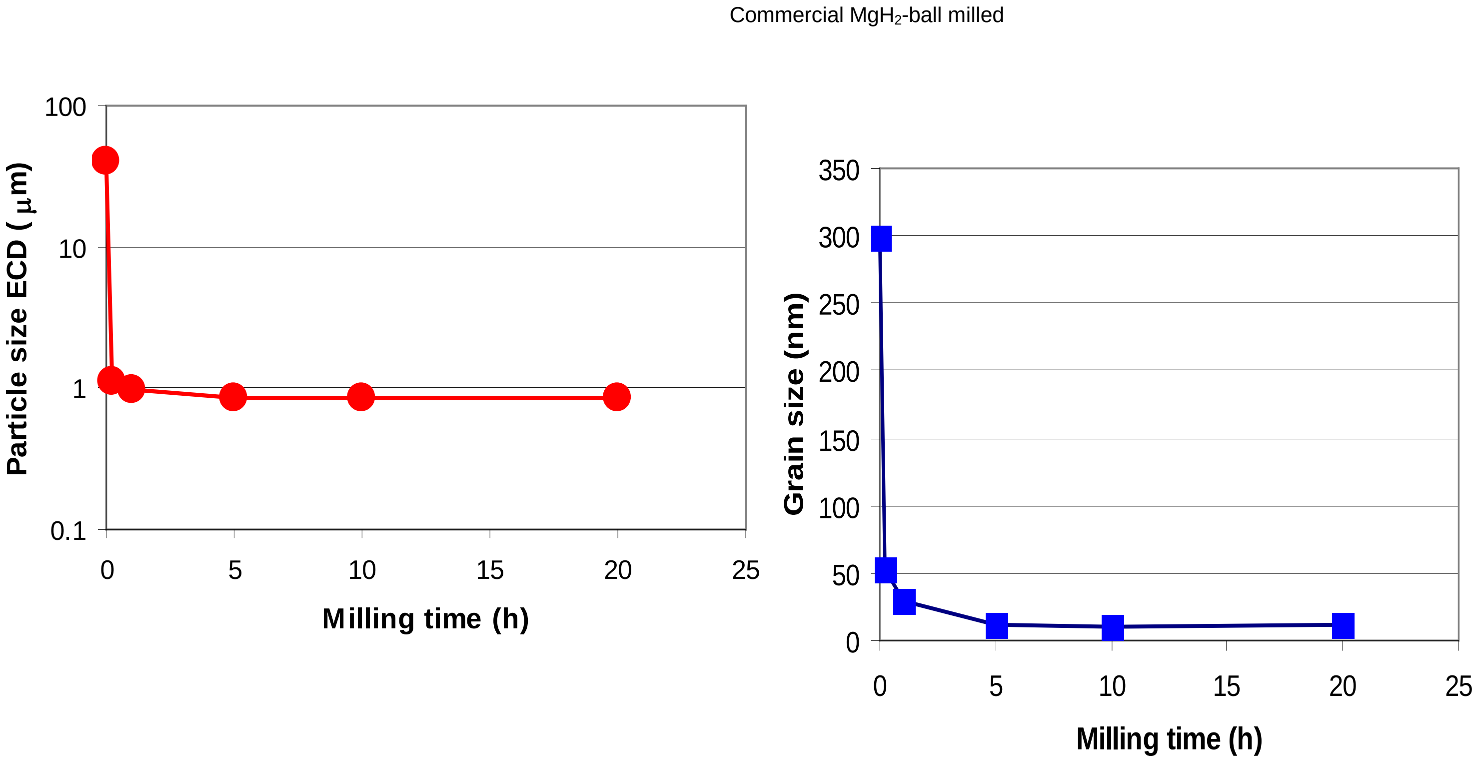

Fig. 4.10. Simultaneous reduction of the particle size and the grain size in fully hydrogenated magnesium powder, MgH_2 [10, 112].

As can be seen, it is very difficult to reduce a particle size of solid hydrides below approximately **1 μm** size. This is a general observation relevant for all types of solid hydrides. In contrast, the grain size of grains formed in powder particles can be **reduced to truly nanometric sizes**.

While no Government of Canada wide definitions for nanomaterials and nanotechnology currently exist, for the purposes of this document, the Health Canada working definition of nanomaterials is used [**113**]. This working definition, indicates that a manufactured substance or product and any component material, ingredient, device, or structure is considered to be a nanomaterial if ***"(a) it is at or within the nanoscale (1-100 nm) in at least one external dimension or has internal or surface structure at the nanoscale; or (b) it is smaller or larger than the nanoscale in all dimensions and exhibits one or more nanoscale/properties/phenomena***". Nanotechnology is described as the control of matter at the nanoscale or utilizing nanoscale phenomena to enable novel applications.

However, an important question is now how does plastic deformation through movement and reorganization of dislocations lead to the development of nanometric grains? Fecht [**114**] through direct observations of the individual grains within the deformed powder particles by transmission electron microscopy (TEM) and X-ray diffraction found that the elemental processes leading to me grain size refinement include three stages:

(i) Initially, the deformation is localized in shear bands consisting of an array of dislocations with high density.

(ii) At a certain strain level, these dislocations annihilate and recombine to small angle grain boundaries separating the individual grains. The subgrains formed via this route are already in the nanometer size range with diameters often between 20 and 30 nm. During further attrition the sample volume exhibiting small grains extends throughout the entire specimen.

(iii) The orientations of the single-crystalline grains with respect to their neighboring grains become completely random. Probably, superplastic deformation processes such as grain boundary sliding cause this self-organization into a random nanocrystalline state.

4.5. Hydrogen entry into the ball milled microstructure

In general, grain boundaries are **truly disordered**, if not plainly amorphous. By forming nanostructure in the individual powder particles the fraction of atoms which counts into grain boundaries should increase with milling time. Nanostructured materials are such where the

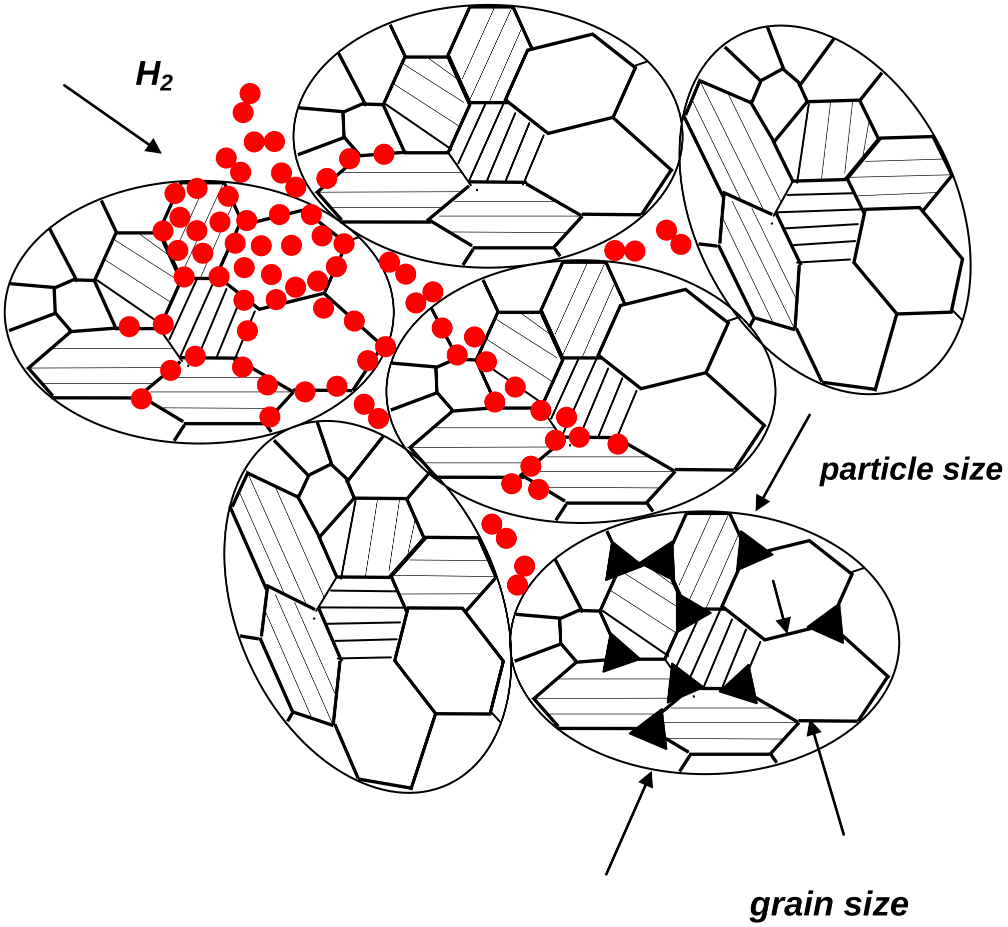

Fig. 4.11. Particle size and grain size in a nanostructured powder. Red points depict hydrogen molecules H_2 (●●) in the pores between particles (triple junctions), and hydrogen atoms (●) diffusing through a grain boundary network and gradually entering the grain interior; black triangles point to triple points that are preferential sites for hydrogen atoms accumulation [10].

density of grain boundaries is maximized. It must be noted that nanopowders are not necessarily consisting of nano-metric particles (nanoparticles). **The powder particles may be actually of micrometric sizes, yet the particle interior may be divided into many nanograins.** Such nanograins are the smallest diffracting domains in X-ray diffractometry (XRD), and being incoherent to X-ray diffraction they cause peak broadening in X-ray diffractometry.

Hydrogen molecule, H_2, enters the ball milled powder at the paths between the individual powder particles and locate themselves in the triple junction pores as shown schematically in Fig. 4.11. Furthermore, on contact with catalytic metal surfaces of individual grains, the individual hydrogen atoms (H) enters the material as dissociated hydrogen atoms through grain boundaries of nanograins which were formed in the individual nanograins during ball milling as shown schematically in Fig. 4.12.

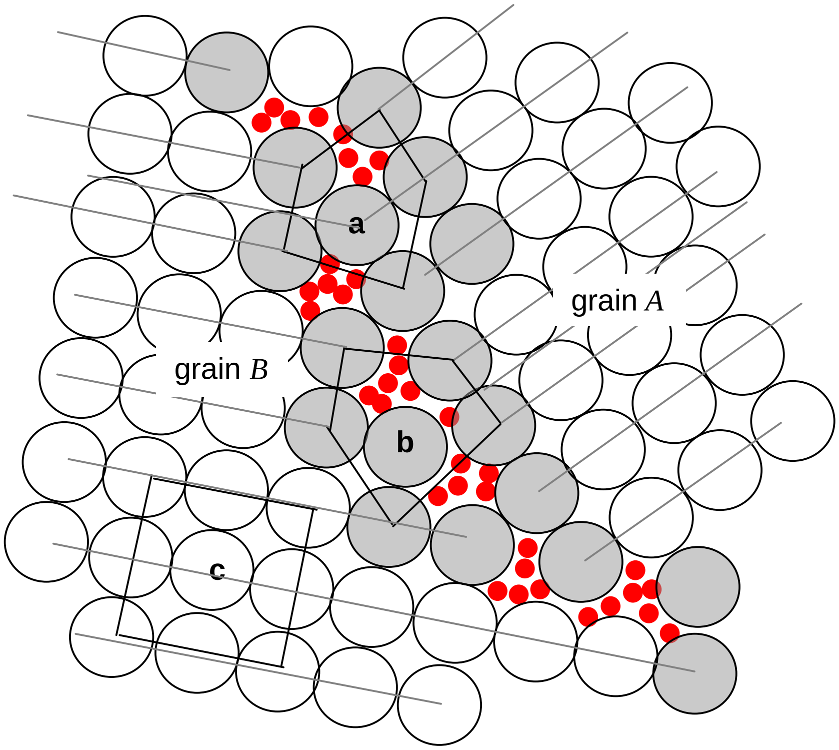

Fig. 4.12. Enlarged view of hydrogen atoms (red circles) in the grain boundary between two grains A and B (grey circles). Note, varying short-range order around atoms **a** and **b** which belong to the grain boundary, and fixed order around atoms type **c** which belong to the grain core [**10**].

Yet, the picture in which the particle size and the grain refinement are sole reasons for mechanochemical activation of powders for reactions with hydrogen is not complete. **Nanostructuring by ball milling introduces a variety of defects, vacancies, dislocations,**

stacking faults besides the described above grains and grain boundaries. These defects raise the free energy of the system making it accessible to formation of thermodynamically metastable phases.

4.6. Experimental methods for microstructural characterization of ball milled hydrides

Two important morphological parameters characterizing ball milled powders are the **particle** and **grain size** of constituent phases within the powders. **The size measurement of the powder particles** can carried out by attaching loose powder to sticky carbon tape and taking pictures under secondary electron (SE) mode in the SEM. The images are then analyzed by an image analysis software. The size of the powders is calculated as the particle equivalent circle diameter, ECD $=(4A/\pi)^{1/2}$, where A represents the projected particle area. Usually from ~300 to 700 particles are analyzed for each batch.

The crystalline structure of hydride powders is characterized by powder diffraction. **The nanograin (crystallite) size of phases** residing in the milled powders is calculated from the broadening of their respective x-ray diffraction (XRD) peaks. Since the Bragg peak broadening in an XRD pattern is due to a combination of grain refinement (nanograin/crystallite) and lattice strains, it is customary to use computing techniques by means of which one can separate these two contributions. The separation of crystallite size and strain is obtained from a Cauchy/Gaussian approximation by a linear regression plot according to the following equation [115]:

$$\frac{\delta^2(2\theta)}{\tan^2\theta} = \frac{K\lambda}{L}\left(\frac{\delta(2\theta)}{\tan\theta\ \sin\theta}\right) + 16e^2 \qquad (4.14)$$

where the term $K\lambda/L$ is the slope, the parameter L is the mean dimension of the nanograin (crystallite) composing the powder particle, K is a constant (≈1) and e is the so-called ‘maximum’ microstrain (calculated from the intercept), λ is the wavelength and θ is the position of the analyzed peak maximum. The term $\delta(2\theta) = B[1-(b^2/B^2)]$ (rad) is the instrumental broadening-corrected ‘pure’ XRD peak profile breadth [115], where B and b are the breadths in radians of the same Bragg peak from the XRD scans of the experimental and reference powder, respectively.

The B value is approximated as the full width at half maximum, FWHM, and calculated by the diffractometer software. The b value is approximated as FWHM from the X-ray diffraction pattern of a compound LaB_6, the National Institute of Standards and Technology (NIST) standard reference material (SRM) 660 for subtracting the instrumental broadening from the experimental FWHM and finding $\delta(2\theta)$as given above. It must be noted that when FWHMs of the instrumental line profiles are obtained in this manner, the Bragg peaks for the LaB_6 SRM are occasionally at different 2θ angles than those of the analyzed hydride in the milled powders. The interpolated FWHM values between angles for the SRM peaks are found using a calibration curve. A typical regression plot according to Eq.(4.14) is shown in Fig. 4.13. It must be also noted that modern X-ray diffractometers are usually equipped with software which calculates grain size and lattice strain.

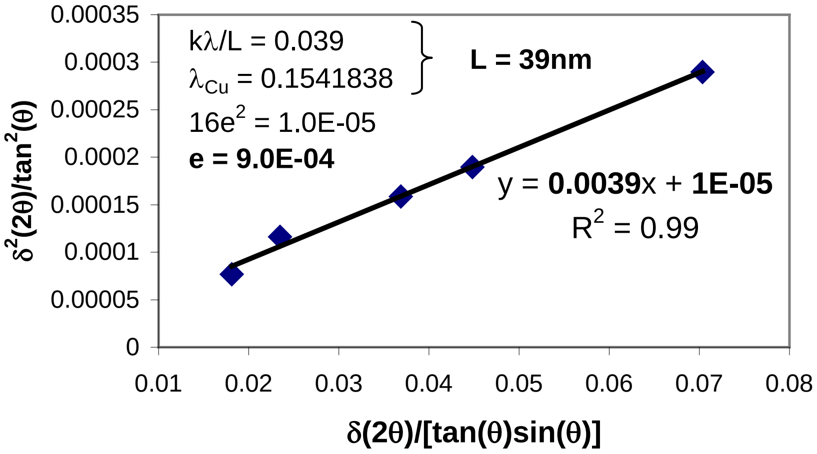

Fig. 4.13. Cauchy/Gaussian plot (Eq.(1.48)) for the grain size of dehydrogenation of MgH_2 (ABCR) milled for 20 h and catalyzed by 5 wt.% Ni [10].

A good analysis of crystallite (nanograin) size estimate from the analysis of X-ray diffraction patterns is provided in the following paper;